NTNU – Trondheim
Norwegian University of
Science and Technology

Laser Induced Incandescence with Long Pulse Duration

Stine Myhre Hverven

Master of Science in Physics and Mathematics
Submission date: June 2013
Supervisor: Jon Andreas Støvneng, IFY
Co-supervisor: Mario Ditaranto, SINTEF Energi AS

Norwegian University of Science and Technology
Department of Physics

Acknowledgements

I would mainly like to thank my advisor Dr. Mario Ditaranto at SINTEF Energy AS for giving me the opportunity of working on this project. Thank you for letting me continue with the project in my Master's thesis. I want to express my sincere gratitude for your great guidance throughout the project.

I would also like to thank Dr. Alexis Sevault for his help during the early stages of the project, especially the specialization project. I am extremely grateful for your help and guidance when teaching me about the laser lab.

Dedication
- To My Constant Optimism

I would like to dedicate this master thesis to myself, especially my constant optimism. Without my own stupendous effort, this thesis and Master's degree would not have come about. There are some important people who have supported me along the way, but these people already know who they are and therefore don't need any further praise or honor bestowed upon them.

It must be mentioned that this project has taught me the many aspects of Murphy's Law. My optimistic motto when working in the lab has for instance been "if anything simply cannot go wrong, it will anyway. This is experimental science" or "though you might not think it possible, there is always something else which can go wrong today". These guiding and uplifting thoughts have helped me through many dark days. It is thus mostly due to my own great optimism that I now can hand in this thesis.

After all, a wise man once said, "a smooth sea never made a skilled sailor."

$Hvala.$

Summary

Laser Induced Incandescence (LII) is a technique used to observe soot concentration and particle size in a flame. The LII signal is captured by an intensified CCD camera. Laser light impacts and heats soot particles within the flame, and the resulting intensity signal is detected. The LII signal is the radiation from the soot particles, and its temporal profile depends on many physical processes. The collected intensity images are further analyzed to generate the temporal profile of the LII signal.

Detailed LII measurements were performed in order to study an unknown phenomenon which first appeared in a previous experiment at SINTEF. Two peaks were found to appear in the temporal LII signal when laser pulses of pulse duration longer than 100 ns were used.

The main part of this thesis was dedicated to preparing the experimental setup, running LII measurements and analyzing temporal LII profiles. The LII measurements were performed on a small laminar ethylene flame with varying laser pulse duration and pulse fluence. An Nd:YAG laser with wavelength 532 nm was used, and later the first harmonic 1064 nm laser light. The temporal laser profiles had pulse duration in the range 50 to 450 ns, all rectangular in shape. The laser energy incident on the ethylene flame was varied using a combination of a half-wave plate and a beamsplitter.

Several hypotheses were presented after the previous experiments at SINTEF, and these have been studied more carefully. As an example, areas within the flame where the soot's morphological characteristics are different were analyzed and found not to have an effect. PAH-fluorescence and contribution from C_2-radicals have also been ruled out as possible causes of the phenomenon. The cause of the two peaks appearing in the temporal LII signal is still unknown, but the results show some interesting aspects of the phenomenon.

For the two peaks to appear, a certain fluence threshold must be reached. Studies of the time-integrated LII signal vs. laser pulse fluence revealed a new profile not previously seen. Such graphs have previously shown a saturation curve, saturating around 0.4-0.5 J/cm^2 for the 1064 nm laser light. The results presented in this thesis show that this signal begins to increase again for higher fluence values. It is when the signal begins to increase that the two peaks become visible in the temporal LII profiles.

The phenomenon's irradiance dependence is also analyzed, but more data is required to give a decisive conclusion. It might be that the two peaks are present in studies using 10 ns pulse duration, but that due to the short time frame only a single peak is seen.

Possible causes of the two peak phenomenon are presented and discussed. Advise on further research, both experimental and computational, is also presented. The two peaks might be caused by morphological changes in the soot, or by creation of new particles due to vaporization. It might also be caused by unknown processes the soot undergoes when impacted by the laser beam.

Sammendrag

Laserindusert glødning (LII) er en teknikk brukt til å karakterisere konsentrasjon og størrelse av sotpartikler i en flamme. LII-signalet fanges opp av et ICCD-kamera. Kameraet brukes til å detektere signalet som oppstår når en laserstråle treffer og varmer opp sotpartikler i en flamme. LII-signalet er varmestrålingen fra de glødende sotpartiklene. Tidsavhengighet til signalet er summen av flere fysiske prosesser. Intensitetsbildene tatt av kameraet blir videre behandlet og analysert for å generere tidsresponsen til LII-signalet.

Detaljerte eksperimentelle LII-målinger ble utført for å studere et hittil ukjent fenomen som dukket opp i et tidligere forsøk ved SINTEF. To toppunkter ble funnet i det tidsavhengige LII-signalet da en laser med pulsvarighet lenger enn 100 ns ble brukt. Det har tidligere kun blitt observert ett toppunkt i LII-signalet, kalt ”prompt LII”.

I denne masteroppgaven gikk mesteparten av tiden til å sette opp det eksperimentelle oppsettet, kjøre LII-målinger og videre analysere resultatene. LII-målingene ble utført på en liten laminær etenflamme. Laserstrålen hadde varierende pulsvarighet og energi. Laseren som ble brukt var en Nd:YAG-laser med 532 nm og 1064 nm som mulige bølgelengder. Laserpulsene hadde pulsvarighet i området 50-450 ns og var rektangulære i tid. Laserens energi ble variert ved hjelp av en kombinasjon av en halvbølgeplate og en strålesplitter.

Flere hypoteser ble presentert som følge av de tidligere forsøkene ved SINTEF og disse har blitt sett nærmere på. For eksempel ble ble det gjort undersøkelser av ulike områder i flammen hvor sotets morfologiske karakteristikk er forskjellig. Fluorisering fra PAH-molekyler og bidrag fra C_2-radikaler har også blitt utelukket som mulige årsaker til fenomenet. Årsaken til de to toppunktene i LII signalet er fortsatt ukjent, men resultatene viser noen interessante aspekter av fenomenet.

For at de to toppunktene skal være synlige, må laserpulsen som blir brukt ha en viss energi. Grafer over det tidsintegrerte LII-signalet mot energitetthet avdekker en kurveform som hittil ikke har blitt observert. Slike grafer har tidligere vist en metningskurve som stabiliserer seg rundt 0,4-0,5 J/cm^2 for 1064 nm laserlys. Resultatene som presenteres i denne rapporten viser derimot en kurve som begynner å øke igjen ved høyere energitettheter. Det er når signalet har begynt å øke igjen at de to toppunktene blir synlige i det tidsavhengige LII-signalet.

Fenomenets irradiansavhengighet er også analysert, men mer data er nødvendig for å kunne konkludere noe med sikkerhet. Det kan være at de to toppunktene faktisk er tilstede i LII-signaler tatt ved bruk av en 10 ns laserpuls, men at dette ikke er synlig på grunn av den korte tiden, og det har derfor kun blitt observert ett toppunkt.

Mulige årsaker til fenomenet med de to toppunktene blir presentert og diskutert. De to toppunktene kan være forårsaket av morfologiske forandringer i sotet, eller ved dannelsen av nye partikler som følge av fordamping. De kan også være forårsaket av ukjente prosesser sotet går igjennom når det blir truffet av laserstrålen. Anbefalt videre forskning, både eksperimentell og numerisk, er også presentert.

Preface

This Master's thesis is the result of work done at SINTEF Energi AS during spring 2013. The thesis is a continuation of my specialization project fall 2012, and it is a collaboration between the Norwegian University of Science and Technology (NTNU) and SINTEF Energi AS.

Declaration

I hereby declare that this work has been performed independently and in accordance with the rules and regulations at the Norwegian University of Science and Technology (NTNU).

Trondheim, June 2013

Stine Myhre Hverven

Table of Contents

List of Figures

Abbreviations

LII	=	Laser Induced Incandescence
PAH	=	Polycyclic Aromatic Hydrocarbons
LIF	=	Laser Induced Fluorescence
ICCD camera	=	Intensified Charge-Coupled Device camera
NOC	=	Organic Carbon Nanoparticles
DOF	=	Depth Of Field
ROI	=	Region Of Interest
CW	=	Continuous Wave
Nd:YAG	=	Neodymium-doped YAG
YAG	=	Yttrium Aluminum Garnet
IR	=	Infrared
UV	=	Ultraviolet
FWHM	=	Full Width at Half Maximum
i.e.	=	From Latin ”id est”, means ”that is”
vs.	=	versus
NTNU	=	Norwegian University of Science and Technology
TEM wave/mode	=	Transverse ElectroMagnetic wave/mode
TEM image	=	Transmission Electron Microscopy image

1 Introduction

Soot formation in combustion is a very complex problem with many physical and chemical aspects involved. Many chemical reactions take place until soot is finally created and much research goes into the study of the various combustion generated particles. If under ideal conditions, the combustion process of a hydrocarbon, such as ethylene gas C_2H_4(g), would lead to the formation of only carbon dioxide and water. However, real life combustion systems have non ideal conditions. Combustion-generated pollutants are notably soot, but also by-products such as organic carbon nanoparticles (NOC) and polycyclic aromatic hydrocarbons (PAH). The reason for studying soot formation is the possible future reduction of such unwanted combustion by-products. For example, soot from diesel exhaust pollution accounts for over one quarter of the total hazardous pollution in the air [1].

Laser Induced Incandescence (LII) was first observed by Eckbreth in 1977 when recording Raman measurements in a propane diffusion flame (Eckbreth, 1977). Today, theoretical models for the interaction between laser light and soot particles have been developed and are frequently used. The LII technique has been used for measuring soot volume fraction and particle size in diesel engines and exhaust gases. Different flame types such as premixed, diffusion, laminar and turbulent flames have been rigorously studied. Both point measurements and two-dimensional imaging are widely used.

It is common to use a high energy laser pulse of about 10 ns pulse duration. The prompt LII signal is the signal from the soot at maximum temperature shortly after its first impact with the laser beam pulse. This signal is proportional to soot size and density. Since the initial peak of the LII signal is what is commonly studied, a short and energetic pulse is usually preferred. Many studies of the LII signal have been done with varying laser energy fluence. A threshold fluence has been observed by many researchers to be 0.2 J/cm^2 for 532 nm laser light. This threshold value corresponds to the vaporization threshold for the soot particle. When studying the effect of laser fluence on the LII signal, the chosen fluence range is usually around [0.05, 0.6] J/cm^2.

[1] http://www.nctcog.org/trans/air/vehicles/health.asp

The purpose of this project was to study the temporal LII signal using laser pulse durations longer than 10 ns. Previous studies at SINTEF/NTNU (Ditaranto et al., 2013) have shown an unexpected feature in the LII signal for pulses with duration longer than 100 ns. A more detailed analysis of the relationship between pulse energy, pulse duration and fluence is essential when seeking a better understanding of this feature. Therefore, this experimental setup was set up so that the duration and fluence of the laser pulse could be varied. The LII measurements presented here are taken using laser pulses with duration between 50 ns to 450 ns. Measurements were first performed using a 532 nm laser beam, and later using a 1064 nm laser beam.

The theory behind the LII technique will first be discussed. Some results obtained in the previous studies at SINTEF/NTNU (Ditaranto et al., 2013) will then be presented for comparison. The experimental setup is explained, with special emphasis on the optical setup. Finally, experimental results for temporal LII measurements are presented and discussed.

2 Theory and Background

Laser Induced Incandescence is a technique used to observe soot particle size and concentration in a flame. Simply put, the method is based on hitting the soot particles in the flame with laser light and detecting the resulting radiation. The soot particles will absorb the laser light and in consequence reach a temperature well above the flame temperature. These small, hot particles will then emit black body radiation which can be detected and further analyzed.

2.1 Soot Morphology

Primary soot particles are small spherical particles of carbon with a diameter in the range of 10-40 nm which are created during combustion. These primary particles rapidly cluster into aggregates. Figure 2.1 shows a typical soot aggregate. The soot aggregates can contain up to thousands of particles, while still not being too densely packed. When talking about soot concentration in a flame, one must therefore consider the average size or diameter of the primary particles, the average number of primary particles per aggregate, and the number density of aggregates.

Since the aggregates are not too densely packed, several assumptions can be made (Zizak, 2000). The aggregates can be considered as composed of primary particles of diameter d_p touching at one point. Each particle is therefore regarded as independent and there is negligible heat transfer between the particles. Multiple scattering and temperature gradients inside the soot particle can also be neglected. The LII signal is thus based on the energy and mass balance of a single soot particle rather than the aggregate.

The soot volume fraction f_v is given by

$$f_v = \frac{\pi}{6} \cdot N \cdot n_p \cdot d_p^3 \tag{2.1}$$

where N is the number density of the aggregates, n_p is the average number of primary particles in the aggregate, and d_p is the diameter of the soot particle. It is assumed that all the primary particles are identical, and $N_p = N \cdot n_p$ is the density of these primary particles.

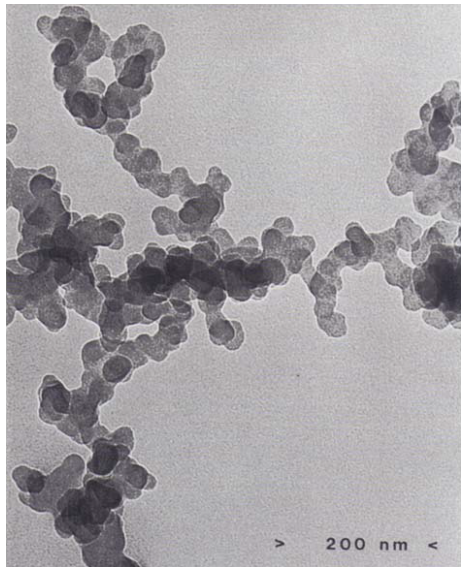

Figure 2.1: TEM image of typical soot aggregate (electron microscopy technique). Figure from (Dobbins and Subramaniasivam, 1994).

2.2 Nd:YAG Laser

Laser is an acronym for Light Amplification by Stimulated Emission of Radiation. Laser light is special due to the fact that it is highly collimated and has a high degree of coherence. The light will therefore spread very little when propagating over long distances. The light from common laser pointers are known for propagating over long distances and being able to focus on very a small area. High temporal coherence means the the light wave has a high correlation when observed at different moments in time. The laser's coherence is the reason it can emit a single color of light.

The different aspects of a laser will now be presented in order to give a better understanding of the Nd:YAG seed laser used in the experimental setup. The seed laser is a continuous wave laser (CW) that is later temporally pulse shaped within the Agilite laser system, see section 3.3.

2.2.1 Stimulated Emission, Absorption and Spontaneous Emission

An incident photon stimulates the creation of an identical, second photon. This is stimulated emission, also known as induced emission. Stimulated emission was theoretically discovered by A. Einstein using quantum theory (Einstein, 1916). A stimulated emitted photon is produced when an excited electron interacts with an incident photon and drops from a higher to a lower energy state. The incident photon has a frequency at or near the frequency of the transition, i.e. $h\nu \approx E_2 - E_1$.

Spontaneous emission is when an electron in an excited state decays to a lower state without any external influence. The excited electron releases its excess energy in the form of a photon when it decays. When such an excited electron decays into an unoccupied lower energy state, a photon is spontaneously emitted. The transition is associated with a particular time constant and the emitted photon will have energy $E_2 - E_1 = h\nu$.

Absorption is when the energy of an absorbed photon causes a transition from a lower to a higher energy level. Stimulated emission is a process identical in form to atomic absorption, only in the opposite transition. In thermal equilibrium, there are more electrons in the lower energy states than in the higher energy states. Absorption therefore exceeds stimulated emission. If the population in the higher state exceeds the population in the lower state however, the rate of stimulated emitted photons would exceed the rate of absorbed photons.

Figure 2.2 shows these three different processes. Since the population in the higher energy state must be larger for stimulated emission to dominate over absorption, an external energy source is needed that is not in thermal equilibrium with the system. This external source is the pump.

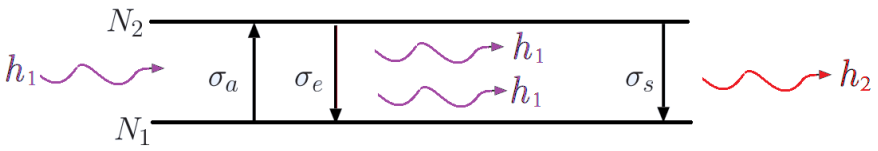

Figure 2.2: Sketch showing the three processes; absorption (σ_a), stimulated emission (σ_e) and spontaneous emission (σ_s). N_1 and N_2 represent the population in the lower and higher energy states. Figure modified from figure in (Papen, 2013).

Einstein came up with coefficients to describe the three processes which will only be mentioned here. The Einstein coefficient A_{21} gives the probability per unit time that an electron in state 2 with energy E_2 will decay spontaneously to state 1. The spontaneous emission lifetime is reciprocally $1/A_{21}$. Stimulated emission is described by the Einstein coefficient B_{21}. It gives the probability per unit time per unit spectral energy density of the

radiation field that an electron in state 2 with energy E_2 will decay to state 1 with energy E_1. Absorption is described by the Einstein coefficient B_{12}. The stimulated emission cross section used in the rate equation presented in section 2.2.3 is calculated using the Einstein coefficients [1].

2.2.2 Nd:YAG Gain Medium

The lasing material is Nd:YAG (neodymium-doped yttrium aluminum garnet) and thus a so-called 4-level laser. YAG $= Y_3Al_5O_{12}$, and it is an isotropic crystal. The YAG-crystal is Nd-doped by substituting some of the Y-ions in the crystal for Nd-ions. It is the possible energy transitions of Nd that makes lasing conditions possible. The Nd^{3+} in the crystal will be homogeneously broadened, have small linewidths, and will be limited to approximately 1% doping. The doping concentration is limited due to the diameter of the Nd-ion relative to the Y-ion for which it is substituted. Though it may not seem a lot, this concentration is sufficient to produce an efficient laser.

For a general gain medium to amplify light, an external supply of energy is needed. The energy is supplied either as an electrical current or the gain medium is optically pumped with light at a different wavelength. Nd:YAG lasers are optically pumped by either a flashtube or a laser diode. A laser diode is an electrically pumped semiconductor laser with an active medium that is a p-n junction. A pn junction is an interface between two types of semiconductor materials inside a crystal. The different materials are formed by doping, and the resulting semiconductor crystal is connected to two electrical outports. The term ”diode-pumped solid-state (DPSS) laser” refers to a solid-state laser made by pumping a solid gain medium with a laser diode. The most common DPSS laser in use is the 532 nm wavelength green laser pointer.

Nd:YAG lasers can be made to have both a pulsed and continuous wave (CW) mode. Laser operation of Nd:YAG was first demonstrated in 1964 by J. E. Geusic et al. (Geusic et al., 1964). As mentioned, the Nd:YAG seed laser in the Agilite laser system is a continuous wave laser.

Lasing Signal and Pump Wavelength

From Figure 2.3, we see that the operational wavelength of a Nd:YAG laser is 1064 nm. This is the $F_{3/2} \rightarrow I_{11/2}$ transition of Nd. As we see in the figure, we have two transitions with $\lambda \approx 1064$ nm; one with $\lambda = 1064.15$ nm and the other with $\lambda = 1064.4$ nm. Combining these two transitions, we can find an effective wavelength for the lasing transition $F_{3/2} \rightarrow I_{11/2}$ as $\lambda_{eff} = 1064.26$ nm. For many applications, the infrared light is frequency-doubled to obtain visible 532 nm green light.

[1] see (Verdeyen, 1995) for further details

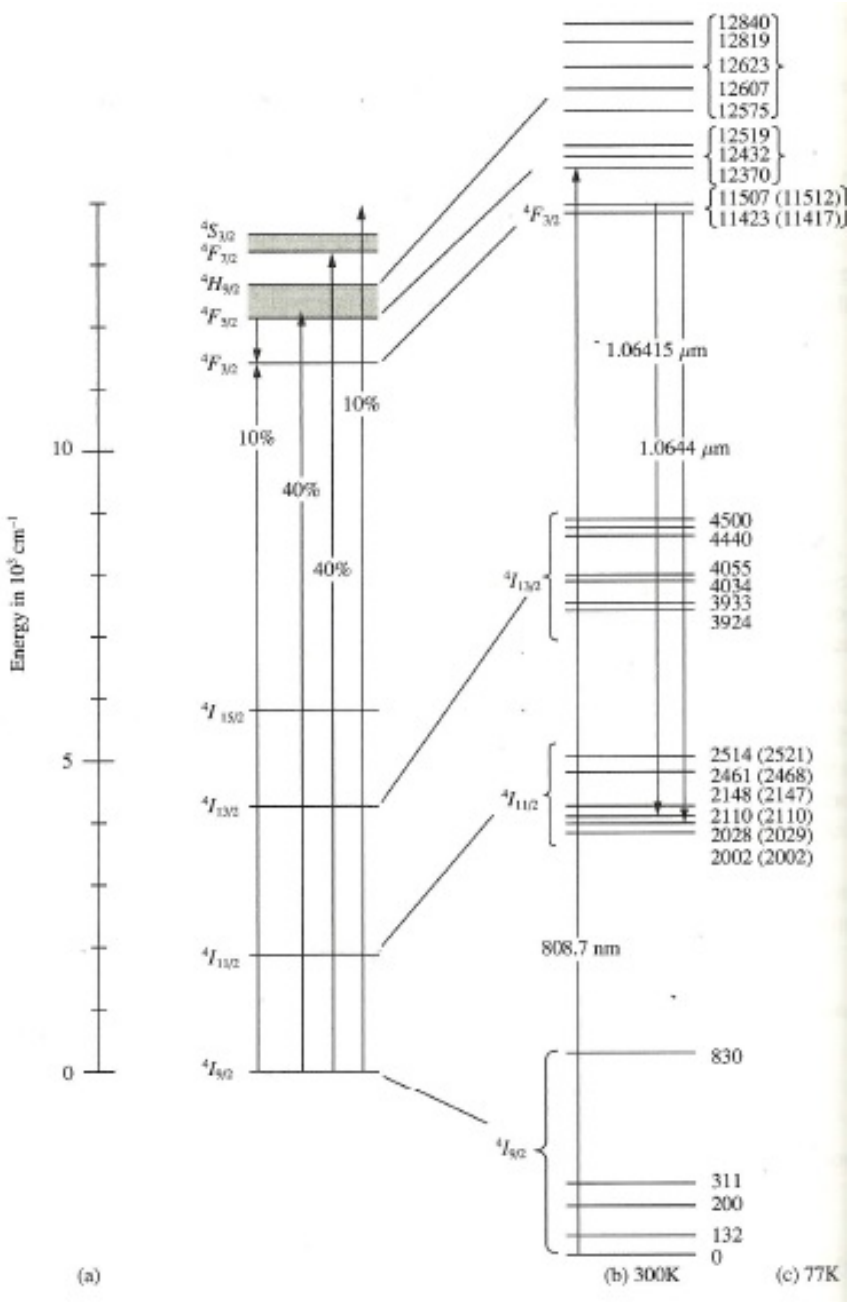

Figure 2.3: Diagram of the energy levels of Nd in YAG-crystal. All states have degeneracy 2. a) Structure of YAG showing the pumping routes with the percentage referring to a pump with a broad spectral output. b) Details of the manifold at 300 K showing the dominant transitions. The semiconductor laser pumping route is also shown. c) Energy levels at 77 K. Figure from (Verdeyen, 1995).

Both the $F_{3/2}$- and the $I_{11/2}$-manifold can be thought of as one energy level despite the Stark splitting we see in the figure. This is because the energy gap between the splitted energy levels is sufficiently small to allow for free exchange of energy between each other. The thermal energy $k_B T = 208$ cm^{-1} is a larger value than the energy gap between the splitted energy levels. A Boltzmann distribution thus exists in each manifold, and we approximate the splitted energy levels of a manifold instead as one effective energy level of that manifold. The lifetime of the $F_{3/2}$-manifold is $\tau_2 = 255$ μs.

As Figure 2.3 depicts, the ground state of the $I_{9/2}$-manifold is pumped to the $F_{5/2}$-manifold with pump wavelength $\lambda_p = 808.5$ nm. The $F_{5/2}$-manifold has a fast relaxation to the $F_{3/2}$-manifold. η_p is the fraction of atoms pumped into the $F_{5/2}$-manifold that relaxes to the the $F_{3/2}$-manifold. It is also called the pump efficiency.

From now on we will denote the lasing transition as the $N_2 \rightarrow N_1$ transition, and the pump transition as $N_0 \rightarrow N_3$. Fast relaxation of the N_3 state to the N_2 state lets us approximate $N_3 \approx 0$. Likewise, the lifetime of the N_1 state is 30 ns, much less than $\tau_2 = 255$ μs, and the fast relaxation to the ground state lets us approximate $N_1 = 0$. This approximation is depicted in Figure 2.4.

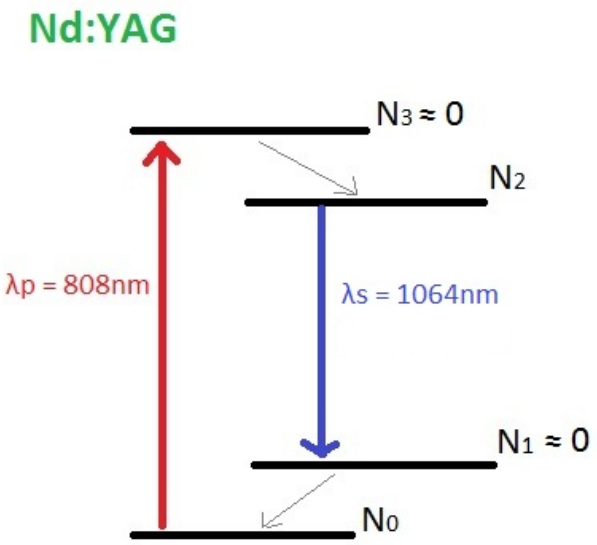

Figure 2.4: Approximate diagram of a 4-level Nd:YAG laser.

2.2.3 Rate Equations

Figure 2.4 depicts the approximations made to the 4-level laser. The corresponding rate equation is:

$$\frac{dN_2}{dt} = R_2 \cdot N_0 - \frac{1}{\tau_2} \cdot N_2 - \frac{\sigma(\nu) I_\nu}{h\nu}(N_2 - N_1) \tag{2.2}$$

where R_2 is the pump rate, τ_2 the upper state lifetime, ν is the frequency, $\sigma(\nu)$ is the stimulated emission cross-section and I_ν is the intensity of the lasing signal.

Inserting $N_1 \approx 0$ and depicting the difference more clearly between the pump and the lasing signal by inserting subindeces p and s, equation (2.2) becomes:

$$\frac{dN_2}{dt} = \frac{\sigma_p I_p}{h\nu_p} \cdot N_0 - \left(\frac{1}{\tau_2} + \frac{\sigma_s I_s}{h\nu_s} \right) \cdot N_2 \tag{2.3}$$

The saturation intensities of the lasing signal and of the pump is given by [2]

$$I_{ss} = \frac{h\nu_s}{\sigma_s \tau_2} \quad , \quad I_{sp} = \frac{1}{f_0 \eta_p} \frac{h\nu_p}{\sigma_p \tau_2} \tag{2.4}$$

where f_0 is the fraction of N_0 actually in the ground state and η_p is the pump efficiency, for example 90%. I_{ss} here stands for the saturation intensity of the lasing signal.

Inserting the two saturation intensities I_{ss} and I_{sp} into equation (2.3) gives

$$\frac{dN_2}{dt} = \frac{1}{\tau_2} \frac{I_p}{I_{sp}} N_0 - \frac{N_2}{\tau_2} \left(1 + \frac{I_s}{I_{ss}} \right) \tag{2.5}$$

Introducing new convention parameters:

$$P = \frac{I_p}{I_{sp}} \quad and \quad L = \frac{I_s}{I_{ss}} \tag{2.6}$$

Using P and L, the time dependent rate equation for N_2 becomes

$$\frac{dN_2}{dt} = \frac{N_0}{\tau_2} P - \frac{N_2}{\tau_2} (1 + L) \tag{2.7}$$

[2] see (Verdeyen, 1995) for further details

Continuous Wave Solutions

The continuous wave solution (CW) for the upper state N_2 is found by setting the derivate in equation (2.7) to zero.

$$N_2 = \frac{P \cdot N_0}{1 + L} \tag{2.8}$$

Combining equation (2.8) with $[Nd] \approx N_0 + N_2$, we get the CW-solution for N_0:

$$N_0 = \frac{[Nd]^0}{1 + \left(\frac{P}{1+L}\right)} \tag{2.9}$$

Inserting the solution for N_0 into equation (2.8) again, we get

$$N_2 = \frac{P \cdot [Nd]^0}{1 + L + P} \tag{2.10}$$

2.2.4 Optical Cavity

An optical cavity or optical resonator is basically mirrors surrounding the gain medium. Light that is confined within the optical cavity is reflected multiple times. The light consequently passes through the gain medium many times and the signal is thus amplified. The most common cavity consists of two spherical mirrors facing each other, one on each side of the gain medium. Two opposing plane mirrors are also commonly used, but alignment here is difficult for large-scale lasers. Another way to create a cavity is to apply reflective optical coating to the sides of the gain medium itself, thus skipping additional mirrors completely.

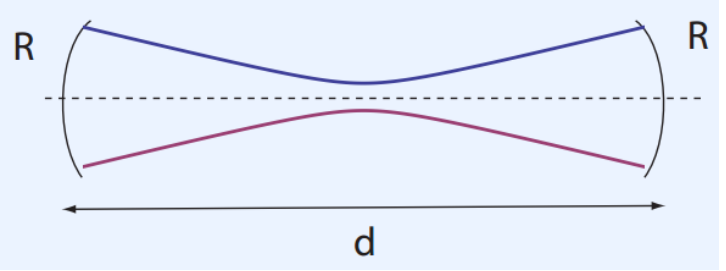

Figure 2.5: Sketch of an optical cavity. The field curvature of Gaussian beam must match at the mirrors with curvature $R_1 = R_2 = R$ as shown. The distance between the mirrors is d. Figure from (Papen, 2013).

An optical resonator with two mirrors of curvature R_1 and R_2 can have many cavity configurations. However, only certain values of curvature and cavity length produce stable resonators. Figure 2.5 shows the Gaussian beam inbetween the two spherical mirrors. The field curvature of the Hermite-Gaussian mode must match at mirrors R_1 and R_2 (Verdeyen, 1995), see section 2.2.5 on Gaussian beams. If the resonator is unstable, the size of the beam will grow until it escapes the cavity. Ray Optics is used to ensure that stability criteria are met.

Ray transfer matrix analysis can be used for Gaussian beams by defining a complex beam parameter q given by

$$\frac{1}{q} = \frac{1}{R} - \frac{i\lambda_0}{\pi n w^2} \tag{2.11}$$

where λ_0 is the Gaussian beam's wavelength, R is the radius of curvature, w is the beam spot size and n is the refractive index.

In ray optics, optical components are each represented by a matrix. An optical system's transfer matrix is the resulting matrix from all optical components using matrix multiplication. When a Gaussian beam propagates through an optical system, the resulting Gaussian beam is found by multiplying this system's optical transfer matrix with the initial Gaussian beam's matrix, i.e.

$$\begin{bmatrix} q_2 \\ 1 \end{bmatrix} = \begin{bmatrix} AB \\ CD \end{bmatrix} \begin{bmatrix} q_1 \\ 1 \end{bmatrix} \tag{2.12}$$

Here q_1 is the initial Gaussian beam's complex beam parameter and q_2 is the beam parameter after propagating through the optical system defined by the transfer matrix $\begin{bmatrix} AB \\ CD \end{bmatrix}$.

A stable cavity will have q(start) = q(round trip). This leads to the ABCD-criterion for a stable optical resonator given by equation (2.13)[3].

$$0 \leq \frac{A + D + 2}{4} \leq 1 \tag{2.13}$$

Another way to write this stability criterion is using the curvature of the cavity's mirrors and the optical path length L. The values for R_1, R_2 and L which satisfy equation (2.14) below corresponds to a stable resonator.

$$0 \leq \left(1 + \frac{L}{R_1}\right)\left(1 + \frac{L}{R_2}\right) \leq 1 \tag{2.14}$$

A confocal cavity design is a stable design consisting of two spherical mirrors with the same radii of curvature and the curvature equal to the length of the cavity, in other words $R_1 = R_2 = L$. For an optical cavity containing a gain medium, the cavity length L is defined as the optical path length between the mirrors. The confocal alignment is least sensitive among all the various configurations. Figure 2.6 graphically depicts the possible alignments of equation (2.14).

[3] for derivation, see (Verdeyen, 1995)

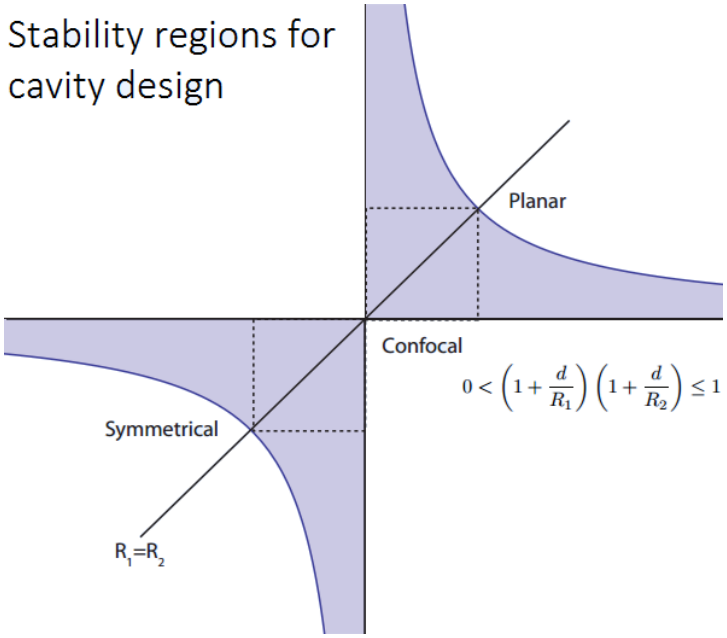

Figure 2.6: Stability regions of an optical two-mirror cavity (shaded region). The curvature of the mirrors is R_1 and R_2 and d is the length of the cavity. Figure from (Papen, 2013).

When the output beam from the laser is known, further ray matrix analysis can be done for the optical components used in experiments with the laser. The change applied to the initial ray can be calculated by finding the optical system's transfer matrix and multiplying this with the initial beam's matrix representation.

2.2.5 Gaussian Beam Profile

The normal or Gaussian distribution is a continuous distribution given by the mathematical formula

$$f(x) = \frac{1}{\sqrt{2\pi}\sigma} e^{-\frac{(x-\mu)^2}{2\sigma^2}} \tag{2.15}$$

where μ is the mean value and σ is the standard deviation.

Most optical beams propagating in free space are almost pure TEM waves (Transverse ElectroMagnetic). The electromagnetic field components lie perpendicular to the direction of propagation. From Maxwell's equations, the paraxial wave equation can be derived [4].

[4] for derivation, see (Verdeyen, 1995)

Equation (2.16) is the paraxial approximation of the Helmholtz equation and has incidentally the same form as the time-dependent Schrödinger equation.

$$\nabla_{\perp}^2 \psi + i2k\frac{\partial \psi}{\partial z} = 0 \tag{2.16}$$

where $\nabla_{\perp}^2$ is the transverse part of the Laplacian, i.e. equal to $\frac{\partial^2}{\partial x^2} + \frac{\partial^2}{\partial y^2}$ when the light propagates in the z-direction.

Equation (2.16) provides solutions in the form of either paraboloidal waves or Gaussian beams. The TEM_{00} mode is the fundamental lowest-order mode and it is shown in Figure 2.7.

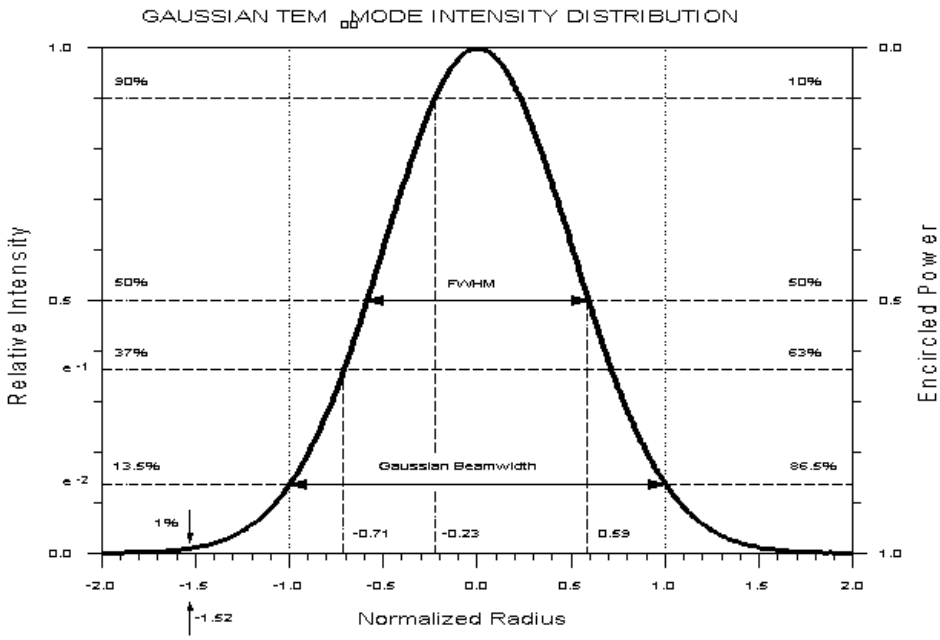

Figure 2.7: Gaussian TEM_{00} mode intensity distribution, depicting the Gaussian beamwidth. Figure from http://www.coseti.org/9101-001.htm.

The radial intensity distribution of the TEM_{00} mode is of a Gaussian distribution and given by equation (2.17).

$$I(r) = I_0 e^{-\frac{2r^2}{w_0^2}} \tag{2.17}$$

where r is the radial distance from the center of the beam, I_0 is the peak intensity equal to I(r=0), and w_0 is the Gaussian radius of the beam or also called the $1/e^2$-width. As Figure 2.7 depicts, the so-called $1/e^2$-width is the distance between the two points that are $1/e^2$ = 13.5 % of the maximum value. The Gaussian beamwidth is thus $2w_0$.

Fluence is the energy or intensity applied per area and given in J/cm^2. The beam's area is πw_0^2. The irradiance of the beam is the time-averaged intensity distribution given in power per unit area or W/cm^2. The average energy measured by an energy detector is the integrated Gaussian intensity distribution. This value will then of course be somewhat lower than the peak energy of the Gaussian laser beam.

$$Fluence = \frac{Energy}{Area} = \frac{E_{pulse}}{\pi w_0^2} \quad [J/cm^2] \tag{2.18}$$

$$Irradiance = \frac{Energy}{pulse\ duration \cdot Area} = \frac{E_{pulse}}{\tau \cdot \pi w_0^2} \quad [W/cm^2] \tag{2.19}$$

Depending on the cavity, the laser beam can be of a higher-order TEM mode with very different intensity distributions. The higher-order Hermite-Gaussian modes are governed by the Hermite polynomial H_n of n^{th}-order. The intensity distribution of order mn is given by equation (2.20), where insertion of $m, n = 0, 0$ gives equation (2.17) again.

$$I_{mn}(x, y, z) = I_0 \cdot \left(H_m(\frac{\sqrt{2}x}{w}) \cdot e^{-\frac{x^2}{w^2}} \right)^2 \cdot \left(H_n(\frac{\sqrt{2}y}{w}) \cdot e^{-\frac{y^2}{w^2}} \right)^2 \tag{2.20}$$

The laser beam used in this project is of Gaussian TEM$_{00}$ mode as depicted in Figure 2.7, which is verified in section 3.4 by studies of the laser's spatial beam profile.

2.3 Laser Induced Incandescence

2.3.1 Energy Balance of a Soot Particle

The general energy balance for a spherical particle that absorbs laser energy is given by

$$E_{abs} = E_{cond} + E_{vap} + E_{rad} + E_{int} \tag{2.21}$$

Here E_{abs} is the absorbed energy from the laser light, E_{cond} is the energy loss due to heat conduction toward the surroundings, E_{vap} is the energy loss due to vaporization of soot carbon, E_{rad} is the energy loss due to black body radiation, and finally E_{int} is the energy used for internal temperature raise. Figure 2.8 is a schematic representation of this energy balance.

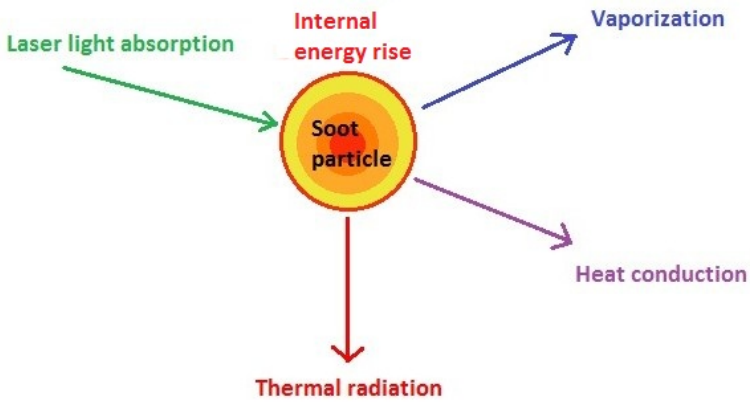

Figure 2.8: Schematic representation of the energy balance of a soot particle that absorbs energy from the laser light. Each physical phenomenon is a contributing term in equation (2.21).

In the original and pioneering paper by L. A. Melton (Melton, 1984), a model of the energy balance is presented using the rate of energy loss and the temporal profile of the laser pulse, $q(t)$. Equation (2.22) is this model.

$$K_{abs}\pi a^2 \cdot q(t) \;=\; 4\pi a^2(T - T_0)\Lambda + \left(\frac{\Delta H_v}{W_s}\right)\frac{dM}{dt} + q_{rad} + \frac{4\pi a^3}{3}\rho_s C_s \frac{dT}{dt} \quad (2.22)$$

The different contributing terms in this energy balance equation will now be introduced.

Absorption of the laser energy is given by the absorption coefficient K_{abs}, the particle radius a, and the temporal profile of the laser pulse $q(t)$. K_{abs} is in turn dependent on the absorption wavelength λ, the radius a, and the complex index of refraction for soot $m = n + ik$.

$$K_{abs} \;=\; \frac{8\pi a \cdot E(m)}{\lambda} \quad (2.23)$$

where $E(m) = 6nk/((n^2 - k^2 + 2)^2 + 4n^2k^2)$ and is thus dependent on the complex index of refraction of soot for a given laser wavelength. It has been found that when $\lambda = 532$ nm, $m = 1.59 + 0.58i$ and thus $E(m) = 0.264$ (Dalzell and Sarofim, 1969).

Heat conduction towards the surroundings gases is given by the conductivity Λ of the soot particle. Since the size of the primary particles is on the order of or smaller than the mean free path in the surrounding gases, the conductivity is found by considering the soot as both free molecules and as being in continuum transfer regimes. A conference paper by

G. Zizak (Zizak, 2000) on LII of soot presents:

$$\Lambda \;=\; \frac{K_a}{a(1+GK_n)} \;=\; \frac{K_a}{a(1+\frac{8f}{\alpha(\gamma+1)}\frac{l}{2a})} \tag{2.24}$$

where K_a is the thermal conductivity in the gas and $K_n = \frac{l}{2a}$ is the Knudsen number, i.e. the ratio between the mean free path length and the diameter of the particle. G is a geometric factor given by $G = (8f/\alpha(\gamma+1))$, where $f = 5/2$, $\alpha = 0.9$ and $\gamma = 1.4$ (air).

Vaporization of soot carbon is given by the heat of vaporization ΔH_v of carbon, the molecular weight of solid carbon $W_s = 12$ g/mol, and the rate of mass vaporization dM/dt. The continuity equation for the rate of particle mass in the transition from solid carbon to carbon vapor is given by equation (2.25).

$$\frac{dM}{dt} \;=\; 4\pi a^2 \cdot \rho_s \frac{da}{dt} \;=\; 4\pi a^2 \cdot \rho_v U_v \tag{2.25}$$

where ρ_s is the density of solid carbon, ρ_v is the density of carbon vapor, and U_v is the vapor velocity.

In accordance with (Eckbreth, 1996) and (Zizak, 2000), the vapor velocity U_v is assumed to be the thermal velocity $\sqrt{(RT/2W_v)}$. The molecular weight of carbon vapor, W_v, is taken as 36 g/mol. R is the gas constant. The ideal gas law, $pV = nRT$, gives the density of carbon vapor as

$$\rho_v = \frac{W_v}{R} \cdot \frac{p(T)}{T} \tag{2.26}$$

Here the temperature dependent pressure $p(T)$ is found by the Clapeyron formula:

$$p(T) = p(T^*) \cdot exp\left(\frac{\Delta H_v (T - T^*)}{RTT^*}\right) \tag{2.27}$$

where T^* is the temperature at which the pressure $p(T = T^*) = 1$ atm. For carbon, the sublimation point (solid to gas) is $T^* = 3195$K.

Radiation from the soot particle is black body radiation. Stefan-Boltzmann's law gives the total power radiated from an object:

$$E_{rad} \;=\; \epsilon \cdot A_{surface} \cdot \sigma T^4 \tag{2.28}$$

The radiative transfer energy from a laser heated soot particle is thus

$$Q_{rad} \;=\; \epsilon \cdot 4\pi a^2 \cdot \sigma(T^4 - T_0^4) \tag{2.29}$$

where ϵ is the soot emissivity. ϵ can be set equal to the absorption coefficient K_{abs}. σ is the Stefan-Boltzmann constant. T is the temperature of the soot particle with radius a, and T_0 is the temperature of the surrounding flame.

The internal energy rise of the soot particle is dependent on its volume, the specific heat capacity of carbon C_s, the soot density ρ_s and the temperature change ΔT.

$$Q_{int} = \frac{C_s}{m}\Delta T \tag{2.30}$$

$$q_{int} = \frac{4\pi a^3}{3}\rho_s C_s \frac{dT}{dt} \tag{2.31}$$

The parameters for soot are $C_s = 1.9$ J/gK and $\rho_s = 2.2$ g/cm^3.

Annealing and oxidation. Not included in equation (2.21) and (2.22) is the contribution from annealing and oxidation processes. Annealing is a heat treatment that alters the microstructure of a material, which in turn causes changes to its properties.

As discussed in section 2.1, soot generated by flames is typically comprised of branched chains of small primary particles held together. According to Michelsen (Michelsen, 2003), the primary particles will at temperatures above 2500 K anneal to form carbon onions and other ordered phases of carbon. The absorption cross section changes as the particle anneals and its emissivity decreases. The morphological changes to the soot is further discussed in section 2.4.3.

2.3.2 LII Signal Formula

By numerically integrating equation (2.22), the time dependent particle radius $a(t)$ and temperature $T(t)$ can be found. In order to do so, one must know the flame temperature T_0, initial particle radius a_0, and the laser excitation wavelength λ. λ is 532 nm or 1064 nm in this project.

The LII-signal is given by

$$LII(\lambda_0, t) = \frac{C_1}{{\lambda_0}^5} \cdot exp\left(\frac{C_2}{\lambda_0 T(t)} + 1\right) \cdot N_p \cdot 4\pi a^2(t) \cdot \epsilon(t) \cdot \Delta\lambda \tag{2.32}$$

where C_1 and C_2 are the first and second Planck constants, N_p is the density of primary particles, and $\Delta\lambda$ is the spectral bandwidth of detection around the central wavelength λ_0.

The LII signal at maximum temperature is called "prompt LII". Melton (Melton, 1984) showed that

$$LII_{prompt} \propto N_p \cdot {d_p}^{(3+154nm/\lambda_{det})} \tag{2.33}$$

where again d_p is the particle diameter (=2a). The exponent $(3 + 154nm/\lambda_{det})$ is dependent on the detection wavelength. When the exponent is about 3, the prompt LII signal is proportional to the soot volume fraction, given by equation (2.1). Theoretical models have been developed to describe the heating and the cooling of the particles by solving these energy and mass balance equations.

2.3.3 Theoretical Models of LII Signal

Theoretical models for the interaction between laser light and soot particles have been developed and are much used. One such model is called LIISim (Hofmann et al., 2007) and even a web interface for it is available. As it promotes, LIISim is ”a software to simulate LII signals as well as for fitting experimental LII signal traces in order to determine particle sizes”. A model for the LII signal makes it possible to study the influence of different parameters on its behavior. LIISim can even solve the energy and mass balance for both single soot particles and for soot aggregates.

As equation (2.33) shows, the prompt LII signal is proportional to soot particle diameter and the density of primary particles. It is therefore sufficient to only look at this part of the LII signal. Q-switched Nd:YAG lasers with pulse duration of about 10 ns is traditionally used. Such a laser pulse will result in a LII signal lasting about 100 ns and they will look much like the signal shown in Figure 2.10. This signal will then either be integrated soon after the ”prompt” LII signal, or it will be integrated over a time frame longer than the pulse itself lasts, for example 200 - 700 ns. This latter technique is used in order to avoid PAH fluorescence influencing the LII signal, see section 2.4.1.

2.4 Experimental LII Signal Features

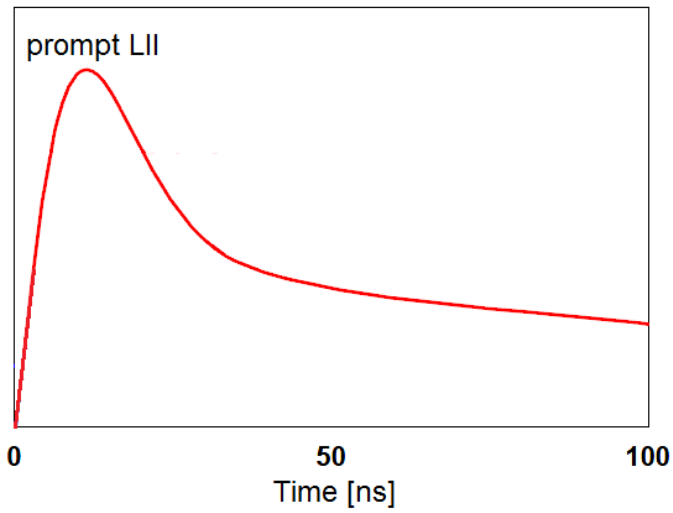

Figure 2.9: Simplified example of a typical LII signal in time. The laser pulse hitting the flame has 10 ns pulse duration, but the LII signal lasts much longer than this. The peak of the signal, or prompt LII, lasts about 20 ns.

Figure 2.9 shows a simplified example of a typical time-resolved LII signal. The peak of the LII signal lasts in this case only about 20 ns, but the LII signal itself lasts more than 100 ns. This shows how the temperature decays in a much longer time frame than the laser pulse duration. The temperature decay curve is dependent on the particle's diameter since smaller particles cool down faster.

Temperature decay curves have been calculated for different laser power densities. For example, the temperature in time of a 40 nm diameter soot particle was studied for three different laser power densities; low, high and medium (Zizak, 2000). It was found that for low laser power density (10^6 W/cm^2), the absorbed energy was simply used to heat the particle.

For medium laser power density however, the soot particle reached a temperature that slightly exceeded the vaporization temperature. The peak temperature of the heated soot particle is just at the beginning of the pulse, and it increased with increasing power. When the fluence of the laser pulse used was increased, the prompt LII signal increased while its duration decreased. In other words, the peak of the signal became sharper with increasing laser power.

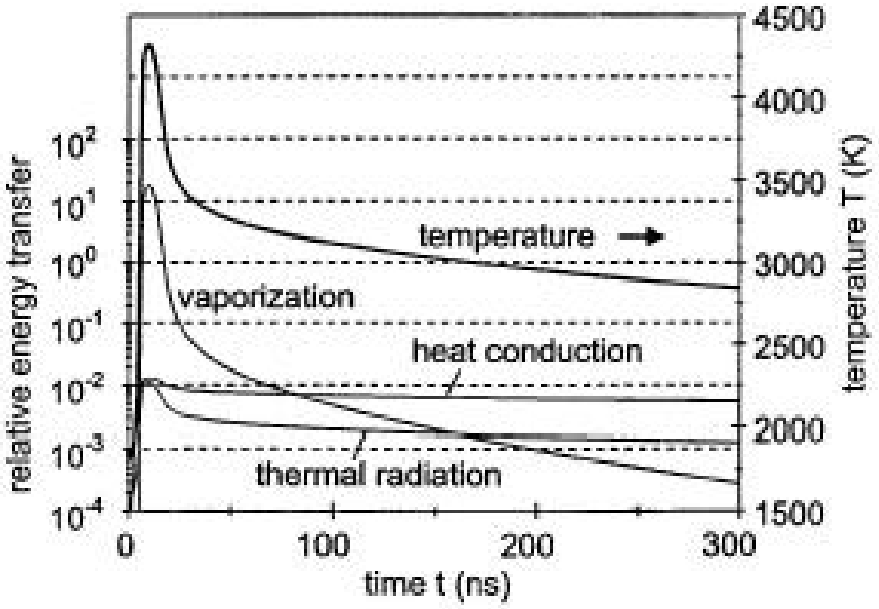

Figure 2.10: Comparison of the different heat loss processes involved in the time-resolved LII signal. Vaporization is the dominating process up to about 100 ns, whereas heat conduction contributes the most to the temperature decay after that. Figure originally from (Will et al., 1998), and also used in (Zizak, 2000).

For very high laser power density (10^8 W/cm^2), the temperature of the particle increased enormously and strong vaporization occurred. The peak temperature was found to be almost independent of the soot particle's diameter, indicating that strong vaporization and mass reduction had occurred.

The relative importance of the energy loss mechanisms in equation (2.21) is shown in Figure 2.10. The graph shows how vaporization dominates up to about 100 ns. After 100 ns, heat conduction is the major contributer to the soot particle's temperature decay. As seen in the figure, the different physical processes involved in heating and cooling of the soot particle have different rates.

For a 532 nm laser excitation wavelength, C. J. Dasch reported a fluence of 0.23 J/cm^2 as the threshold for soot vaporization effects (Dasch, 1984b). A similar threshold value of 0.2 J/cm^2 has been found for time-resolved LII experiments (Michelsen et al., 2003). The threshold value for 1064 nm laser light lies around 0.4 - 0.5 J/cm^2.

2.4.1 PAH-fluorescence

As mentioned before, combustion-generated pollutants are notably soot, but also by-products such as organic carbon nanoparticles (NOC) and polycyclic aromatic hydrocarbons (PAH). There is some uncertainty in how much PAH-fluorescence influences the LII signal, especially when using laser pulses of long duration as in this project. In the flame, there are contributions from PAH-fluorescence as well as LII and Mie scattering from soot.

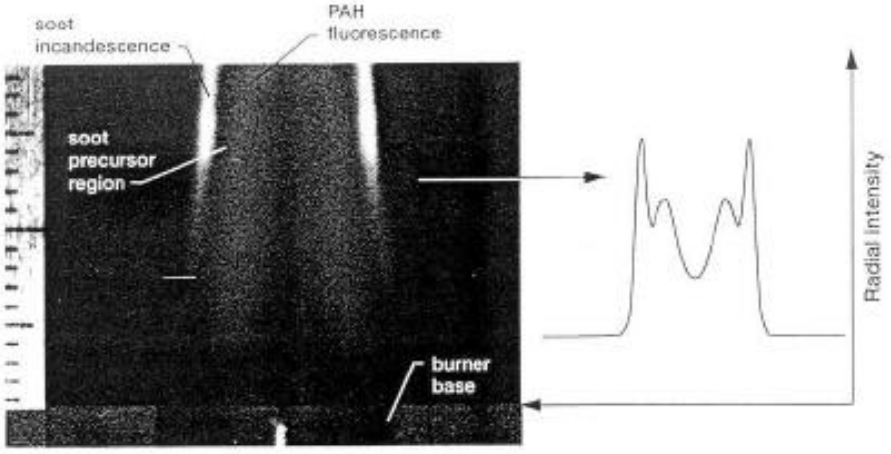

Figure 2.11: Visualization of soot and PAH regions within an ethylene diffusion flame. From (Wal et al., 1997).

PAH are considered as precursors of soot. The molecules present absorption bands in the UV and a red-shifted emission in the UV-VIS part of the spectrum (Zizak, 2000). Vander Wal simultaneously visualized soot LII and PAH-fluorescence by the use of the fourth-harmonic of a pulsed Nd:YAG laser (Wal et al., 1997).

Figure 2.11 shows a visualization of the structure of a diffusion flame, highlighting the different regions of the flame. Figure 2.12 shows radial intensity profiles containing contributions from both LII of soot and laser-induced fluorescence (LIF) from PAH.

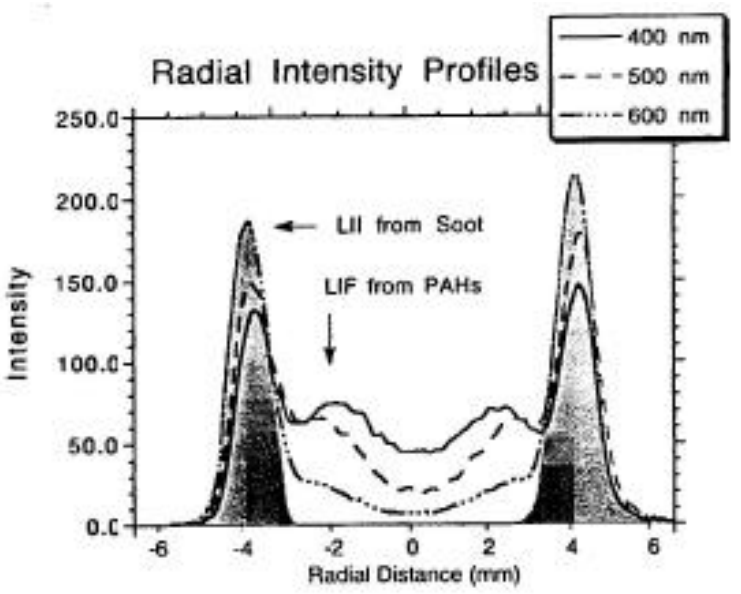

Figure 2.12: Radial intensity profiles of simultaneous LII/LIF images using a 266 nm laser beam. The label shows the band pass interference filter being used. The annular soot containing region is denoted by the shaded region. Figure from (Wal et al., 1997).

The LII signal is the increased temperature radiation from soot particles that have been heated to temperatures of several thousand degrees as a consequence of absorption of laser radiation. In an article by Bengtsson and Aldn (Bengtsson and Aldn, 1995), the dependence of the signals on experimental parameters were studied. The influence of interfering radiation such as the background flame luminosity and fluorescence from PAH on the studied signals was established. It was found that when the laser's intensity increased, so did the PAH-fluorescence.

When soot is formed it is accompanied by the formation of large aromatic hydrocarbons. It can be difficult to spectrally distinguish between the LII signal and the LIF signal caused by PAH. In the visible spectral region, both signals give rise to a broadband spectrum. However, the smaller PAH-molecules absorb in the ultraviolet region, and the larger

ones also absorb in the visible spectrum. Laser-induced PAH-fluorescence is therefore not possible when a laser beam with wavelength in the infrared spectrum is used. In Figure 2.12, the shown LII profiles have been verified by LII images obtained with a 1064 laser beam (Wal et al., 1997).

2.4.2 C_2-radicals and Carbonaceous Particles

The LII technique is based on the fact that soot particles strongly absorb laser radiation in a large spectral region from the UV to the IR. Even for relatively low laser intensity, $\approx 10^7$ W/cm^2, the soot particles are heated to temperatures above 4000 K. The background flame has a much lower temperature of about 1500-2000 K. The LII signal is therefore distinguishable from the background luminosity of the flame.

For high laser intensities, the soot particles in the flame will vaporize. Some of the laser energy will be used to raise the energy level of the vaporized carbon molecules. Since soot particles mainly consist of carbon atoms in a disordered graphite structure, large amounts of molecular carbon species are produced during vaporization (Bengtsson and Aldn, 1995). Previous studies have demonstrated that carbon atoms are released from soot due to laser impact (Michelsen et al., 2007).

The produced carbon molecules are assumed to range from C_1 to C_7, depending on particle temperature (Schulz et al., 2006). The excited carbon molecule will in turn emit visible light to release its excess energy. The visible emissions from C_2-radicals can be quite strong and interfere with the LII signal.

2.4.3 Morphological Changes Caused by Laser Impact

Intense laser radiation changes the properties of the soot particles, both structural and morphological. According to Schulz et al., these changes can occur even below the sublimation threshold (Schulz et al., 2006). Van der Wal et al. showed in 1998 TEM images of laser-heated soot extracted from a flame (Wal and Jensen, 1998). The laser light was of 1064 nm wavelength and images were taken using different laser fluences.

At 0.15 J/cm^2 fluence, no significant changes were seen. A doubling of the fluence however, caused the soot's structure to change to hollow particles. Further doubling of the fluence created TEM images where several carbon layers or carbon onion rings appeared at the perimeter of the particles. Finally, at 0.9 J/cm^2 the soot aggregates had lost much of its original material.

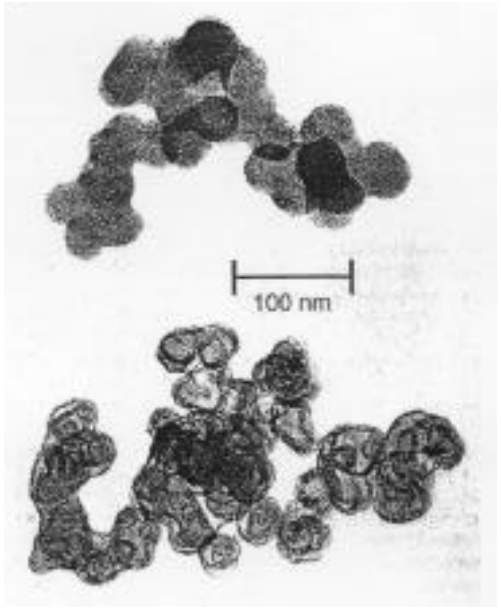

Figure 2.13: TEM images of typical soot aggregates in a flame. The bottom aggregate shows soot that has been heated by the laser. Figure from (Wal and Jensen, 1998)/(Zizak, 2000).

A change in structural and morphological characteristics will in turn have an effect on the absorption and emission cross-sections of the soot. The absorption cross section was found to change as the particle anneals and its emissivity decreased. If a particle anneals during laser impact, the integrated value of the laser heating term in equation (2.22) is reduced.

Previous articles had suggested that the soot aggregates break apart into primary particles during laser heating. However, the studies performed by Van der Wal et al. indicate that soot aggregates do not "disaggregate" or break apart into primary particles when subjected to 1064 nm laser pulses. Several other studies [5] have also supported the theory that the aggregates do not break apart, but that changes observed in scattering and absorption likely are caused by a decrease in primary particle size due to vaporization.

Michelsen et al. investigated more closely in 2007 the physical and chemical changes induced in soot aggregates exposed to laser radiation (Michelsen et al., 2007). Michelsen et al. found that the soot aggregates did not appear to break apart into "freed" primary particles. Instead, extensive new particle production was observed to occur at fluences above 0.12 J/cm^2 when using 532 nm laser, and above 0.22 J/cm^2 when using 1064 nm laser light. The studies indicate that the new particles are formed by nucleation of small carbon clusters generated by sublimation or photodesorption.

[5] see (Dasch, 1984a), (Witze et al., 2001) and (Yoder et al., 2005).

2.4.4 Typical Laser Parameters Used in LII measurements

In a paper by Schulz et al., the typical laser beam parameters in LII testing scenarios are discussed. "Nd:YAG lasers are frequently used for LII excitation because these lasers are generally reliable, readily available and provide high-power pulses with typical pulse durations of 8-15 ns. The fundamental (1064 nm) or second harmonic (532 nm) are most often used for LII applications."(Schulz et al., 2006)

In the paper, emphasis is also put on the fact that care must be taken with the strategy used for both excitation and detection in order to avoid non-LII signal interferences. Three main reasons are given for why excitation with 1064 nm results in less interference than laser light of 532 nm or shorter wavelengths. First, LIF of PAH is induced with excitation in the visible and the UV spectral region. Secondly, generation of electronically excited C_2 fragments is less pronounced for longer wavelengths. Excited C_2 emission is short-lived and the interference occurs only during the laser pulse and decays quickly thereafter.

As mentioned in section 2.4.2, the visible emissions from C_2 can be quite strong for high intensity excitation. Delayed detection is often used to minimize this interfering contribution in the signal (Schulz et al., 2006).

In addition to interferences from PAH and C_2, elastically scattered light is very strong in sooting flames (Schulz et al., 2006). There is a good chance that the elastically scattered 532 nm light is not be entirely blocked by an interference filter. This would then cause a perturbation to the LII signal.

The 1064 nm light is on the other hand not in the visible spectrum and will thus not be detected by an ICCD camera. An infrared laser beam would therefore not interfere with the LII signal through elastic scattering. However, the 532 nm laser beam has the obvious advantage of being visible to the naked eye, while optical components when using an infrared laser beam must be aligned by looking through a beam viewer.

2.5 Previous Experiments with Long Pulse Duration

Mario Ditaranto and Christoph Meraner first reported using a laser pulse duration longer than 50 ns (Ditaranto et al., 2013). They observed an unexpected feature in the temporal LII signal for pulse durations longer than 100 ns. As shown in Figure 2.14, a second peak emerges for the longer pulse durations.

The figures presented in this section are based on experimental results obtained by C. Meraner for SINTEF Energy (Ditaranto et al., 2013). In all graphs, the original rectangular laser pulses are represented by a dashed line and shown together with the corresponding LII signal (solid line).

An intensified CCD camera collected intensity images as the one shown in Figure 2.18. The images were taken with a 10 ns gate width, or camera opening time. The temporal LII signals presented in the following figures were collected throughout a 800 ns or longer time frame. At each time step, 10 images were accumulated on-chip before being sent to the computer.

The 532 nm laser beam was focused with a spherical lens of 1 m focal length. This was combined with a cylindrical lens of -45 mm focal length. These optical components were included in order to create a laser sheet. The LII signal was collected by a lens of 249 mm focal length which focuses the light to the ICCD camera. In this collection path is also a 10 nm band-pass interference filter centered at 488 nm and a 532 nm notch filter. The same collection lens and filters are used in this project's experimental setup.

A more detailed analysis of the relationship between pulse energy, pulse duration and fluence is essential when trying to get a better understanding of the unexpected second peak feature. The aim of this project was to repeat the experimental program previously done, but this time with a better control of the laser pulse fluence and the laser beam's spatial profile.

Constant pulse fluence or total energy, using different pulse durations

Figure 2.14 shows the temporal LII signal using different pulse durations, but constant fluence. A second peak feature is clearly visible for the pulses of a 100 ns duration or longer.

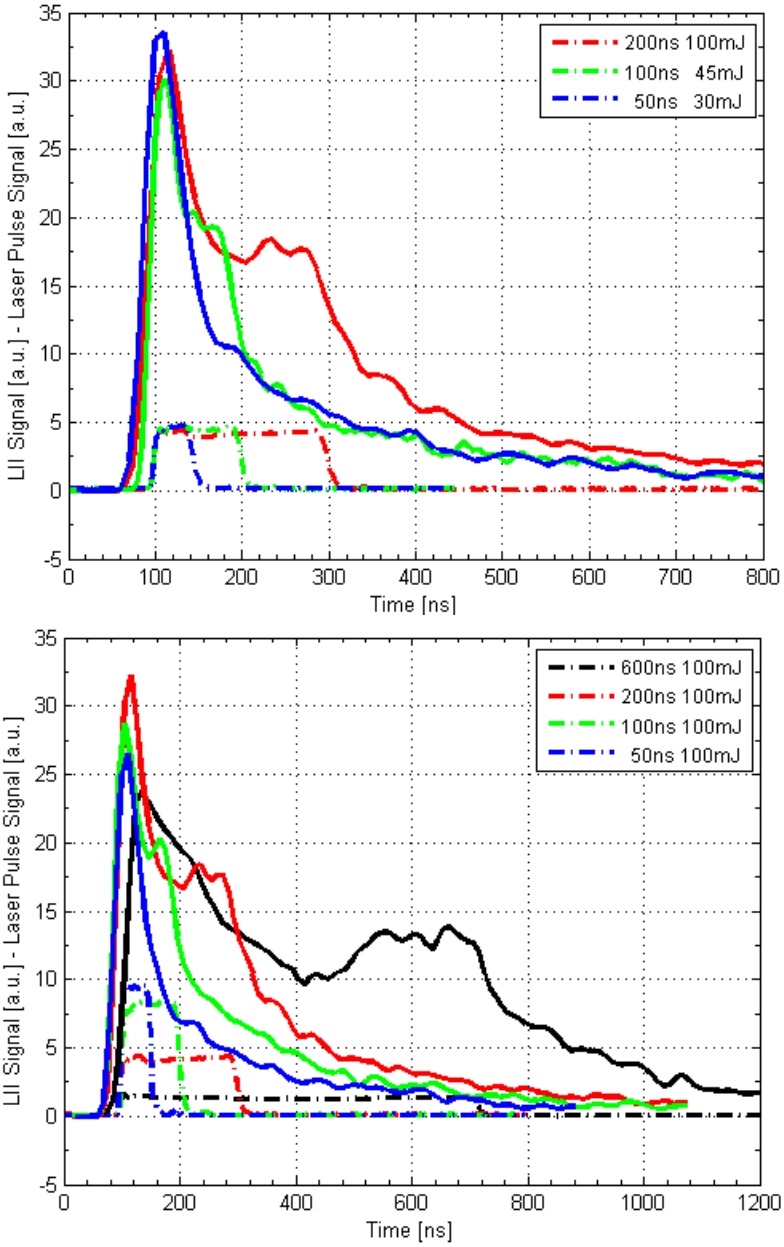

Figure 2.14: Temporal LII signal using different pulse durations. The original rectangular laser pulses (dashed line) are shown together with the corresponding LII signal (solid line). The top figure shows the temporal LII signals using three pulses of different pulse durations but equal intensity. A second peak feature is clearly visible for the pulses of a 100 ns duration or longer. The bottom figure shows the temporal LII signals using three pulses of different pulse durations with the same total pulse energy. (Ditaranto et al., 2013)

Different temporal laser pulse profiles, constant pulse duration

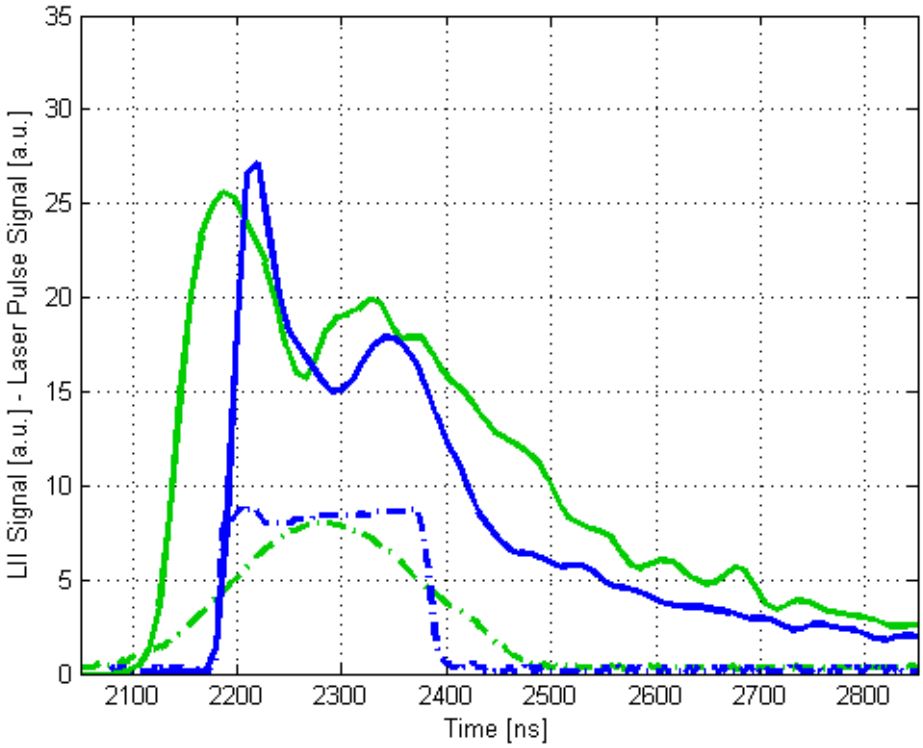

Figure 2.15: Temporal LII signal using different temporal pulse shapes, rectangular and near-gaussian as shown by the dashed lines. The second peak feature is visible for both pulse shapes, rejecting the temporal profile as the sole cause of the second peak. (Ditaranto et al., 2013)

Different total pulse energies, constant pulse duration

Figures 2.16 and 2.17 show LII signals for four different pulse durations, 50 ns - 600 ns, with varying pulse energies. For the laser pulses of 100 ns duration or longer, the second peak is clearly visible. It is also seems to be linked to the amount of energy applied, as its visibility increases with increasing energy. For the low pulse energies in Figure 2.17, the pink colored 6 or 12 mJ curves, the signal has changed its shape and the second peak is not seen. This suggests a threshold energy for the second peak to occur.

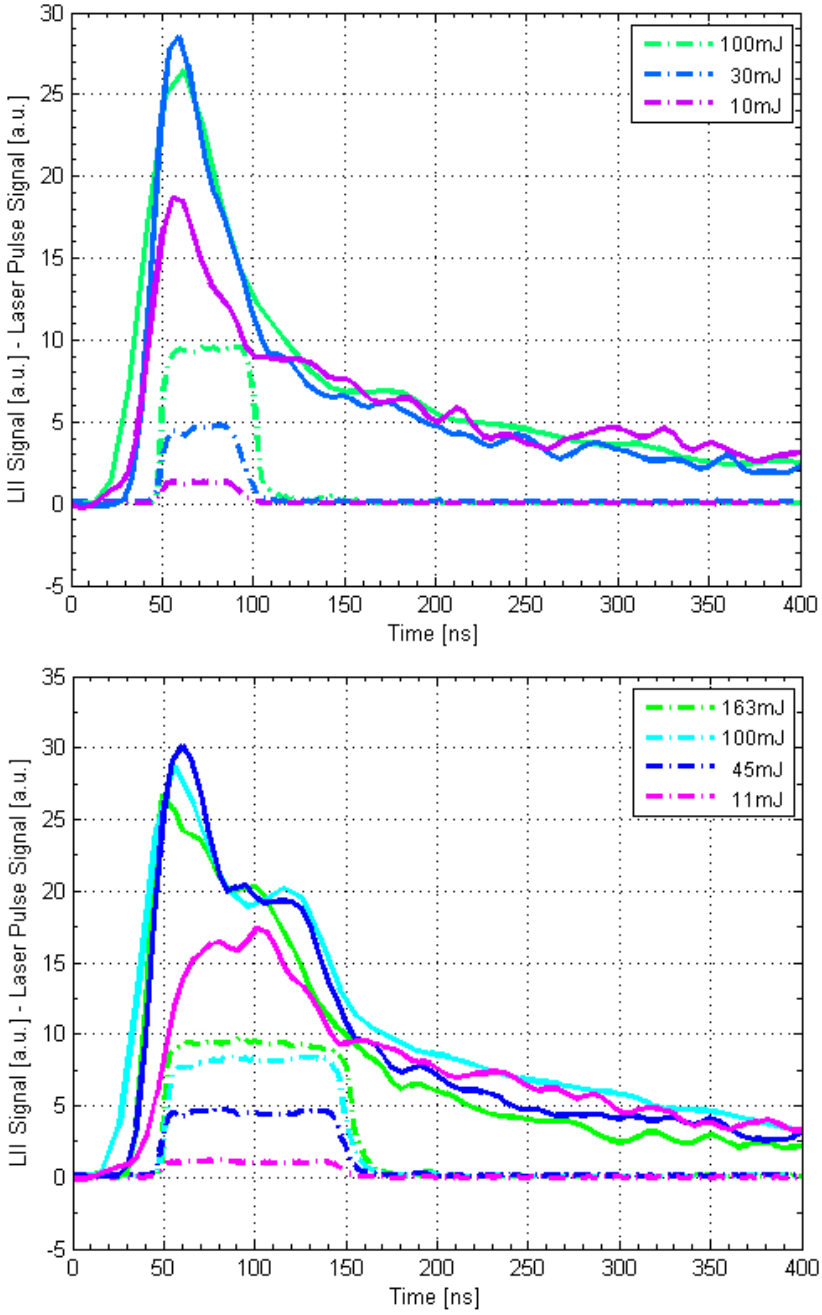

Figure 2.16: Temporal LII signal using different laser pulse energies. The original rectangular laser pulses (dashed line) are shown together with the corresponding LII signal (solid line). The top graph is for the 50 ns pulse, while the bottom is for the 100 ns pulse. (Ditaranto et al., 2013)

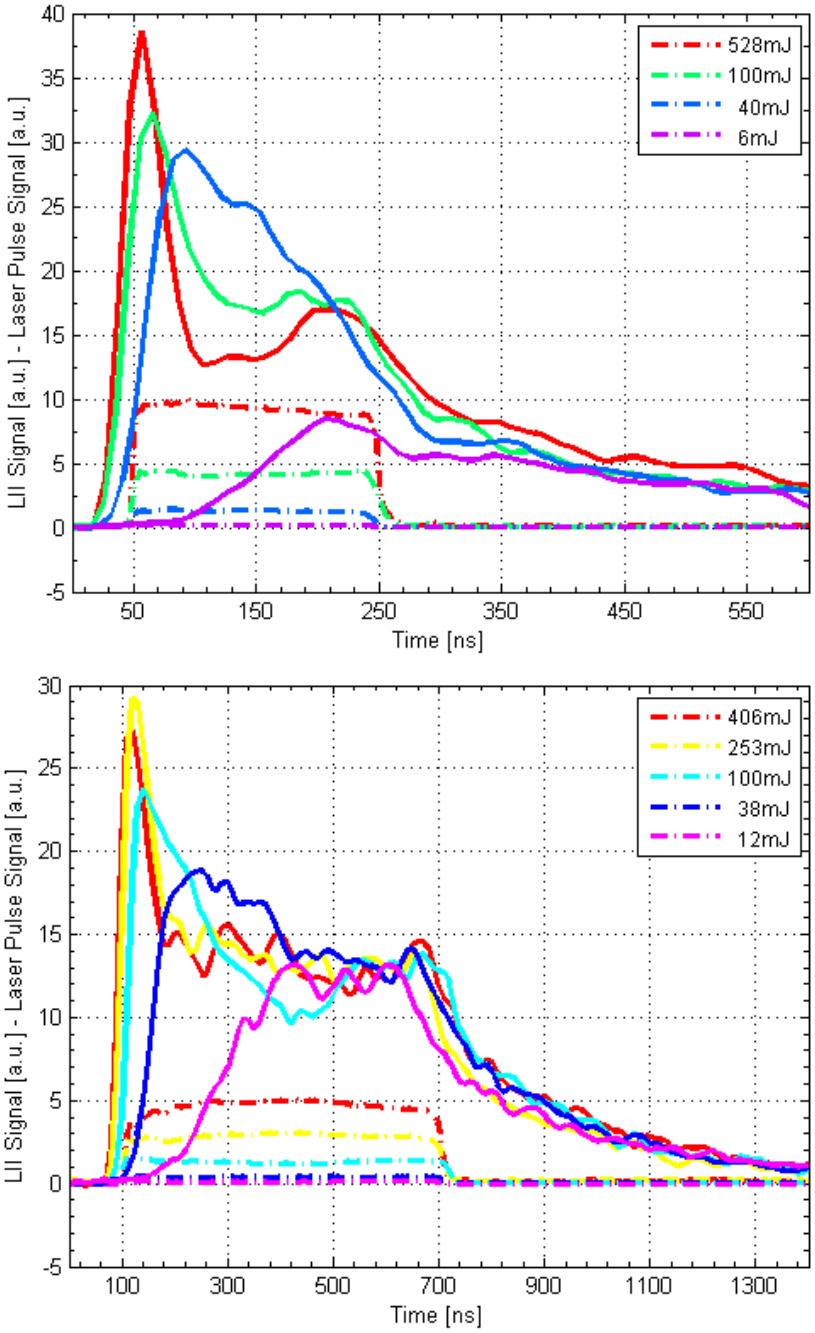

Figure 2.17: Temporal LII signal using different laser pulse energies. The original rectangular laser pulses (dashed line) are shown together with the corresponding LII signal (solid line). The top graph is for the 200 ns pulse, while the bottom is for the 600 ns pulse. (Ditaranto et al., 2013)

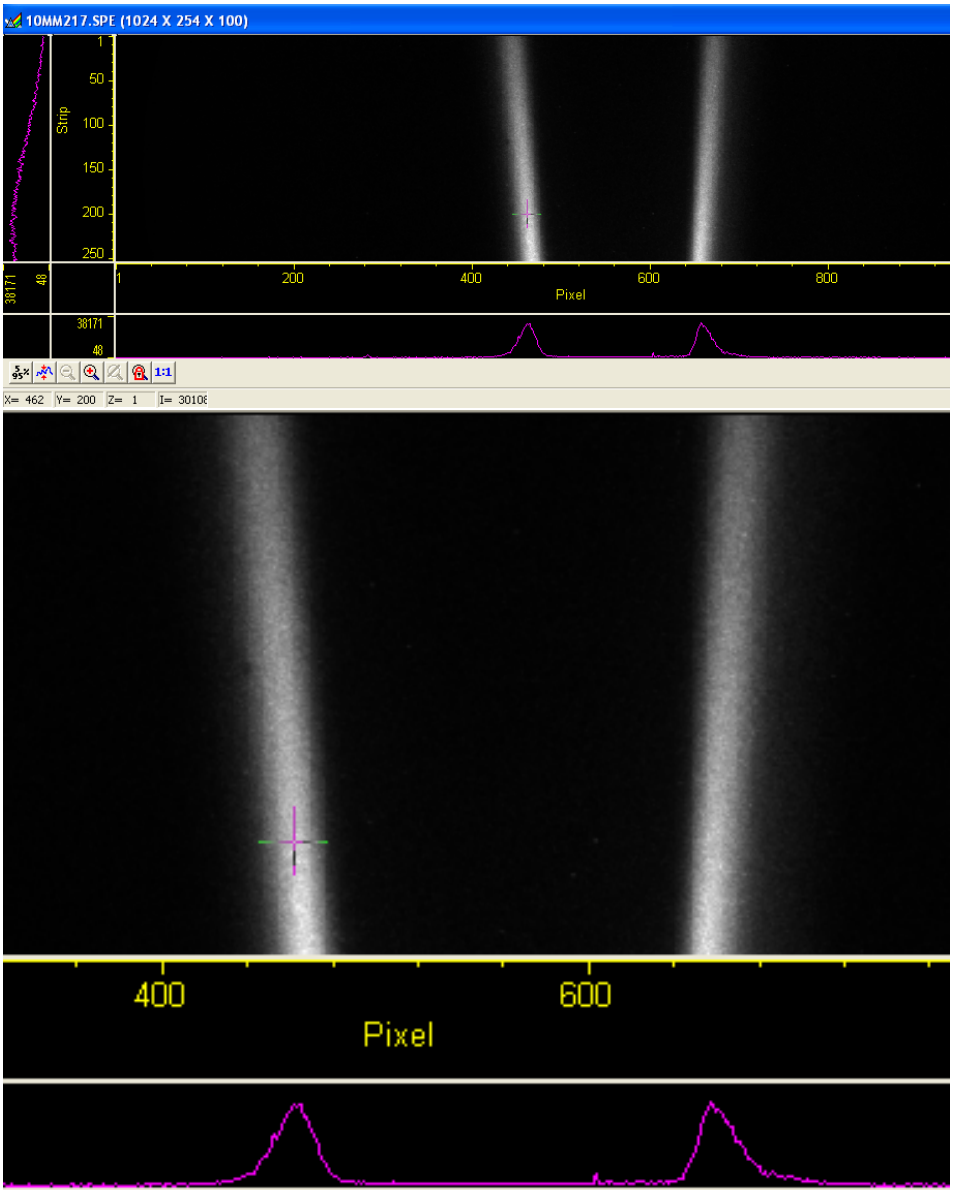

Figure 2.18: LII image of the flame. The high intensity at the edges of the flame show that this is where the soot particles are. This image is a 2D image of the flame, i.e. the cross-section seen by the ICCD camera. In the center of the flame, no intensity is registered. This image is one of the LII images obtained by C. Meraner (Ditaranto et al., 2013).

3 Experimental Setup

The VATL laboratory at NTNU/SINTEF in Trondheim, Norway is equipped with a pulsed Nd:YAG laser with temporal shaping capabilities. The main part of this project consisted of setting up a rig where LII measurements can be performed on a small laminar ethylene flame (C_2H_4(g)). The laser impacting the flame needed to have varying laser temporal pulse durations and varying pulse fluence [J/cm^2]. The Nd:YAG laser at the VATL laboratory had a maximum pulse energy of about 520 mJ for its 532 nm laser beam.

Figure 3.1 shows the experimental setup used in this project. The experimental setup is mainly composed of:

- A frequency doubling Nd:YAG Continuum Agilite 56-910 system. The laser emits at 532 nm, 10 Hz. Maximum pulse energy is about 520 mJ. Service was later performed and the frequency doubling crystal was then removed, making the laser emit 1064 nm laser light.

- Optical components such as a periscope (two reflecting mirrors), a half-wave plate, a beamsplitter, focusing lenses and a notch filter.

- Oxy-fuel combustion chamber. The chamber stands on a moving structure. Mass flow controllers regulate the coflow of fuel gas and air.

- Princeton Instruments PI-MAX intensified CCD camera. The camera is controlled using Princeton's data program WinSpec.

Due to space constraints, the laser and optical components are in one room, while the combustion chamber and ICCD camera is in another. The laser beam passes through a hole in the wall between these two rooms.

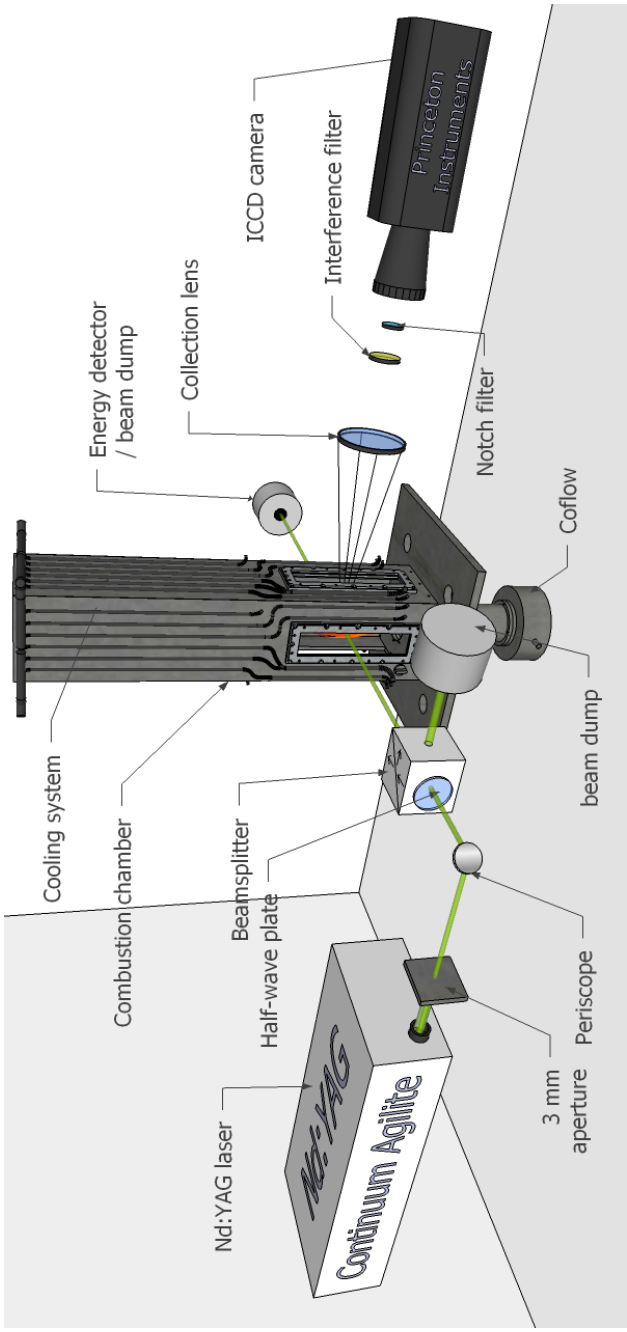

Figure 3.1: Schematic representation of the experimental setup. The 532 nm laser beam goes through various optical components before reaching the ethylene flame inside the combustion chamber. The ICCD camera registers the radiation from the soot particles. Figure is tilted for better visibility. Modification of a figure from the doctoral thesis by A. Sevault(Sevault, 2012).

3.1 Ethylene Flame

The soot particles are generated in a small and very sooty laminar ethylene flame. The ethylene flame develops above a 5 mm diameter circular nozzle and issues at 21 cm/s. Around this nozzle is a 10 mm diameter coaxial tube which for this experiment was not used, see Figure 3.2. Enclosing these two tubes is a 97 mm diameter circular tube supplying air to the flame and also stabilizing it. The laser beam impacts the flame 1.9 mm above the nozzle exit.

Figure 3.2: The nozzles where ethylene gas and air exits. The inner tube of exiting fuel gas has a 5 mm diameter and around this is an empty 10 mm diameter tube. Around these two nozzles is a 97 mm diameter circular tube of hexagonal array (honeycomb) where the airstream exits.

The fuel is controlled by a mass flow controller with optimal range 0-2 L/min in normal conditions, i.e. temperature T = 0 °C and pressure p $= 1$ atm. The ideal gas law was used to find the mass flow rate per density to set for both the fuel and air supply. Mass flow rate $\dot{Q}$ of the ethylene gas is given by:

$$\dot{Q} \;=\; \rho \cdot u \cdot A \tag{3.1}$$

where ρ is the density of ethylene, equal to $\rho = 1.178 \cdot 10^{-6}$ kg/cm^3 in room temperature. The output velocity u is 21 cm/s. The cross-sectional area A is $\pi \cdot 0.25^2$ cm^2 for the fuel nozzle. These values give $\dot{Q} = 4.86 \cdot 10^{-6}$ kg/s. The mass flow rate $\dot{Q}$ is constant through the transition from normal conditions to room temperature conditions.

From the ideal gas law, we get the relationship between room temperature conditions and normal conditions at constant pressure:

$$\rho_{room} \cdot T_{room} = \rho_n \cdot T_n \tag{3.2}$$

Here $T_n = 273.15$ K and T_r is around 288.15 K (15 °C). Insertion of these temperatures and the known density of ethylene gas in room temperature, equation (3.2) gives the density of ethylene in normal conditions as 1.243 kg/m^3.

The corresponding mass flow rate per density of ethylene in normal conditions is then

$$\left(\frac{\dot{Q}}{\rho}\right)_n = \frac{4.86 \cdot 10^{-6}\ kg/s}{1.243\ kg/m^3} = 0.234\ Ln/min \tag{3.3}$$

The mass flow controller is therefore set to 0.23 Ln/min, resulting in a small and stable ethylene flame.

Figure 3.1 shows the combustion chamber with the coflow entrance from below. The chamber is fully ventilated from above. In order for the ethylene gas to be released into the air, there are several safety devices installed. First, the ventilation system must be on and the mass flow controller set to correct value. Also, only when a flame detector sees a flame within the chamber, will the ethylene gas be released. It is therefore necessary to have an ”ignition flame” the detector can detect. A handheld propane torch is used for this purpose.

From the ethylene gas container to the combustion chamber, there are three safety switches or gas regulators. The ventilation system is essential to this experiment even for a relatively small flame. This is because we can have gas build-up within the pipe. Even though the mass-flow controller is set to a certain value, all of the built-up gas will be released when the flame detector sees the ”ignition flame”. The expected small flame will then turn out to be quite large, and it is therefore crucial that this flame is quickly ventilated upwards and away from the operator. The large flame itself is relatively harmless since the fuel gas is quickly burned. However, the operator must always be prepared for the possibility of a larger flame than expected.

Stability of the ethylene flame is greatly helped along by the airstream surrounding the flame. The airstream is set to exit at a much greater velocity and it shields the flame from outer disturbances, such as the ventilation system in the room. It also encases the flame in such a way that the flame interacts less with stationary air particles. The airstream creates a stable flame of cylindrical shape. The resulting flame is a little higher than what it is without the airstream present.

3.2 ICCD Camera

The radiation from the laser heated soot particles are detected by an intensified CCD camera (PI-MAX, Princeton Instruments). The experimental setup depicted in Figure 3.1 shows the camera's position with regard to the flame and the laser beam path.

3.2.1 Finding the Camera's Focus Point

In order to see where the camera had its focus, a sheet of paper with small numbers and letters was placed directly over the center of the fuel nozzle without coming into contact with it. A lamp was directed at the paper so that the reflections would be detected by the camera. The 2D image from the camera then showed the position of the camera's focus, see Figure 3.3.

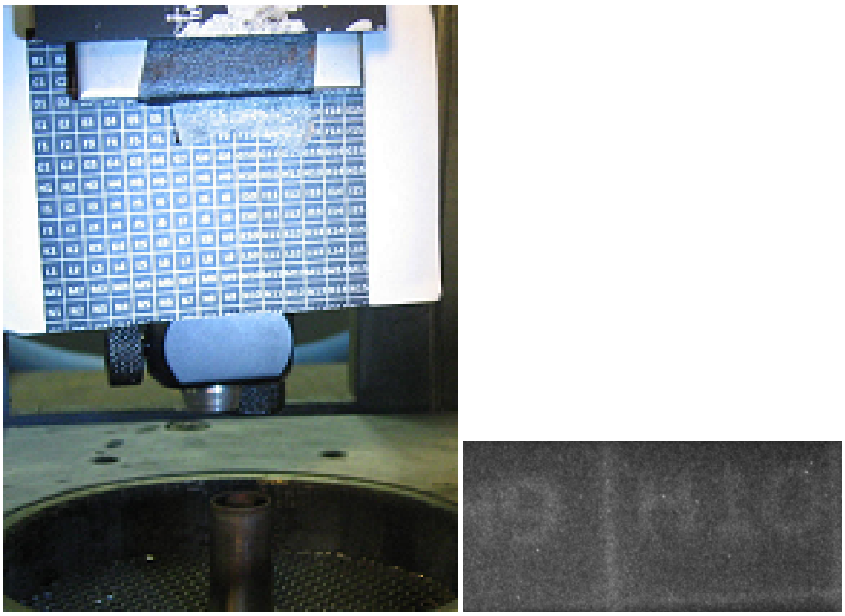

Figure 3.3: Finding the focus position of the camera using a paper with small text on it. The paper is placed directly over the center of fuel nozzle. A lamp shines light on the paper and the ICCD camera detects the reflections. The small image to the right is the image from the camera, in this case showing the text "H9 / H10".

When first trying out the camera for LII testing, one must start with low laser energy and minimum signal gain. The energy can then slowly be increased, all the while making sure there is no possibility of saturating the camera's pixels.

3.2.2 Resolution of the Images

As Figure 3.4 shows, 140 pixels represents a measured true width of 4 mm. One pixel in the collected image thus represents approximately 28.6 μm in true size. A part of the sheet of paper with numbers and letters is shown next to the black-and-white image taken by the ICCD camera.

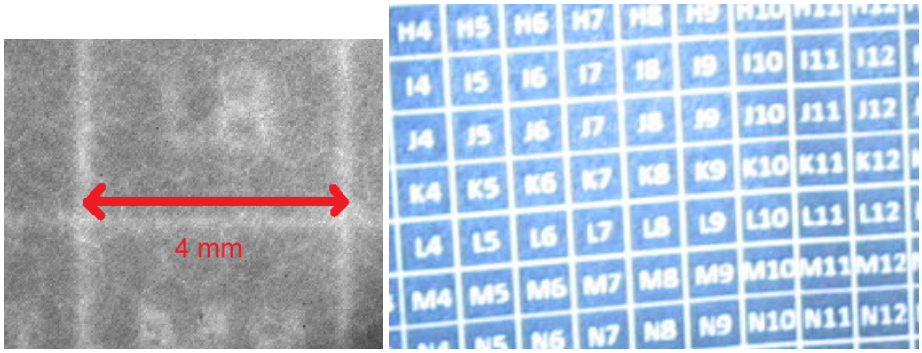

Figure 3.4: The left image is part of the 2D intensity image captured by the camera. The red line is 140 pixels wide, and measured to be 4 mm in true width. The image to the right is part of the sheet of paper shown in Figure 3.3.

The true resolution of the ICCD camera's pixel is 26 μm. The magnification caused by the setup is thus found to be approximately

$$M = \frac{28.6\mu m}{26.0\mu m} = 1.1 \tag{3.4}$$

The focal length f of the collection lens is 249 mm. Figures 3.3 and 3.4 show how the alignment of the camera was found by evaluating the overall sharpness of the image using eyesight. The image did not suddenly come in to focus, it was more an approximate ideal camera position that was finally decided upon. Ideally, both the flame and the camera would have been exactly 2f = 249 mm x 2 away from the collection lens, giving perfect imaging. In this setup a magnification of 1.1 signifies that $M = \frac{d_i}{d_o} = 1.1$, where d_i is the distance between the lens and the camera and d_o is the distance between the lens and the sheet of paper in Figure 3.4.

3.2.3 Depth of Field of Camera

The depth of field or DOF is the length around the focus point of the lens that is sharply collected by the camera, see Figure 3.5.

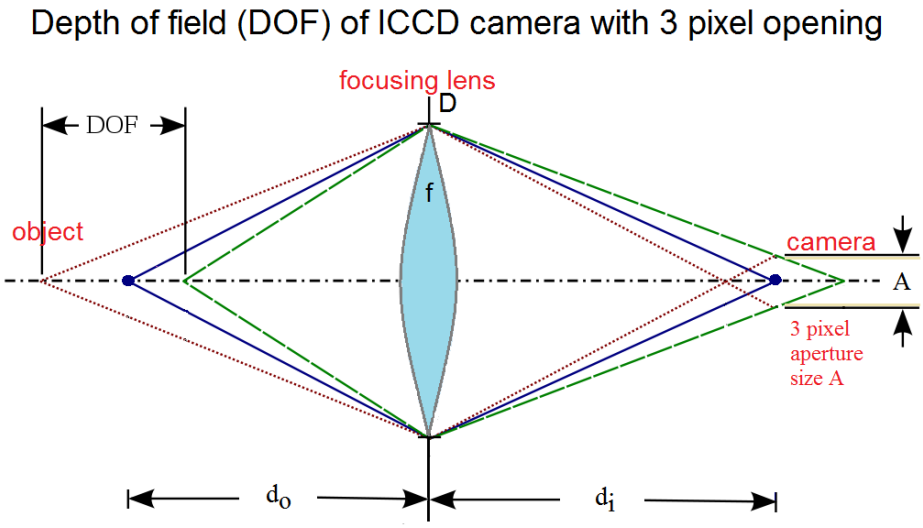

Figure 3.5: Sketch of the depth of field of the camera with 3 pixels as aperture size. The calculated DOF-value is 0.39 mm. Within this distance all light is collected and stored by the three pixels.

The depth of field of the ICCD camera is dependent on the camera's aperture size and the collection lens used. Equation (3.5) calculates the camera's DOF or the spatial resolution of the system (Eckbreth, 1996). It is dependent on the focal number $f_\#$ of the collection lens. The focal number $f_\#$ is the focal length of the lens divided by its diameter D. Perfect focus of the lens lies a distance 2f from the lens, and the depth of field of view is thus given by

$$DOF = 2f_\# A = 2\frac{f}{D}A \tag{3.5}$$

In these experiments, the LII signal is found by averaging a pixel with its eight closest neighbors. With this in mind, the aperture diameter of one measurement point in the CCD field is three pixels in height, or in other words A = 3 x 26.0 μm = 78 μm. Inserting values into equation (3.5) gives

$$DOF = 2 \cdot \frac{249mm}{100mm} \cdot 78\mu m = 0.39mm \tag{3.6}$$

3.3 Agilite 569-10 Laser System

The whole optical setup of the Agilite system resides on a 110mm thick optical breadboard and is covered with an enclosure attached to the breadboard. The enclosure has an output port for the laser beam to exit. The laser system's power control unit contains two cooling groups, two power distributions, three dual PFN power supplies, a programmable laser pulse shaper, timing control unit and a CW seed laser power supply. Detailed information about the Agilite 569-10 Laser System is found in the system reports (ContinuumCorporation, 2008) and (ContinuumCorporation, 2005-2008), only the main aspects are presented here.

As Figure 3.6 depicts, the optical system starts with the CW seed laser emitting approximately 500 mW CW radiation at 1064 nm. The CW radiation is then sliced and shaped into appropriate seed pulses by an electro-optical modulator. The seed pulses are then amplified in three amplification stages. First, the beam passes through a pair of 5 mm rod single lamp heads, then a pair of 6 mm rod single lamp heads and finally a pair of 9 mm rod dual lamp heads.

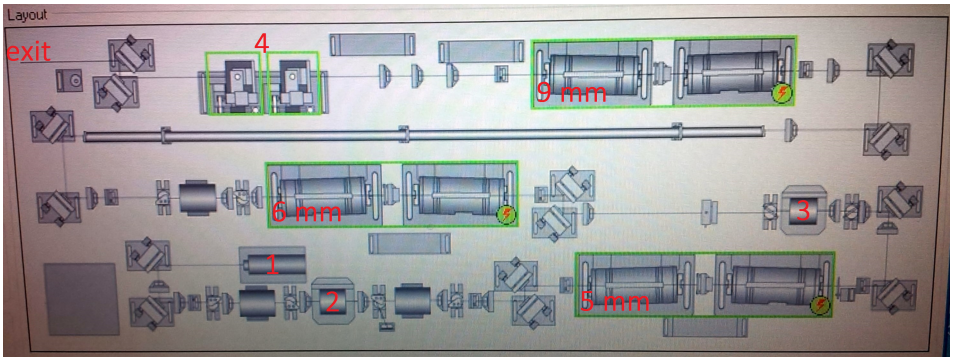

Figure 3.6: The inside of the Agilite Laser System. 1) CW seed laser emitting 1064 nm light at 500mW. 2) Electro-optical modulator. 3) Additional double Pockels cell with appropriate driver. 4) Second-harmonic generator consisting of two KTP doubling crystals. The position of three amplification stages are also shown in the figure, depicted by the length of the rod of the lamp heads used and also by the small lighting bolt symbol and surrounding green box. The system starts with the CW seed laser, the laser beam then follows the path depicted through the optical system before it is finally directed out of the output port (depicted by the text "exit").

The additional double Pockels cell has been employed between the first two amplification stages to further suppress the CW radiation from leaking through the pulse shaping electro-optical modulator. A Pockels cell is an electro-optical device, like the electro-optical modulator. It is basically a voltage-controlled wave plate. It consists of an electro-optic crystal through which the laser beam passes. The polarization direction of the laser

light is controlled by the voltage applied to the crystal. An electro-optical device can thus be used to rotate the polarization of the beam passing through it. By varying between ”open”, ”degree of openness” and ”closed” in terms of allowed polarization, the device can be used to create temporal pulse shapes [1].

The CW seed laser creates a laser beam of 1064 nm wavelength. It is only right before the exit of the ”laser box” that the frequency is doubled by the KTP doubling crystals, each 20 mm long. The infrared input beam generates another wave of twice the optical frequency during its path through the nonlinear crystal. The process is called second-harmonic generation. The residual infrared light is caught by a water cooled beam dump after its exit from the crystal, while the green light is directed out of the laser.

The generated second-harmonic green light has lower intensity than the original infrared light. For low incoming intensity, the conversion efficiency to green light is small and increases linearly. The intensity of the frequency doubled wave grows at this stage with the square of the incoming beam's intensity. For high intensities, the efficiency doesn't increase as much, and the output intensity will of course always be less than the incoming.

In order to have the output laser beam in the infrared spectrum, one need only remove the frequency doubling crystal. The crystal was therefore simply removed for the 1064 nm LII measurements and two new mirrors were added to direct the infrared 1064 nm light towards the laser's exit.

As the frequency doubling crystal had to be removed, general service was also done on the laser. Realignment of all components inside the laser was performed. There are irises at many positions inside the laser. Using a beam viewer, the alignments were checked and improved. It is very important for example, that the laser beam is well centered when it passes through an amplifier. This was ensured by checking the irises set up before and after the amplifier, and mirrors were slightly adjusted if needed. It is also very important that the crystal axis of the electro-optical modulator is aligned with the ray axis. Misalignment can for example lead to a large phase shift or an unwanted polarization rotation.

The system specifications from 2008 reports the laser beam to have a 70% Gaussian fit in the near field (< 1 m), and a 95% fit in the far field. The beam divergence is reported to be 5 mrad and the repetition rate is 10 Hz (ContinuumCorporation, 2008).

[1] See (ContinuumCorporation, 2005-2008) for further details

3.4 Spatial Laser Beam Profile

Several measurements of the spatial beam profile were taken before and after the service on the laser, and also at different positions. The spatial intensity images presented here were taken after being attenuated by two wedges. The images were taken either very close to the laser output port or at the position of the nozzle exit, about 3 m away from the output port. For both the 532 nm and the 1064 nm beam, the spatial profiles with and without the 3 mm aperture were recorded.

3.4.1 $1/e^2$-width

In the following figures of the spatial beam profiles, several parameters of the laser beam can be found. For the Gaussian beamwidth or the $1/e^2$-width, the "$2W_{ua}$"-parameter is to be read. For example, in Figure 3.12, the average laser beamwidth for the 1064 nm pulse in the top image is (2.030 mm + 1.964 mm)/2 = 1.997 mm, and thus less than the 3 mm width expected as a result of the beam passing through a 3 mm aperture. The bottom image gives an average beamwidth as (2.028 mm + 1.986 mm)/2 = 2.007 mm. The beamwidth is thus found to be approximately 2.0 mm, and this is the beam size used in further calculations for the 1064 nm pulse.

3.4.2 532 nm Laser Beam

Before any service was done on the laser, the spatial laser beam profile was checked at the nozzle's position. The spatial profile was first checked with the 3 mm aperture and the periscope as the only components before the nozzle. As the results show, see Figure 3.7, the laser beam has been affected by diffraction caused by the aperture. Since the aperture was placed quite a long distance away from the nozzle exit, its diffraction fringes are increased at the nozzle's position. The beam also has a prominent center peak. As the LII is dependent on fluence, this beam profile is not the rectangular shape ideally wanted and neither is it very close to a Gaussian distribution.

532 nm - With 3 mm Aperture at Flame Distance

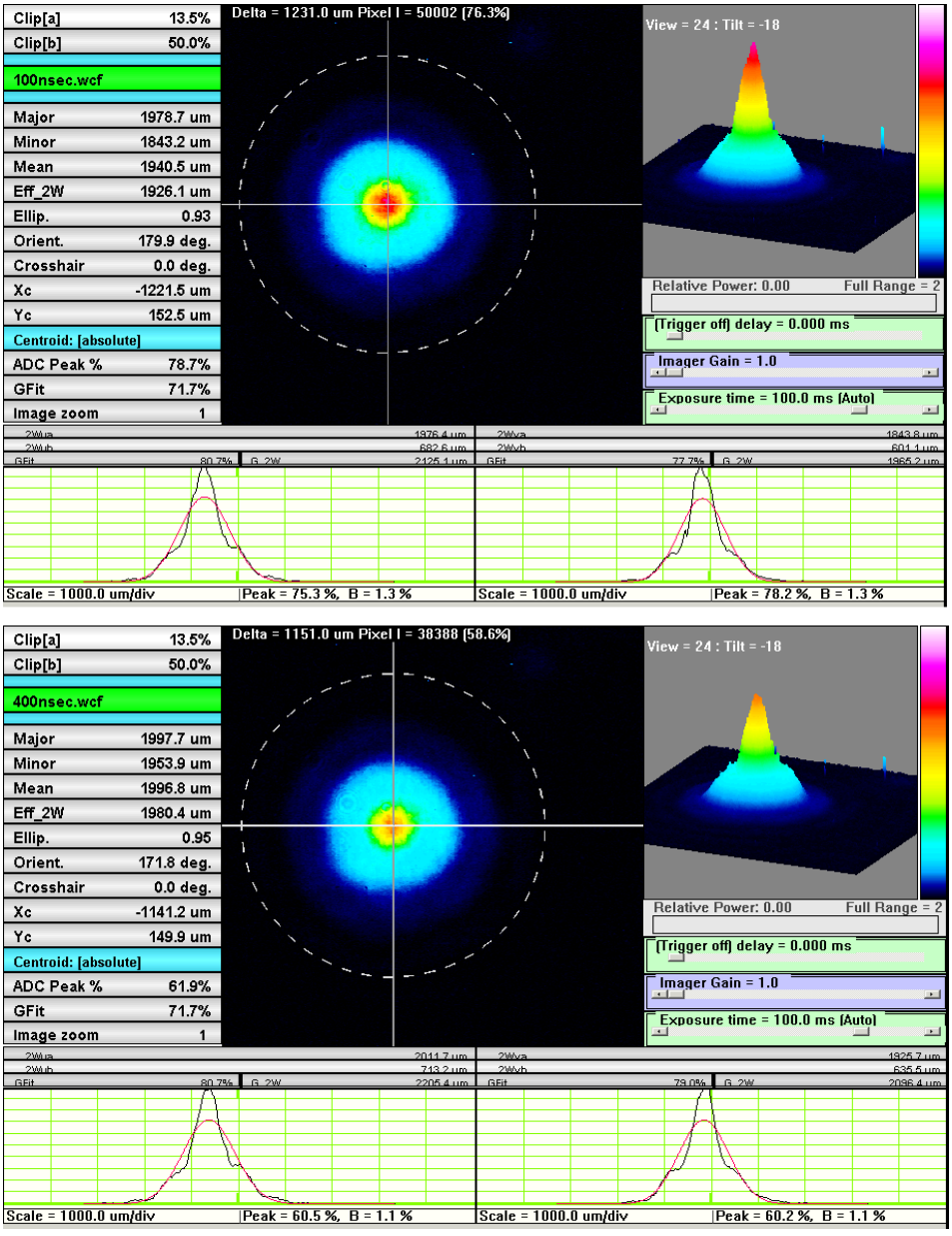

Figure 3.7: Spatial beam profile of the 100 ns and 400 ns pulse at the position of the nozzle exit. The measured averaged $1/e^2$-widths were 1.91 and 1.96 mm.

532 nm - Without Aperture at Flame Distance

For comparison, the aperture was removed and the spatial profile was again checked. Figure 3.8 shows the results, a Gaussian beam profile about 4.5 mm in diameter.

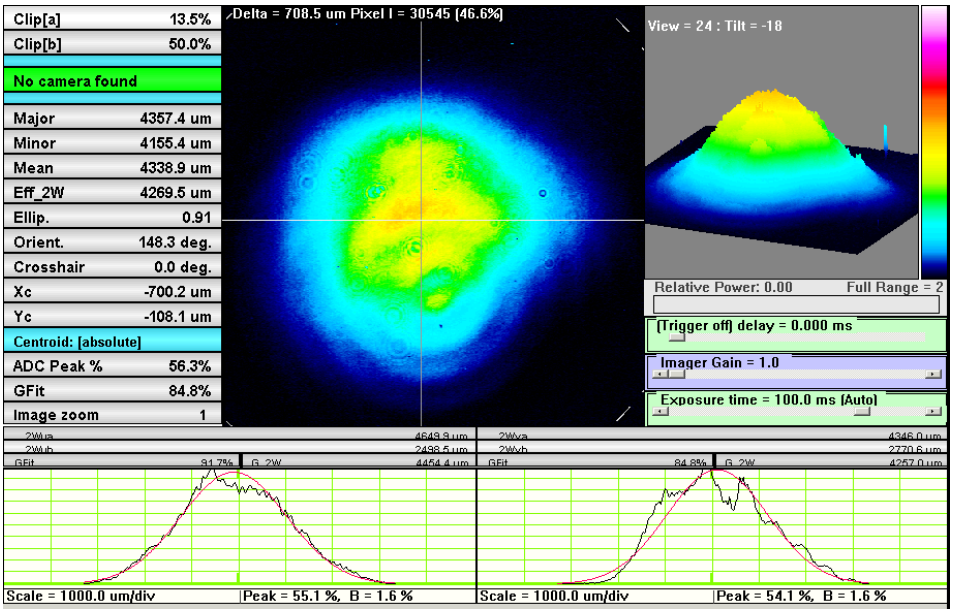

Figure 3.8: Spatial beam profile of the 532 nm beam at the position of the nozzle exit, but now without the aperture in place. The average measured $1/e^2$-width was 4.50 mm.

3.4.3 1064 nm Laser Beam

After the wavelength of the laser light had been changed, the new spatial beam profile of the laser was recorded. Figure 3.9 show the spatial beam profile for the laser beam at different energies. The shape of the beam changes only slightly with increasing energy.

The spatial profile of the 1064 nm laser beam was studied both near the laser's output port and at the position of the nozzle exit. As with the 532 nm beam, the beam with and without the 3 mm aperture was measured. Another test using a 4 mm aperture was also done for comparison with the 3 mm aperture, see appendix 6.1. In the LII experiments, the 3 mm aperture was used.

1064 nm - Without Aperture, Near Laser Output Port

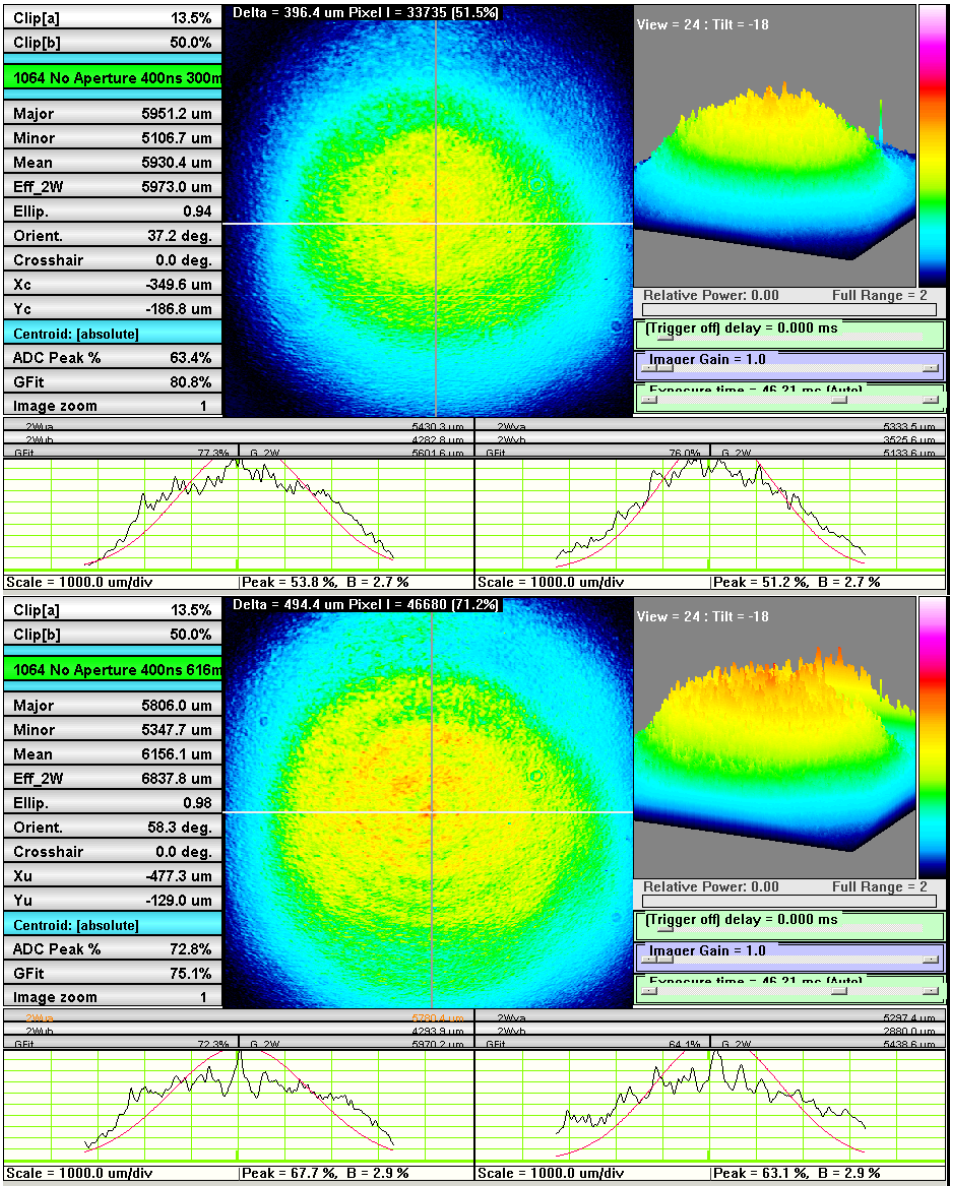

Figure 3.9: Spatial beam profile of the 1064 nm laser beam without the 3 mm aperture in place. The pulse duration was 400 ns and the energy about 300 mJ and 600 mJ. The average measured $1/e^2$-widths were 5.38 and 5.53 mm near the laser output port.

1064 nm - With 3 mm Aperture, Near Laser Output Port

Figure 3.10 shows the spatial beam profile with the 3 mm aperture in place. With this high energy, the increased effect of the diffraction fringes is especially visible and the intensity profile does not have a Gaussian distribution directly after the aperture.

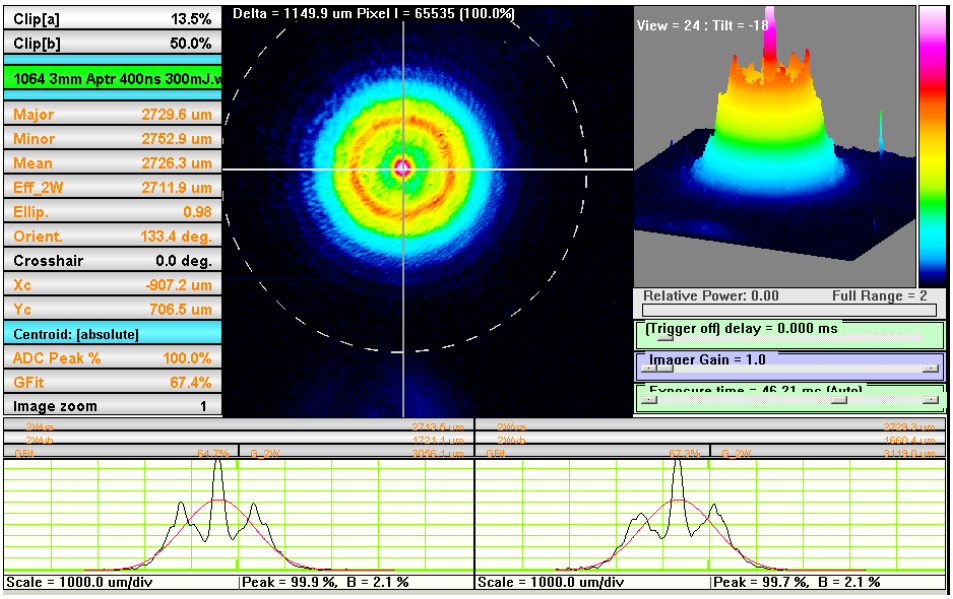

Figure 3.10: Spatial beam profile of the 1064 nm laser beam with the 3 mm aperture in place. The pulse duration was 400 ns and the energy about 300 mJ. The spatial intensity profile does not have a Gaussian distribution. Measured near laser output port, directly after the aperture.

1064 nm - Without Aperture at Flame Distance

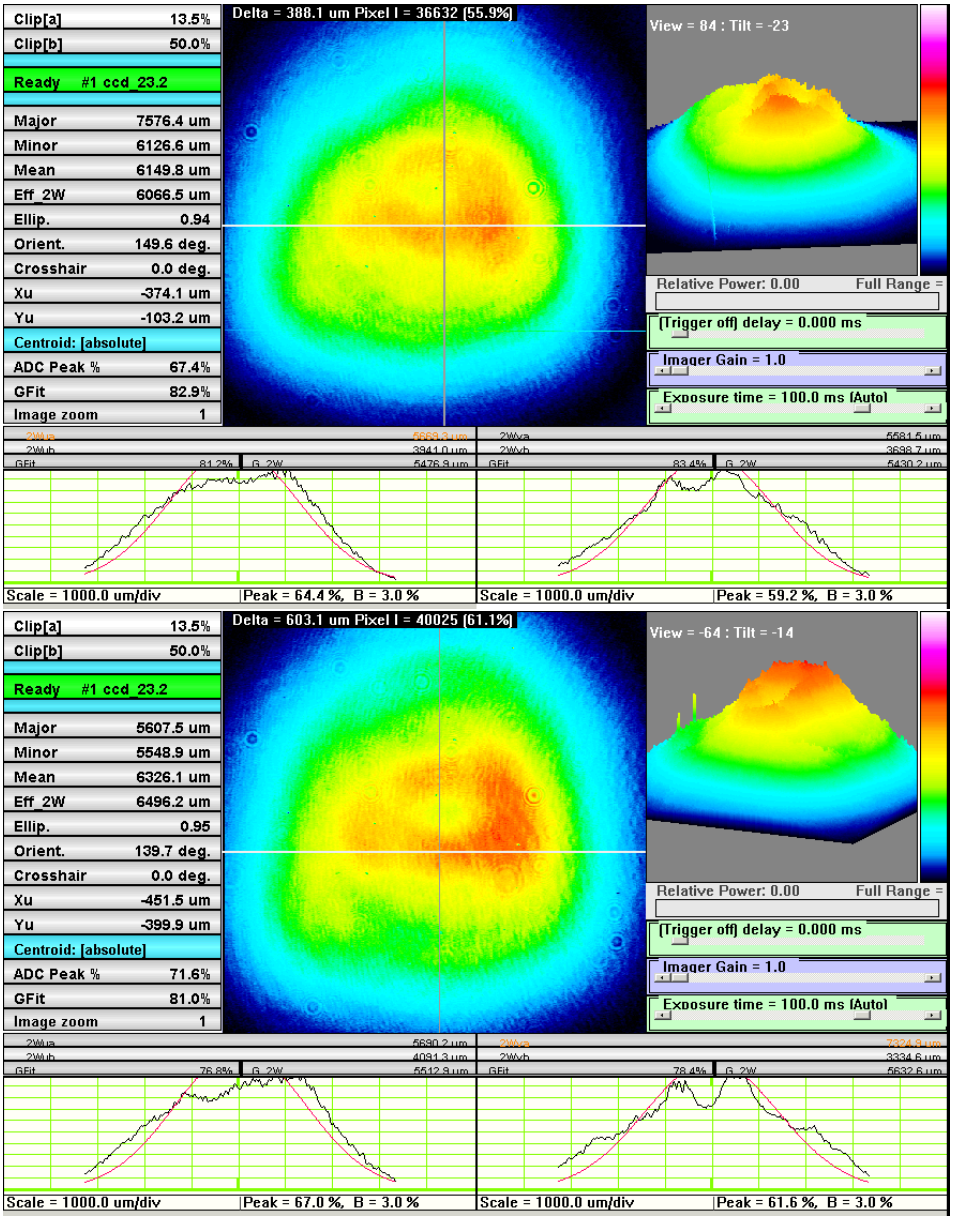

Figure 3.11: Spatial beam profile of the 1064 nm laser beam without an aperture in place. The pulse duration was 100 ns and the energy about 300 mJ and 500 mJ. Studying the top image, the average measured $1/e^2$-width is 5.63 mm. The images were taken at flame distance from the laser output port.

1064 nm - With 3 mm Aperture at Flame Distance

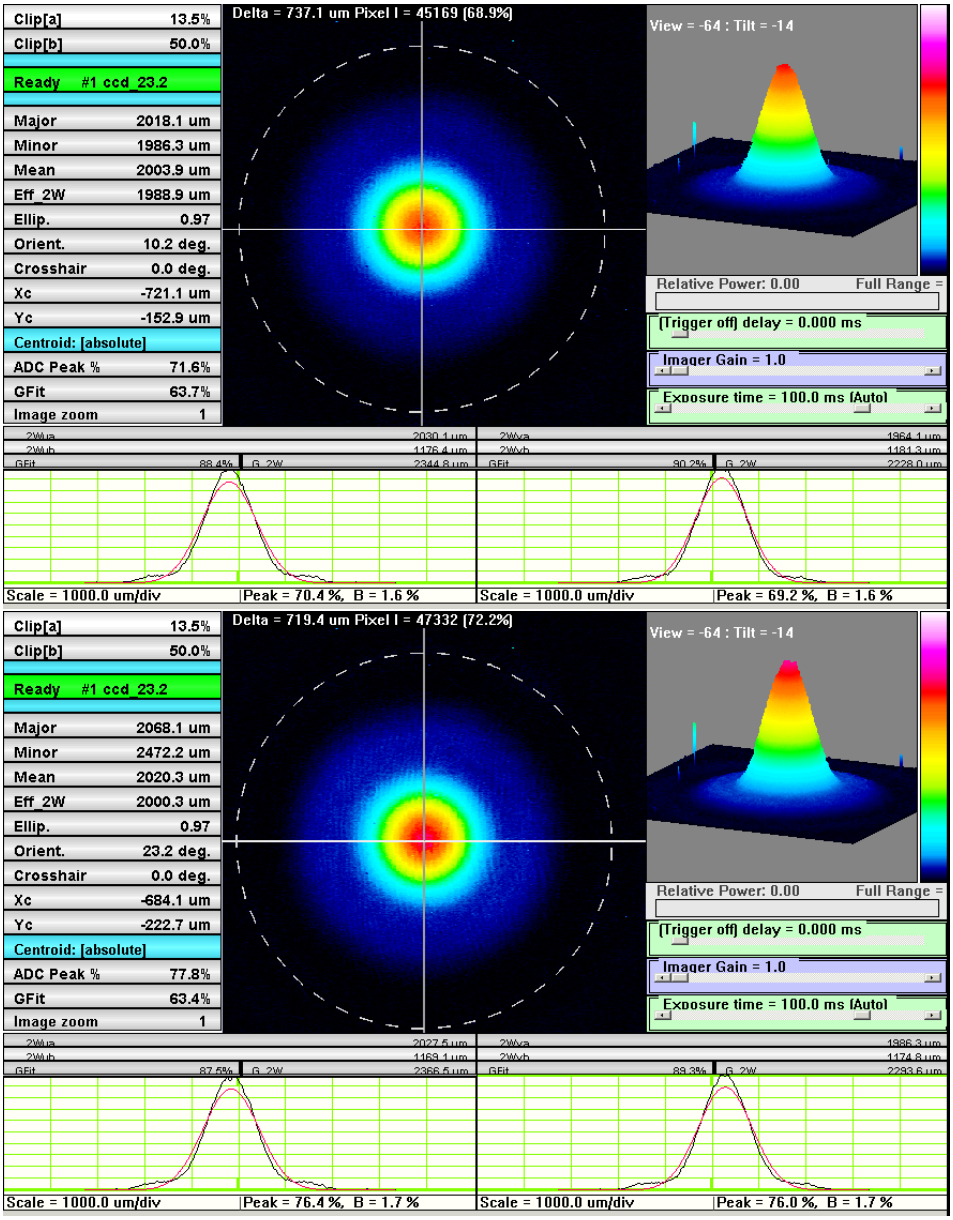

Figure 3.12: Spatial beam profile of the 1064 nm laser beam with 3 mm aperture in place. The pulse duration was 100 ns and the energy about 105 mJ and 187 mJ. The average measured $1/e^2$-width was 2.0 mm at flame distance from the laser output port. The intensity distribution is clearly Gaussian, though the fitted Gaussian curve in red has a slightly lower peak value.

3.5 Optical Setup

3.5.1 Possible LII Testing Scenarios

There are several ways the laser beam can impact the ethylene flame. One way is to spread the laser beam out as a vertical sheet. This can be done by inserting a focusing lens followed by a cylindrical lens. The cylindrical lens spreads the focused laser beam out in only one direction. This is a commonly used technique. It is also the technique used in the previous experiment at SINTEF (Ditaranto et al., 2013). Figure 3.13 is a schematic diagram of this measurement technique.

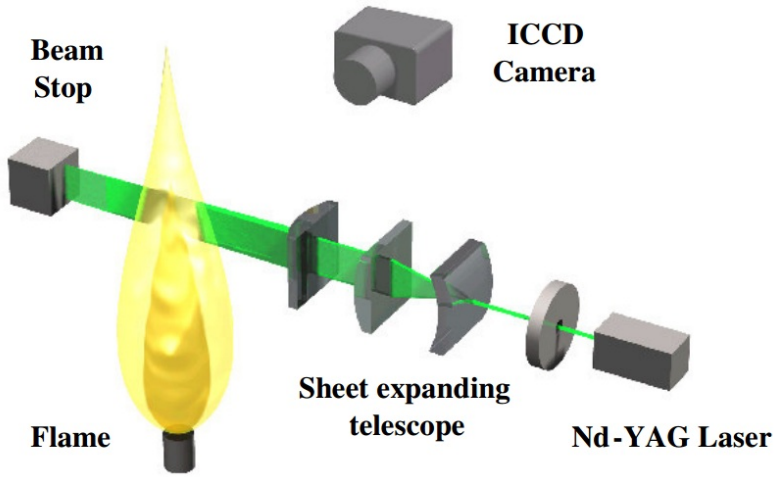

Figure 3.13: Typical setup when expanding the laser beam in one direction in order to cut the flame with a ”laser sheet”. Figure from (Qamar et al., 2005).

Using a laser sheet ensures that soot is impacted with laser light in a very small area. A problem with this technique is that soot particles outside the area of interest are also impacted by laser light. The camera may detect some of the incandescence from these outside particles as well. In the previous experiments there were some problems with the laser beam's spatial intensity profile. Measurements revealed that the beam's intensity varied greatly in the y-direction. It was therefore not possible to know if the measured average energy of the laser pulse was a good indication of the true energy impacting the flame in the camera's ROI.

The technique used in this project was to simply let the 3 mm laser beam continue undisturbed towards the flame. When using this technique, it is important to be careful of not impacting the soot particles with too high fluence. Implementation of a variable attenuator or beamsplitter makes it possible to vary the fluence of a laser beam. The experimental setup design is shown in Figure 3.1.

With a small beam size, the ICCD camera will detect the LII signal from the soot particles within a known cross-sectional area. The advantage of the technique shown in Figure 3.1 is that it gives more control over the energy fluence and the spatial laser beam profile.

The optical setup for the 532 nm and 1064 nm laser light differ slightly and will be introduced separately. The slightly different design for the 1064 nm light was designed to improve the spatial intensity profile of the laser beam, seen in section 3.4.

3.5.2 Alignment of an Optical Component

When including new optical components to an experimental setup, the unwanted reflections must be found and contained. Heat-resistant aluminum foil is used to catch the unwanted reflections from each component. As the fluence is quite high, it is especially crucial to make sure that the reflected beam cannot return to the laser's output port and cause damage to the laser. In order to separate a reflected beam from an incident beam, the optical component is tilted slightly away from the direct path of the beam. The reflected beam from the variable attenuator will thus be a small angle away from the incident beam, and an aluminum foil can then catch this reflection safely.

Unfortunately, while catching the unwanted reflections, this method also tilts the outgoing beam a corresponding small angle away from the initial laser path. The optical components must therefore be carefully aligned and tilted with respect to each other so that the final outgoing laser beam crosses the fuel nozzle at its center. The reflections were found using very low laser energy, a small white paper and eye sight. For the 1064 nm tests, a beam viewer was used to see the laser light.

When adding an optical component, perfect alignment and centering of the new component is very important. Small changes in the position of it will have a great impact when the laser beam only has a small beam size and a large energy. As an example, the 3 mm aperture had to be as perfectly centered as possible in order for the resulting beam to have the wanted beam profile. To align the aperture, eye sight at very low energy was first used to find a good starting position. For further centering, the 3 mm aperture was connected to the table in such a way that small adjustments could be made in both horizontal and vertical direction with 0.01 mm accuracy.

3.5.3 Variable Attenuator/Beamsplitter

As Figure 3.15 shows, a periscope had been mounted in order to change the direction and height of the laser beam. This was necessary for the laser beam to enter the room containing the combustion chamber. The periscope was made up of two reflecting mirrors.

After the mirrors, the laser beam reaches a half-wave plate and a beamsplitter (attenuator). This combination will ideally make it possible to vary the outgoing energy from 0% to 100% of the incoming laser beam energy. How the optics of this works will here be further explained. The percentage of energy that is not allowed through the beamsplitter is directed towards a beam stopper or "beam dump".

Wave plates and linear polarizers are optical components that can alter the polarization of light passing through them. A half-wave plate rotates the plane of polarization from a polarized laser to any other desired plane. The 532 nm laser beam in this experiment was originally vertically polarized. Introducing a half-wave plate to the optical setup made it possible to shift this polarization direction.

An electromagnetic wave propagating in the z-direction can be represented mathematically by a Jones vector. When light goes through an optical component, the resulting polarization of the emerging light can be found by taking the product of the Jones matrix of the optical component and the Jones vector of the incident polarized light. As described in section 2.2.4, the optical system' transfer matrix can be found by multiplying all the components' Jones matrices. The Jones matrix representing a half-wave plate is

$$J_{\lambda/2} = \begin{pmatrix} cos(2\theta) & sin(2\theta) \\ sin(2\theta) & -cos(2\theta) \end{pmatrix}$$

where θ is the orientation of the fast axis with respect to the horizontal axis. After passing through the half-wave plate, the original wave field has been rotated an angle 2θ.

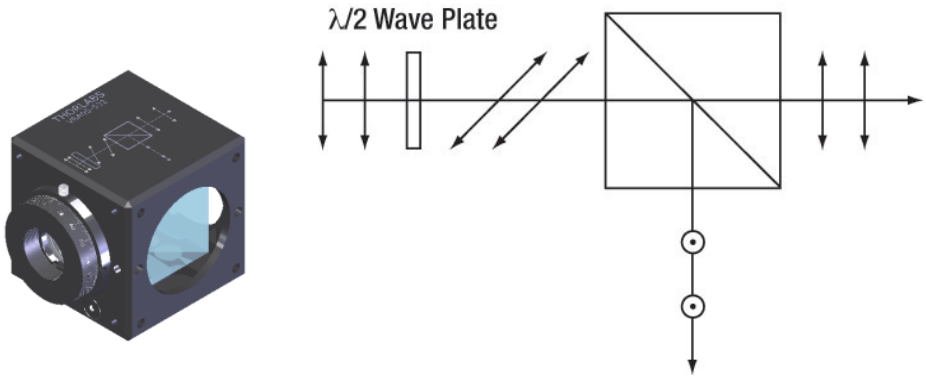

Figure 3.14: Schematic diagram of the variable attenuator's effect on an incoming laser beam. First, the incoming beam passes through a half-wave plate, an optical device that alters the polarization state of the light traveling through it. By choosing a certain angle θ for polarization, the half-wave plate polarizes the beam a certain degree, depicted in the figure by the tilted vectors. The beam then enters the attenuator or polarizing beamsplitter, which only allows a certain polarization to pass through. The outgoing beam is now a fraction of its original energy. The rejected percentage of the original beam is directed towards a beam stopper or beam dump. Both figures are from the manufacturer, Thorlabs Inc.

The half-wave plate in this setup can have its angle θ be in the range 0° to 360°. However, we are only interested in the absolute value of the energy of the emerging light. It is therefore only a 0°-90° angle range that is of interest. Figure 3.14 shows a schematic diagram of the variable attenuator's effect on an incoming beam and a picture of the cube beamsplitter itself.

Unfortunately, the variable beamsplitter for the 532 nm laser light seen in Figure 3.14 was damaged. The laser beam managed to make a small burn inside the beamsplitter. A new beamsplitter for the 532 nm wavelength did not arrive in time before the laser was changed to output infrared light. For the experimental results depicted in sections 3.6 and 4.2, the half-wave plate and the damaged beamsplitter were removed from the optical setup altogether. Temporal LII measurements with varying laser pulse energy was therefore not possible to obtain for the 532 nm laser beam.

In the experiments with the infrared laser beam, a new beamsplitter and half-wave plate were installed before the 3 mm aperture, see section 3.5.5. The beamsplitter was now of a slightly different type, a so-called plate polarizer.

3.5.4 532 nm Optical Setup

Figure 3.15 shows the optical components the 532 nm laser beam passes through before reaching the flame. After exit from the laser, the beam immediately passes through a 3 mm aperture. More than half of the original energy is thereby removed. Since the aperture size is much larger than the laser beam wavelength, diffraction was assumed to have negligible effect.

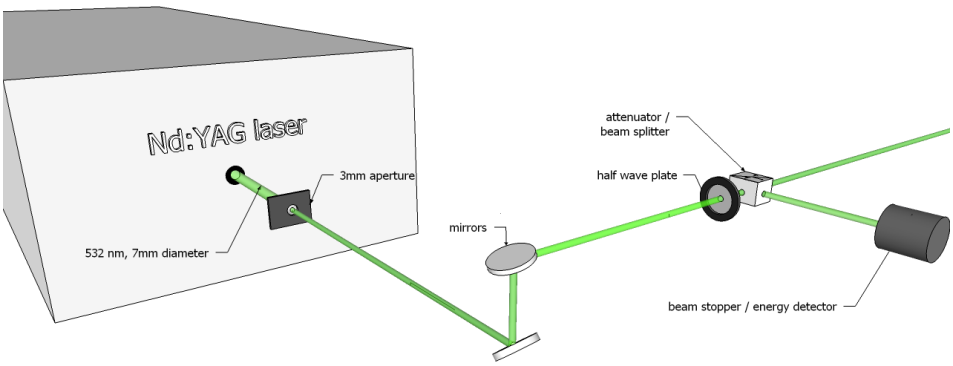

Figure 3.15: Schematic representation of the optical experimental setup for the 532 nm LII measurements.

Assumptions were made with respect to the spatial laser beam profile as a laser profiler was not possible to obtain prior to measurements. Figure 6.1 in the appendix is an image taken several years earlier of the laser beam profile. After passing through the 3 mm aperture, a 3 mm diameter laser beam of approximately constant energy was assumed since Figure 6.1 shows a fairly constant energy in this radial interval. Section 3.4 presents images of the real spatial beam profile obtained after the 532 nm LII measurements were taken. These images show a Gaussian distribution with clearly visible diffraction effects. The Gaussian fit calculates the beamwidth to be 1.94 mm instead of the 3 mm previously expected.

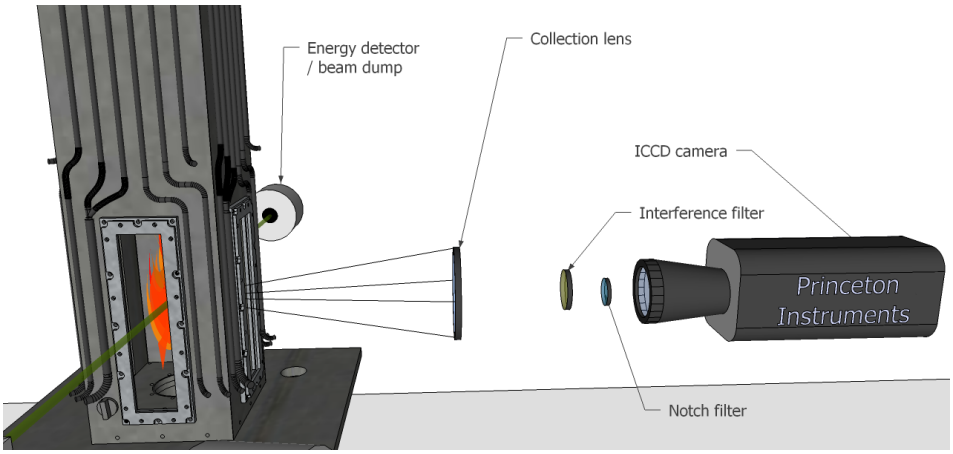

Figure 3.16: Schematic representation of the experimental setup for the ICCD camera. Between the flame and the camera are three optical components; a collection lens, an interference filter and a 532 nm notch filter.

Between the camera and the flame, there are three optical components installed, see Figure 3.1 and 3.16. First there is a collection lens used to collect as much light as possible for the camera to register. Next, there is an interference filter around 488 nm with a 10 nm wavelength gap (488FS10). LII from the soot particles will have a wavelength in this interval. The filter makes sure wavelengths outside of this interval are not allowed to pass through the lens. However, as some of the 532 nm laser light still will manage to pass through, a notch filter for 532 nm laser light was set up directly in front of the camera. This will help to ensure that as little as possible of the 532 nm light will be registered by the ICCD camera.

There had previously been registered some dependence on the angle of incidence of the notch filter. Measurements were therefore done with the notch at slightly different angles. No real difference was found however, see appendix 6.3. The notch filter was removed for the experiments with the 1064 nm laser light.

3.5.5 1064 nm Optical Setup

As a result of the spatial beam profiles, a new strategy was derived for the experiments on the 1064 nm beam. The beam profiles showed how the diffraction fringes are significant at the position of the nozzle exit. A new strategy was devised to minimize diffraction effects. An ideal setup is shown in Figure 3.17. Here there are two focusing lenses of the same type, most importantly with the same focal length. As the image shows, the aperture is to be placed a distance exactly equal to the focal length in front of the first lens, and the nozzle exit a focal length after the second lens.

With such a setup, the laser beam directly after the aperture will be imaged at the position of the nozzle exit. This is a 1:1-expansion setup simply used for the purpose of collimating the beam and reducing the diffraction effects when the beam must travel a relatively long distance. It is common to also include a pinhole at the focus point of the two lenses to further collimate the beam, but for this setup design the extra aperture might have caused more harm with its own diffraction effects.

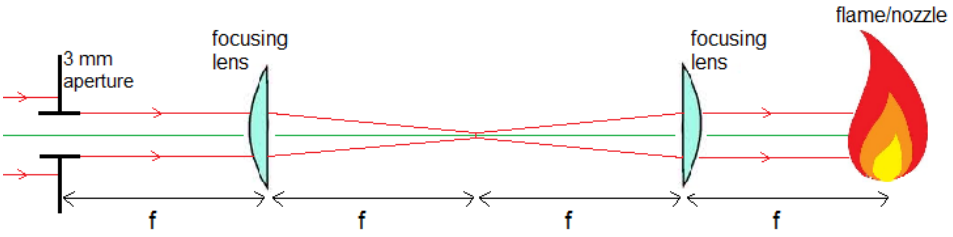

Figure 3.17: New imaging setup to minimize diffraction effects of the 3 mm aperture. The aperture is placed a distance 4f away from the nozzle exit, where f is the focal length of the lenses shown.

The geometry of the lab makes it possible to place a focusing lens a distance between 64 and 85 cm away from the nozzle exit. Also, the distance from the nozzle exit to the top mirror is about 255 cm, with an additional 11.5 cm between the two mirrors. It is therefore not possible to place the new imaging setup after the two mirrors as was originally hoped. The aperture must instead be placed in front of the mirrors, and the two focusing lenses after the mirrors. Two focusing lenses with focal length of 70 cm were ordered, and the distance between the aperture and the nozzle exit was in turn chosen to be 280 cm.

With this new design, the half-wave plate and beamsplitter would be moved to be in front of the 3 mm aperture, so as to not interfere with the 1:1-imaging setup. Figure 3.18 shows the geometry of the lab and the new optical setup for the 1064 nm laser beam. The LII measurements presented in section 4.3 were taken before the two focusing lenses shown in the figure were implemented into the optical setup.

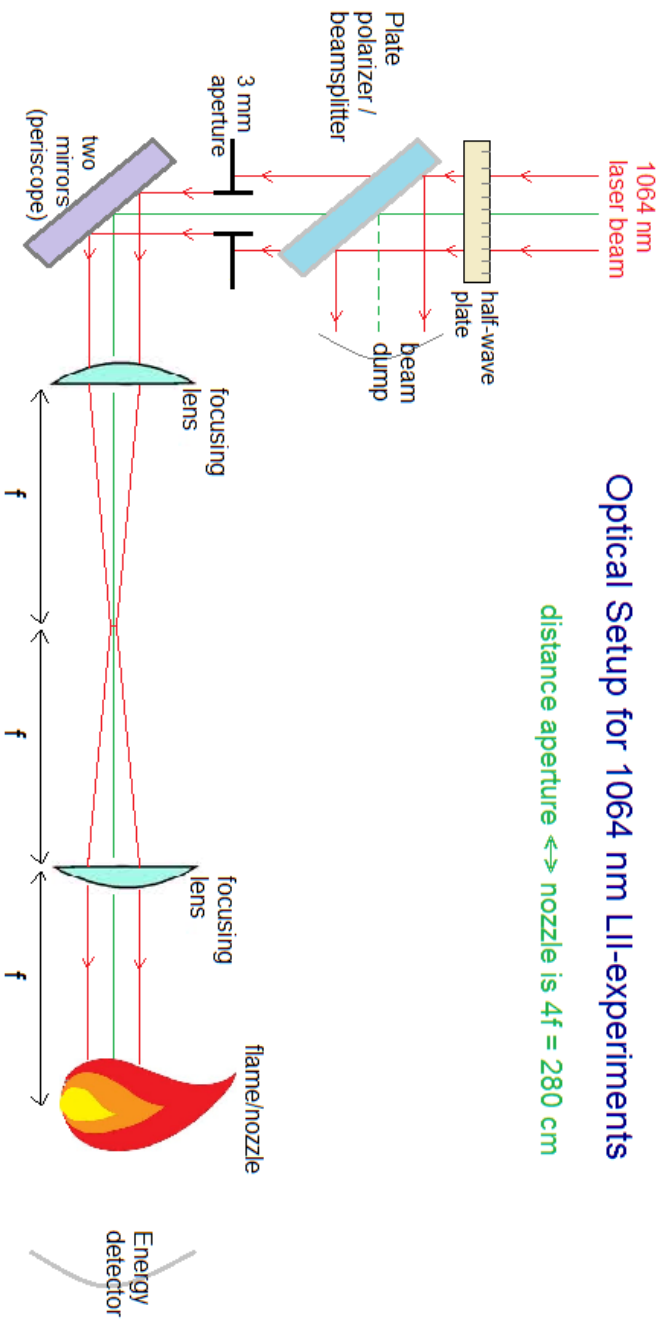

Figure 3.18: Sketch showing the geometry of the lab and the new optical setup for the 1064 nm laser beam experiments. The optical components are a half-wave plate, a beamsplitter, a 3 mm aperture, two mirrors and two focusing lenses.

Half-wave Plate and Plate Polarizer/Beamsplitter

For the 532 nm laser light, a polarizing cube beamsplitter was used and ultimately burned at its beamsplitting intersection. As stated on the manufacturer ThorLabs' own website: "for applications where extinction ratio, transmission, or damage threshold is necessary, these plate polarizers are the preferred option over polarizing beamsplitter cubes". With this in mind, a plate polarizer was ordered for the 1064 nm LII experiments.

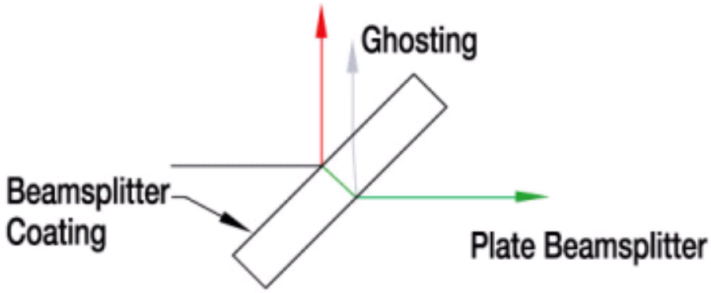

Figure 3.19: Plate polarizer or beamsplitter with 45 ° incidence angle. The green arrow signifies the allowed transmitted light which continues further to the 3 mm aperture and eventually the flame. Figure from the manufacturer ThorLabs Inc.

As specified in Figure 3.19, one side of the plate polarizer has a beamsplitter coating while the other side is uncoated. It is therefore important that the laser light impacts the coated side first. The plate polarizer is made so that s-polarized light is reflected and p-polarization is allowed to pass through. As depicted in the figure, a 45 ° incidence angle is the optimal setup for this polarizer. A beam dump catches the unwanted reflected light, while the transmitted light continues to the 3 mm aperture.

As described, a half-wave plate rotates the polarization of incoming light a certain degree dependent on its angular orientation. Figures 3.20 and 4.17 show the trigonometric energy variation achieved by varying the orientation angle of the half-wave plate in the interval $[0°, 90°]$.

As the Figure 3.20 depicts, the experimental setup makes it possible to vary the fluence of the laser beam. The 200 ns laser pulse used to create the following graph has a measured fluence range of [0.024, 1.87] J/cm^2.

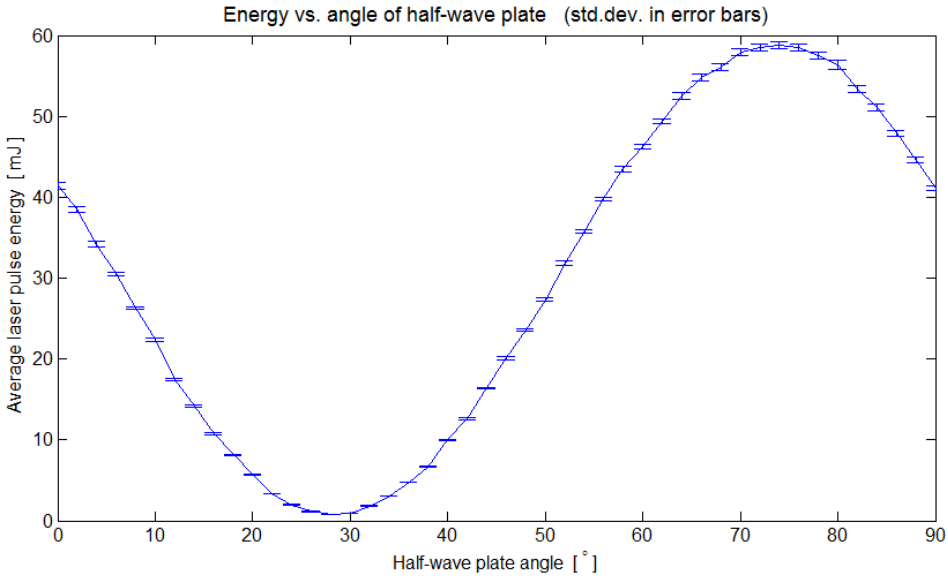

Figure 3.20: Measured average pulse energy with respect to angle of the half-wave plate. Energy was measured at a position after the nozzle exit, with no flame present, using the 200 ns laser pulse. Each energy measurement is an average of 200 pulses and the error bars show the corresponding standard deviation. The measured fluence range is [0.024, 1.87] J/cm^2.

3.6 Temporal Properties of Laser Pulses

Inside the laser, the laser beam from the CW Nd:YAG laser passes through an electro-optical modulator and is further amplified in three stages by flashlamp amplification, see section 3.3. Rectangular temporal laser pulse shapes had previously been created. Temporal LII measurements will be presented for the following pulse durations: 50, 100, 150, 200, 250, 300, 350, 400 and 450 ns. Each of these have different delay times that are sent to the three flash lamps or optical amplifiers. All waveforms had originally an exit energy of about 100 mJ for the 532 nm laser. However, due to general decrease in the laser's energy, they had at the time of experiment an initial energy lying more around 80 mJ.

3.6.1 Example Images

Figure 3.21 shows the captured elastic scattering signal from the particles the laser beam hits. As the figures show, there is a great variety in the amount of intensity registered throughout the 2D image. Rayleigh scattering from the air returns an average intensity well above the background intensity. This is the scattering signal which will give a clear indication of the temporal laser pulse duration and shape. The bright intensity spots seen

in the example images is the result of parasitic Mie scattering, caused by larger particles than the molecular air particles.

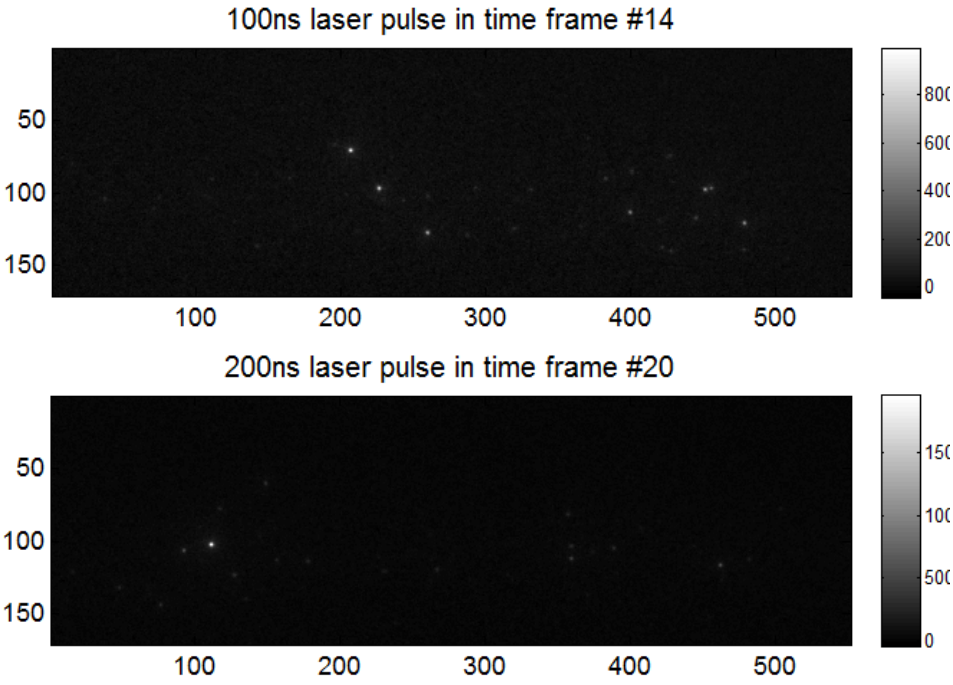

Figure 3.21: Example image captured of elastic scattering from the 100 ns and the 200 ns laser beam interacting with air and also some larger dust particles. Due to 5 ns gate width, only a few intensity spots are visible in each frame. These bright spots are parasitic elastic Mie scattering, with intensity much larger than the Rayleigh signal.

In order for the temporal shape of the laser to be compared with the full LII measurements shown in the next chapter, the ICCD camera could only be opened for 5 ns per image. The images above were created with this 5 ns shutter opening, a gain of 80 or 100 and either 20 or 25 accumulations on the CCD-chip itself before being sent to the computer. An image of the background noise was taken before measurements began, and this noise has been removed in the intensity images and data presented here.

It was also possible to accumulate images on the computer, but this would also accumulate the noise. A better signal to noise ratio can be accomplished be accumulating directly on the CCD-chip and only sending the resulting intensity data one time to the computer. However, great care had to be taken so as not to saturate the camera's pixels. This put a constraint on the applied gain and number of on-CCD accumulations. Parasitic Mie scattering presented the problem that sudden spikes in intensity would be captured by a few pixels. This set the limit for gain and number of on-CCD accumulations used.

3.6.2 Approximate Average Temporal Pulse Shapes

The temporal intensity profile was analyzed so that the laser profile could be included in the figures of the temporal LII signals presented later. Figures 3.23 - 3.30 show the average temporal shape of the different pulse durations, see also appendix 6.4. The average pixel intensity was found for each frame of the 100 frames taken per measurement, within a chosen ROI.

For each pulse duration, four or five elastic scattering measurements were done. In order to find a realistic average pulse shape of the Rayleigh scattering signal, the parasitic intensity spikes of the original signals were removed. A Savitzky-Golay filter was also used to smooth the resulting curves before averaging them together, and also to further smooth the averaged temporal profile. This filter is a generalized moving average with filter coefficients determined by an unweighted linear least-squares regression and a polynomial model of specified degree, here five. The method works with nonuniform predictor data. The smoothening was only performed in the time interval when the laser was present, i.e. the pulse duration. Figure 3.22 shows how the original scattering signals are processed before being averaged together.

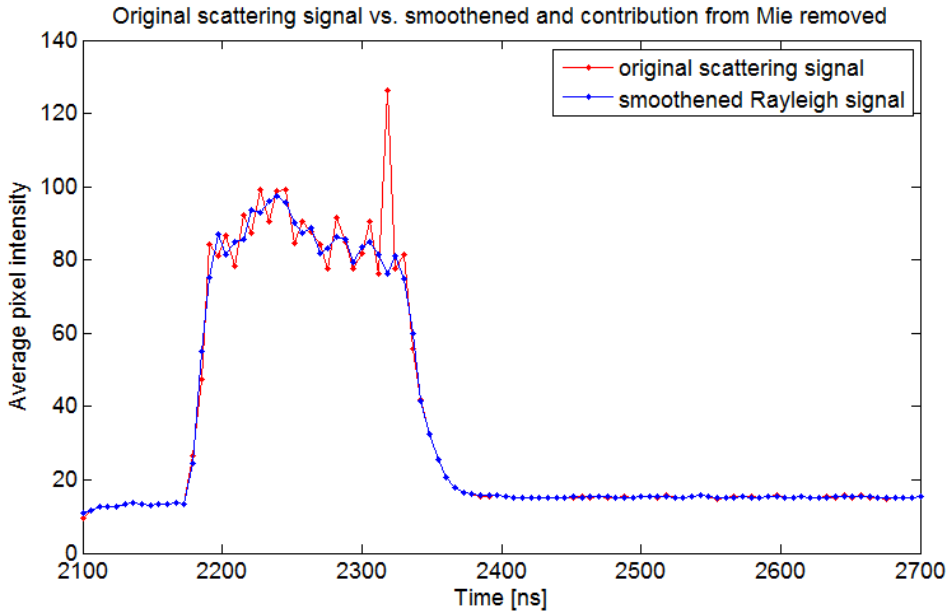

Figure 3.22: The original elastic scattering signal from the first measurement of the 150 ns laser beam interacting with particles in its path. In the blue curve, the parasitic intensity spikes from Mie scattering have been removed from the signal as it is the Rayleigh scattering which is of interest. The blue curve has also been smoothened using the Savitzky-Golay filter in the time interval the laser was present. The processed signal is further averaged with the other 150 ns measurements and the smoothened averaged signal is depicted in Figure 3.25.

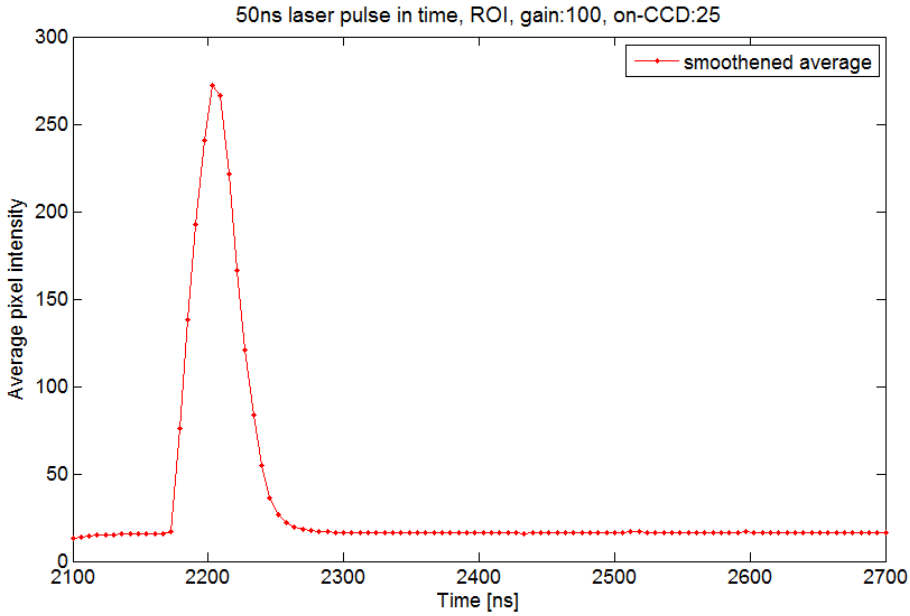

Figure 3.23: Rayleigh scattering signal from the 50 ns laser beam. The smoothened average signal is shown, see Figure 6.5 for the original signals.

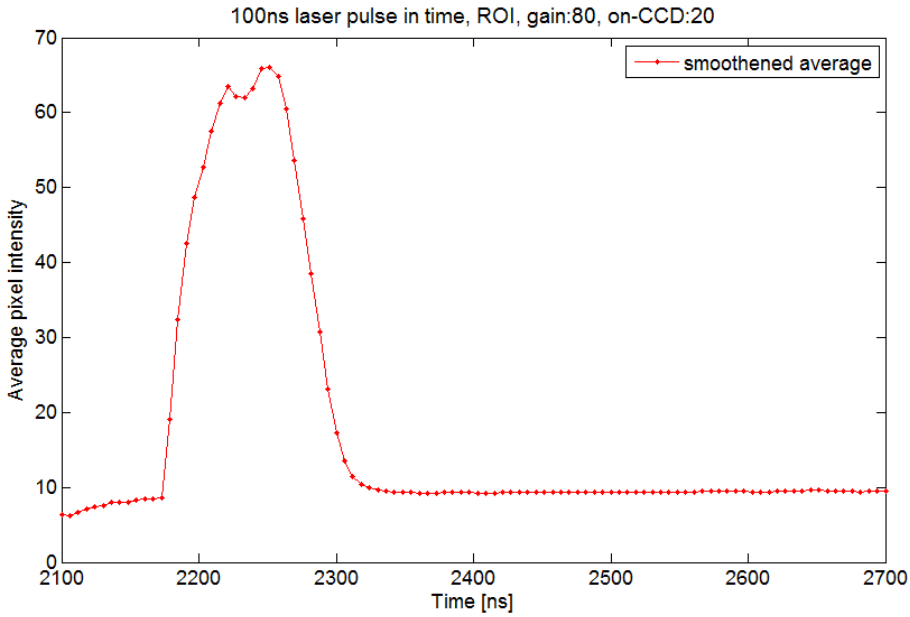

Figure 3.24: Rayleigh scattering signal from the 100 ns laser beam. The smoothened average signal is shown, see Figure 6.6 for the original signals.

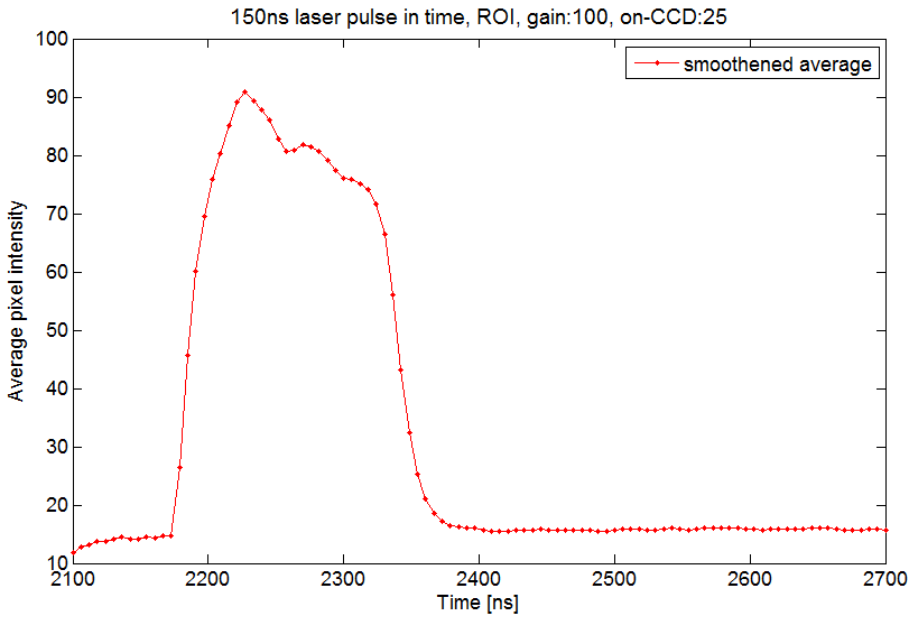

Figure 3.25: Rayleigh scattering signal from the 150 ns laser beam. The smoothened average signal is shown, see Figure 6.7 for the original signals.

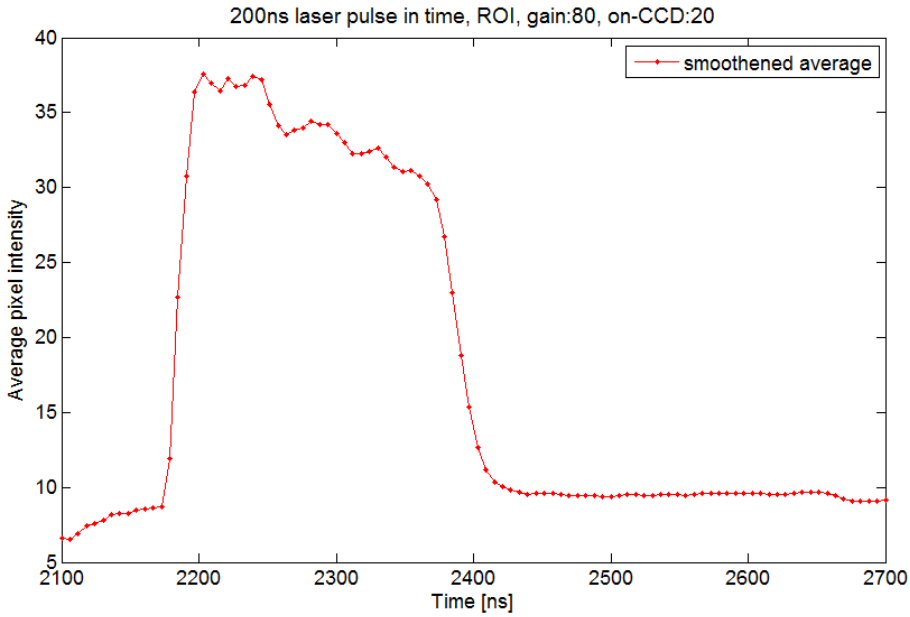

Figure 3.26: Rayleigh scattering signal from the 200 ns laser beam. The smoothened average signal is shown, see Figure 6.8 for the original signals.

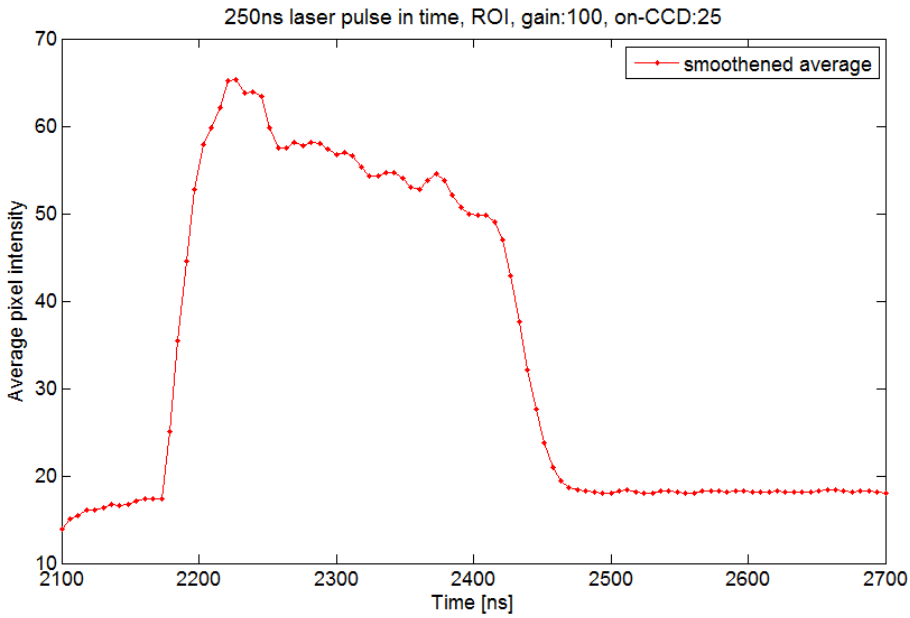

Figure 3.27: Rayleigh scattering signal from the 250 ns laser beam. The smoothened average signal is shown, see Figure 6.9 for the original signals.

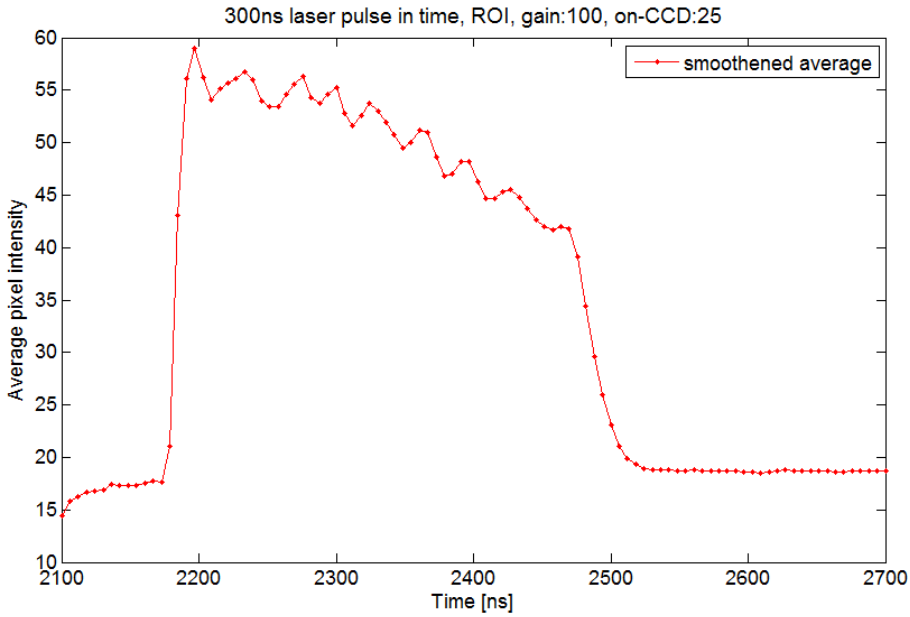

Figure 3.28: Rayleigh scattering signal from the 300 ns laser beam. The smoothened average signal is shown, see Figure 6.10 for the original signals.

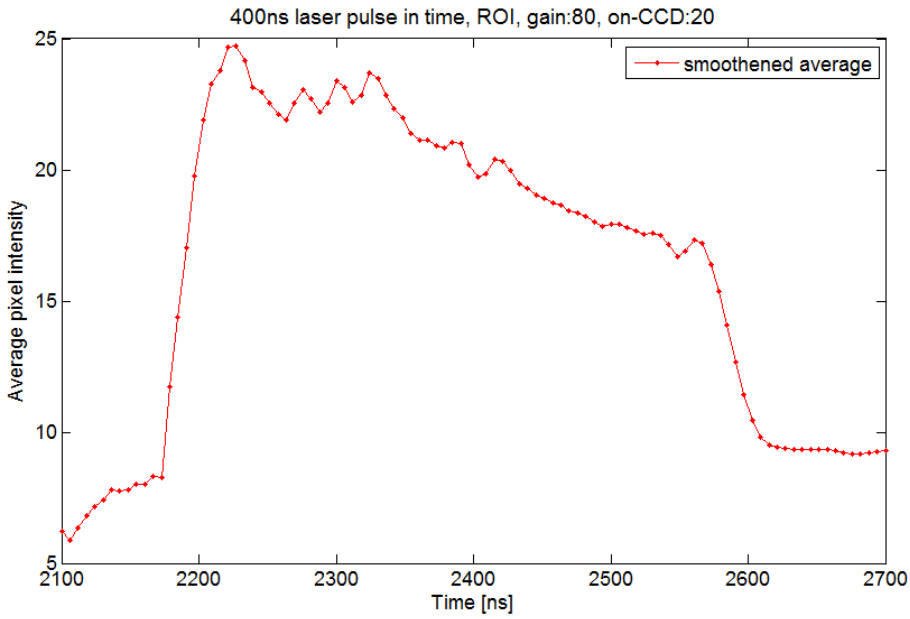

Figure 3.29: Rayleigh scattering signal from the 400 ns laser beam. The smoothened average signal is shown, see Figure 6.11 for the original signals.

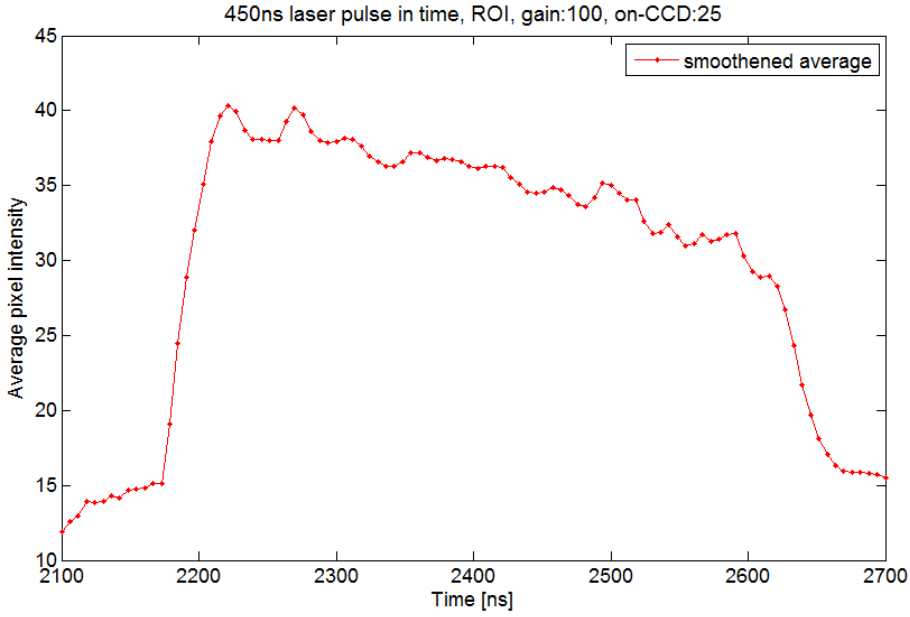

Figure 3.30: Rayleigh scattering signal from the 450 ns laser beam. The smoothened average signal is shown, see Figure 6.12 for the original signals.

3.7 Camera Settings for the LII Measurement Images

The measurements of the LII signal in time were taken using a gain of 200 and on-CCD accumulation of two images. A gate width of 5 ns was used. Images were taken in the time interval 2100 to 2700 ns as the gate delay of the ICCD camera, i.e. in a 600 ns time interval. Each LII measurement consists of 100 images or frames and the delay increment was 6.06 ns. As can be seen in the figures presented for the temporal LII signals in section 4, the 532 nm laser beam reaches the flame in approximately frame #14.

In comparison with the previous results obtained at SINTEF (Ditaranto et al., 2013), it is important to clarify that the gate width for these experiments is 5 ns instead of 10 ns. In the previous experiments ten images were accumulated on-chip, while only two images are accumulated on-CCD here. The laser beam's spatial profile was also very different.

A region of interest (ROI) was chosen by cutting away the areas of the original full field of view that were outside the area where the laser impacted the flame and LII signal was seen. The camera's full field of view was 1024x251, and the chosen ROI was 551x171. The images were taken as .SPE-files and later converted to 3D intensity matrices in MATLAB, where they were further analyzed. Figure 3.31 shows frame #20 of 100 for the 100 ns pulse, and in turn the dimensions of the chosen ROI.

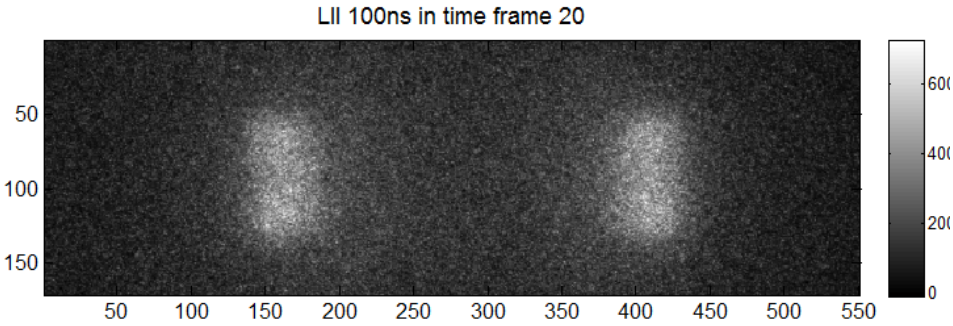

Figure 3.31: 100 ns, frame #20 of 100

3.8 Background Noise Analysis

Before taking any LII measurements, a sample image of the background noise is collected. This background image has the same camera settings as the LII images, the only difference being that only one image is collected instead of 100. Figure 3.32 shows the average pixel intensity value of three such background files, $Back\_1 - \_3.spe$. WinSpec has a built in command to remove the sampled effect of the background noise in its further measurements.

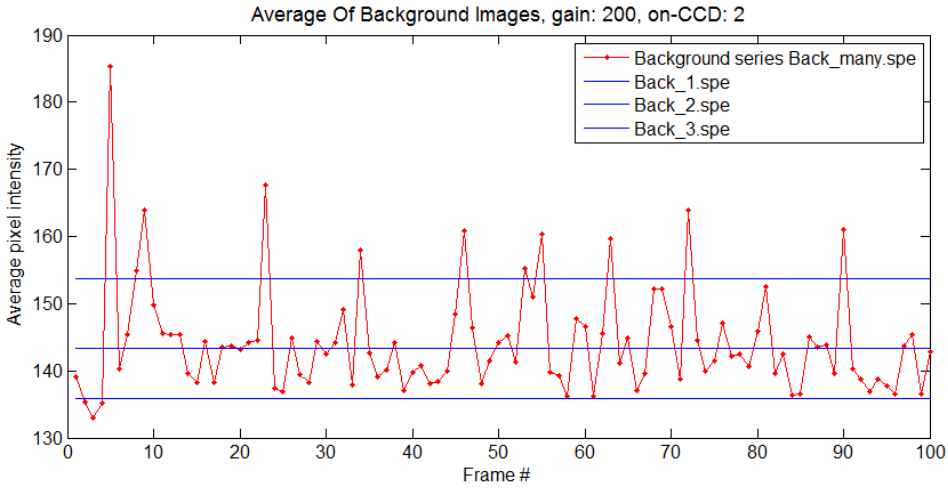

Figure 3.32: Comparison of two ways to collect the background noise, a single image vs. a series of 100 background images.

Figure 3.32 also shows the average intensity of each image in a collection of 100 frames labeled as $Back\_many.spe$. These images were taken using exactly the same settings as the LII measurements and not generated by WinSpec to be a single background image. As the figure shows, the background noise varies a little in average pixel intensity throughout the 100 images. To get as reliable and noise free LII measurements as possible, the original idea was to create an average background image from the image series $Back\_many.spe$ and feed it back to WinSpec. However, Princeton Instruments made WinSpec in such a way as to only handle files of .spe format.

Analyzing .spe files was possible in this project only after extensive research in how to import .spe images as matrices in MATLAB. A solution was unfortunately not found for how to create a .spe file from a matrix in MATLAB, and it was therefore not possible to feed WinSpec an averaged background image. In further LII measurements, a single background image was collected by WinSpec, and in the presented temporal LII signals the effect of the background noise has in such a way been removed.

3.9 Energy Absorption of Flame

An energy detector is placed after the fuel nozzle so as to monitor the laser energy simultaneously as the LII measurements. Laser energy measurements were taken before the nozzle and after the nozzle, with the flame not present. For security reasons, the energy detector after the nozzle was encapsulated to contain as much of the reflections

from the 532 nm laser light as possible. This results in a slight loss in the amount of energy measured. The loss was about 10 %, see appendix 6.2. The 1064 nm LII measurements has a slightly different encasement with much less resulting loss in the energy detected.

There is also some energy loss due to the flame, but only a small percentage of the laser energy is absorbed by the particles in the flame. Figure 3.33 shows energy measurements taken with and without the flame present. Eight measurements, each an average of 500 pulses, were taken before turning on the flame, then while the flame was present and at last after the flame had been turned off. The laser itself varies its energy with 1-2 %, but a small decrease in average energy was found in the measurements with the flame present. The decrease in average energy showed an energy absorption of about 1-2 %. For the 532 nm LII results presented in section 4.2, the laser pulse energy reaching the flame can be estimated as $1.11 \cdot E_{after\,flame}$.

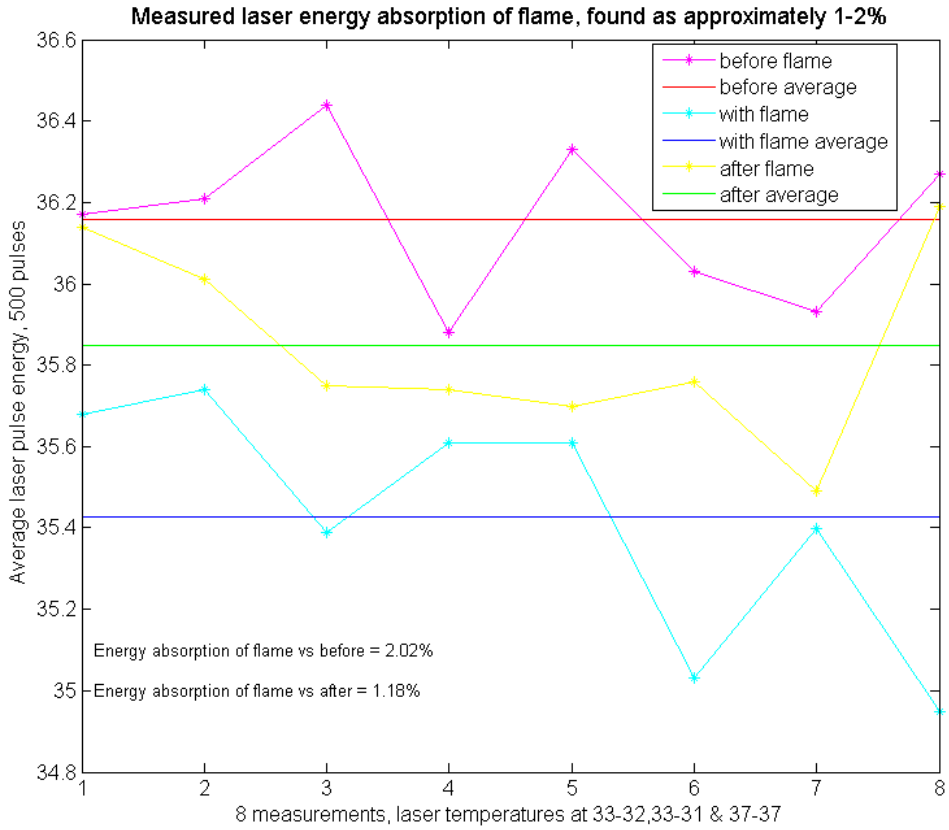

Figure 3.33: Laser pulse energy with and without a flame present. Each data point represents an average energy of 500 pulses. The output energy of the laser itself varies with 1-2 %. An additional reduction of about 1-2 % was found when the laser had to pass through the flame.

4 Experimental Results

4.1 Finding Maximum Average Intensity Per Frame

The average maximum LII signal is found along y=88, in other words near the center of the chosen ROI. This is done by finding the average intensity of one pixel at y=88 and its eight closest neighbors. All x-values are then checked, and the maximum average value for the specific frame is finally found. As long as a certain y-position is chosen and maximum intensity is found along this height, the flickering of the flame isn't of much consequence.

As Figure 4.4 shows, the laser pulse impacts the flame at about 2.18 μs and the pulse lasts 200 ns. The LII signal remains even after the laser pulse is gone. The figure shows five different measurements and also the average temporal LII profile of these five measurements.

4.2 532 nm Experimental Results

The laser beam energies vary slightly for the different pulse durations, but lie around 40 mJ. As mentioned, the cube beamsplitter that was intended to be used in the 532 nm optical setup was damaged. It was therefore not possible to vary the laser pulse fluence in the 532 nm LII experiments. Using the measured beamwidth of 1.94 mm presented in Figure 3.7, a 40 mJ pulse energy corresponds to a fluence of 1.35 J/cm^2. One must mention that the diffraction effects are quite prominent and the Gaussian fit used to calculate the beamwidth is therefore not entirely precise. The diffraction effects were not as prominent however, in the images of the spatial laser beam profile for the 1064 nm laser beam with calculated beamwidth of 2.0 mm.

Figures 4.1-4.9 show the temporal LII signal using different pulse durations. As Figure 4.9 shows, the temporal LII measurements are highly reproducible.

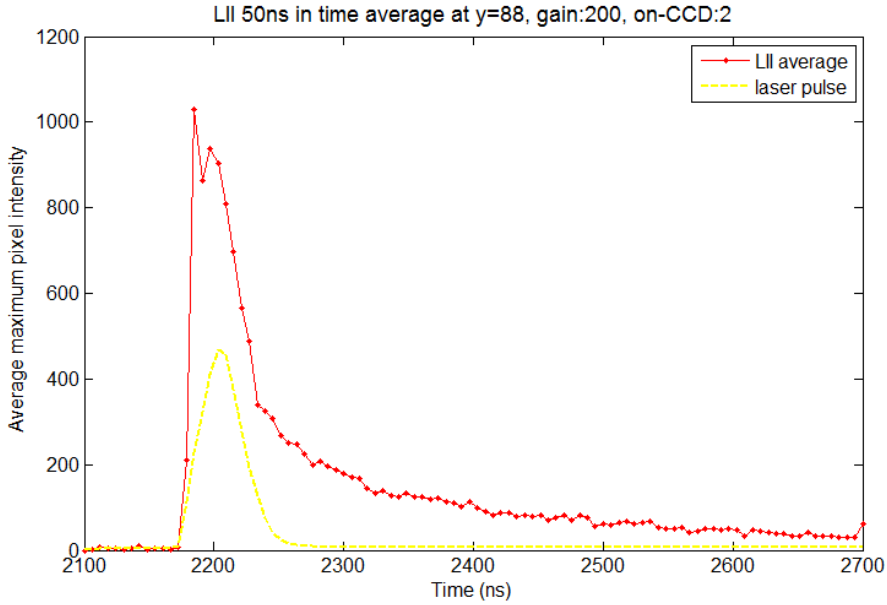

Figure 4.1: Temporal average LII signal using the 50 ns pulse duration. The laser pulse is shown by the dotted yellow line. Average pulse energy at 42.3 mJ, corresponding to 1.43 J/cm^2.

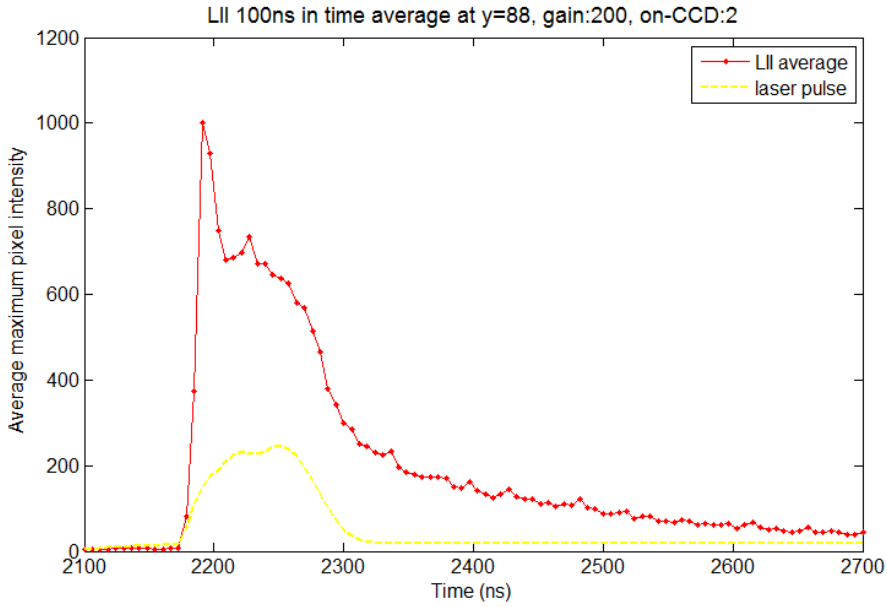

Figure 4.2: Temporal average LII signal using the 100 ns pulse duration. The laser pulse is shown by the dotted yellow line. Average pulse energy at 42.2 mJ, corresponding to1.43 J/cm^2.

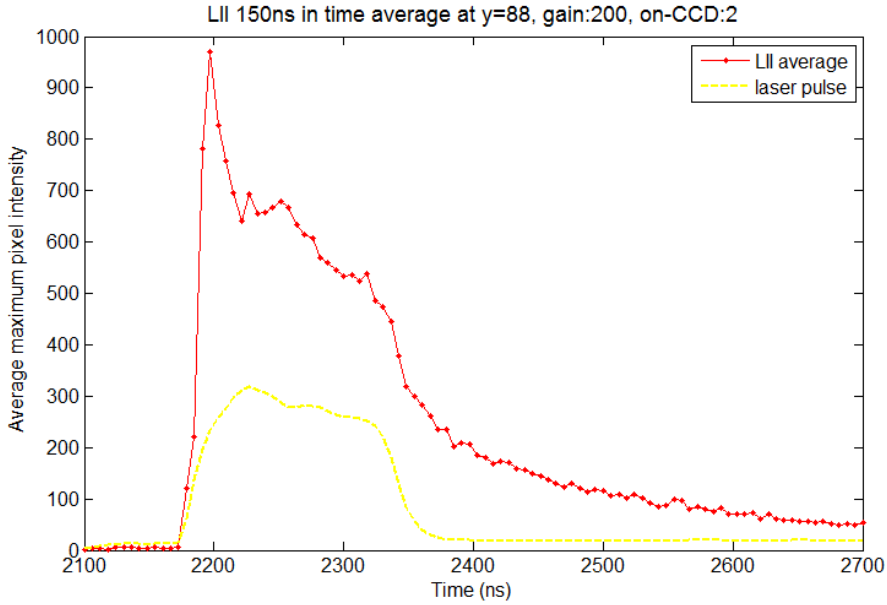

Figure 4.3: Temporal average LII signal using the 150 ns pulse duration. The laser pulse is shown by the dotted yellow line. Average pulse energy at 42.6 mJ, corresponding to 1.44 J/cm^2.

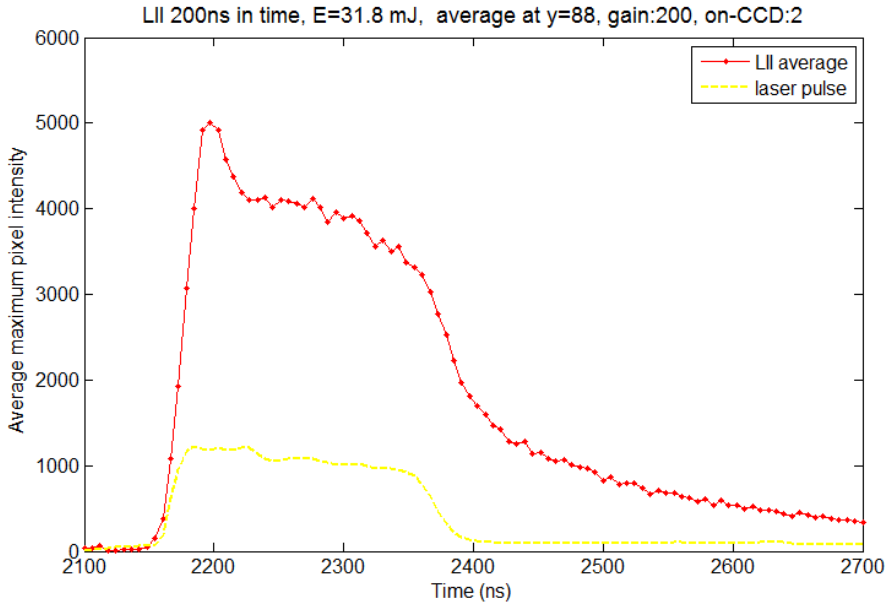

Figure 4.4: Temporal average LII signal using the 200 ns pulse duration. The laser pulse is shown by the dotted yellow line. Average pulse energy at 40.4 mJ, corresponding to 1.37 J/cm^2.

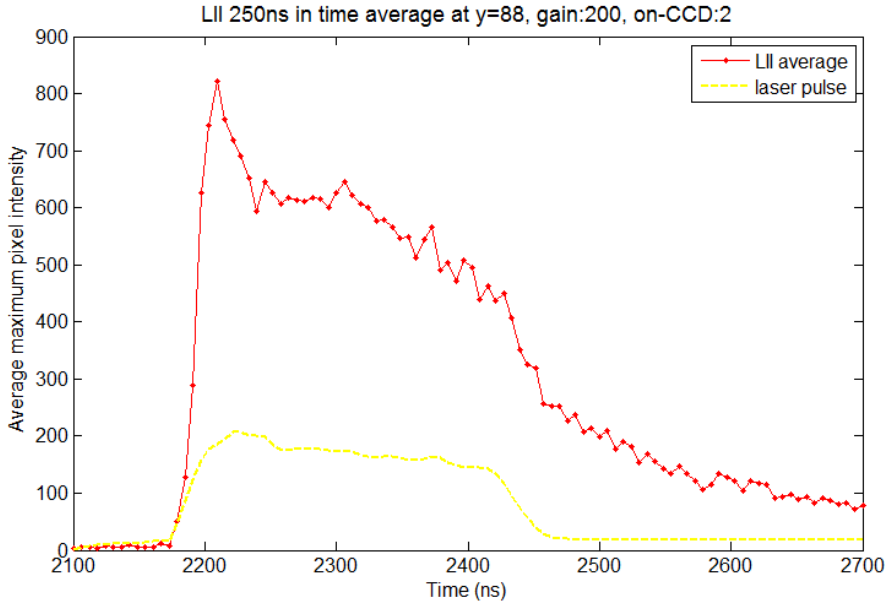

Figure 4.5: Temporal average LII signal using the 250 ns pulse duration. The laser pulse is shown by the dotted yellow line. Average pulse energy at 39.5 mJ, corresponding to 1.34 J/cm^2.

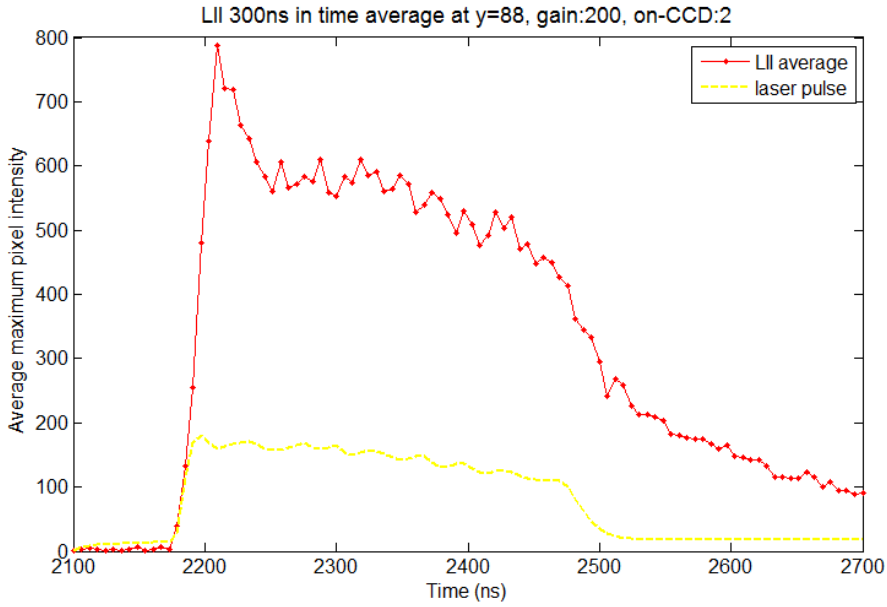

Figure 4.6: Temporal average LII signal using the 300 ns pulse duration. The laser pulse is shown by the dotted yellow line. Average pulse energy at 38.5 mJ, corresponding to 1.30 J/cm^2.

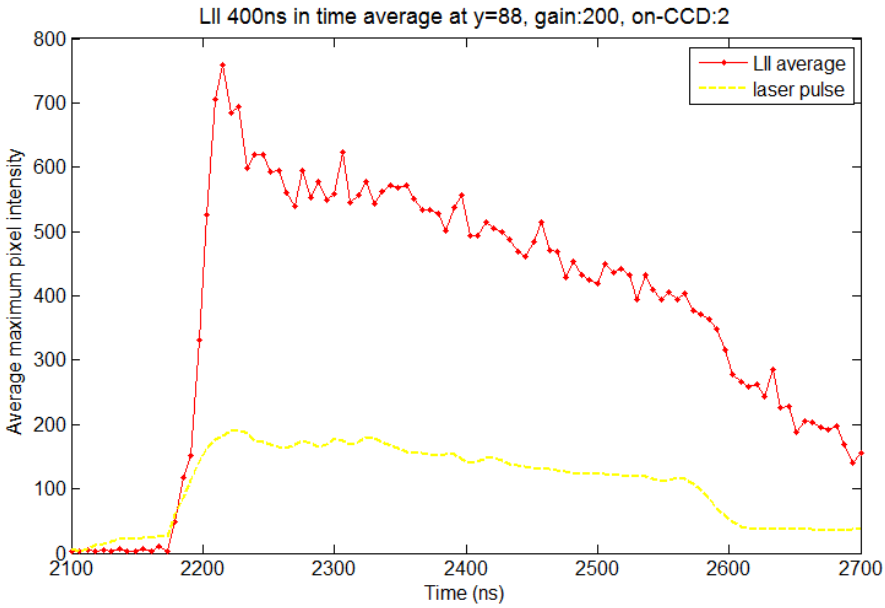

Figure 4.7: Temporal average LII signal using the 400 ns pulse duration. The laser pulse is shown by the dotted yellow line. Average pulse energy at 37.8 mJ, corresponding to 1.28 J/cm^2.

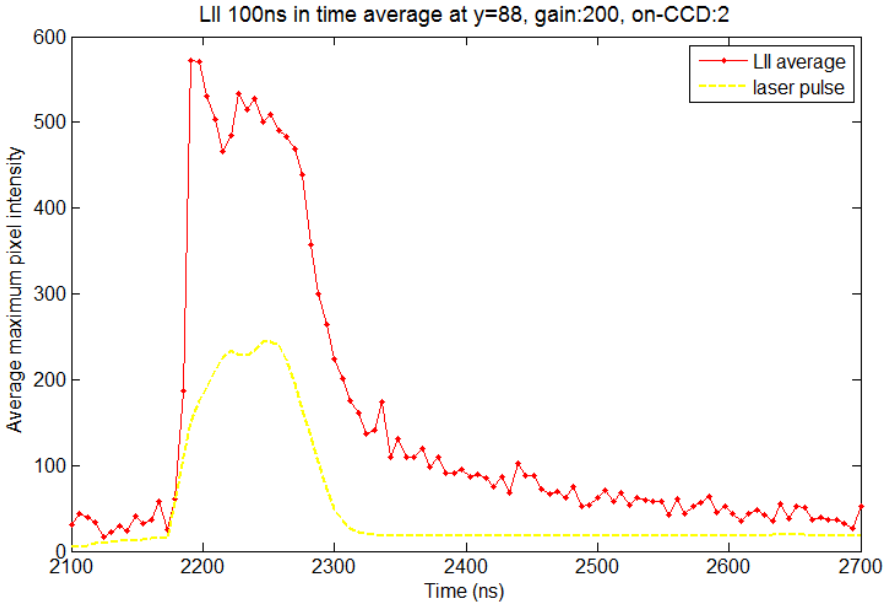

Figure 4.8: Temporal average LII signal using the 100 ns pulse duration, taken test day nr.2. The laser pulse is shown by the dotted yellow line. Average energy at 35.2 mJ, corresponding to 1.19 J/cm^2.

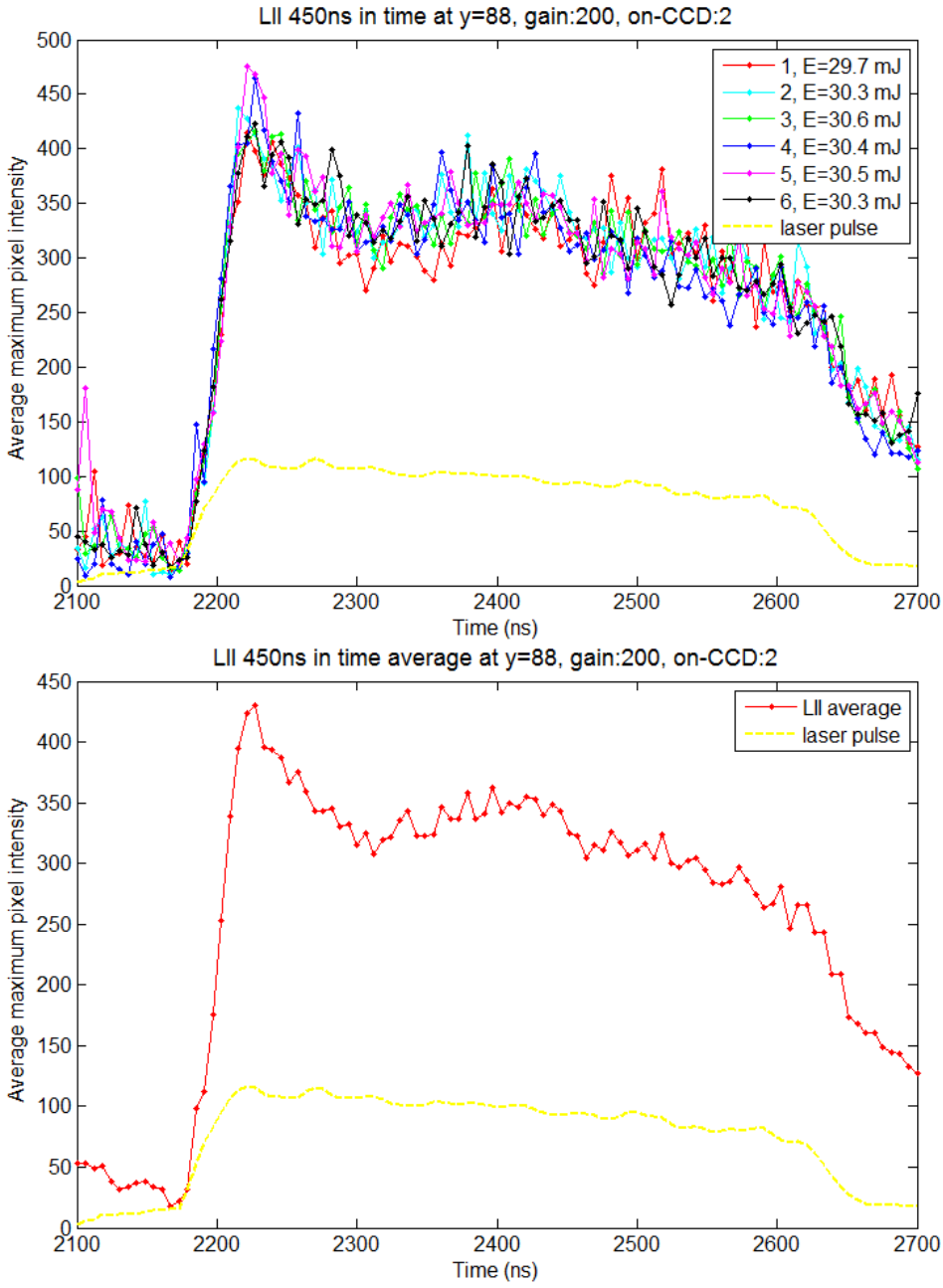

Figure 4.9: Temporal LII signal using the 100 ns pulse duration, taken test day nr.2. The laser pulse is shown by the dotted yellow line. The bottom graph shows the average signal. Average energy at 30.3 mJ, corresponding to 1.03 J/cm^2.

Comparison of Pulse Durations

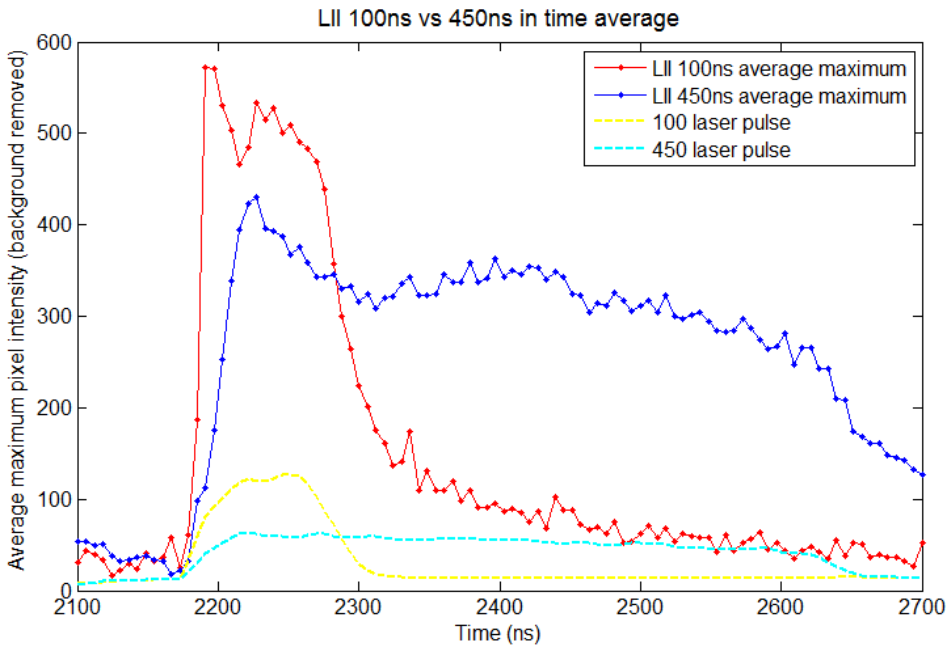

Figure 4.10: Comparison of the 100 ns and the 450 ns temporal LII signals. The dotted lines show the laser pulse durations. The fluence of the 100 ns pulse was 1.2 J/cm^2, while 1.0 J/cm^2 for the 400 ns pulse.

Figure 4.10 shows how the peak of an LII signal of shorter pulse duration and equal fluence rises more quickly. A second peak is clearly visible for the 100 ns pulse, and it can also be seen for the pulse of longer duration. This is consistent with the previous results obtained by C. Meraner (Ditaranto et al., 2013).

4.3 1064 nm Experimental Results

Some preliminary LII measurements were performed before the half-wave plate and plate polarizer were installed, see Figures 4.11-4.15. In other words, in these LII measurements, the laser beam only passed through the 3 mm aperture and the periscope before reaching the flame. Also, background analysis was not performed prior to these preliminary measurements.

As with the 532 nm laser beam experiments, the camera had a gate delay of 2100 ns to 2700 ns, a 600 ns time interval. The camera's gate opening was 5 ns and with 6.06 ns delay increment. Gain was set to 200 as before, with two images accumulated on-CCD.

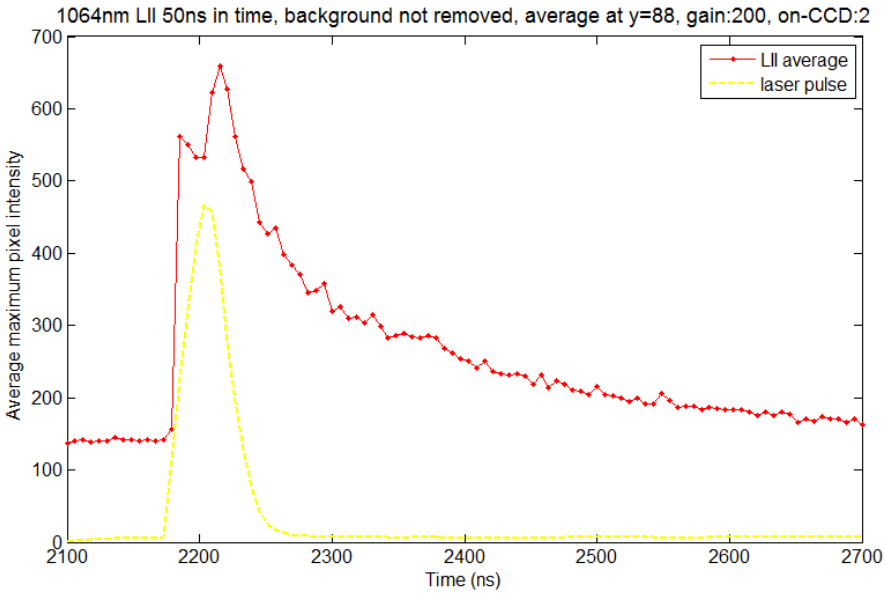

Figure 4.11: Temporal average LII signal using the 50 ns pulse duration. The laser pulse is shown by the dotted yellow line. Note that the background noise has not been removed. Average laser beam energy at 47.6 mJ with corresponding fluence of 1.52 J/cm^2.

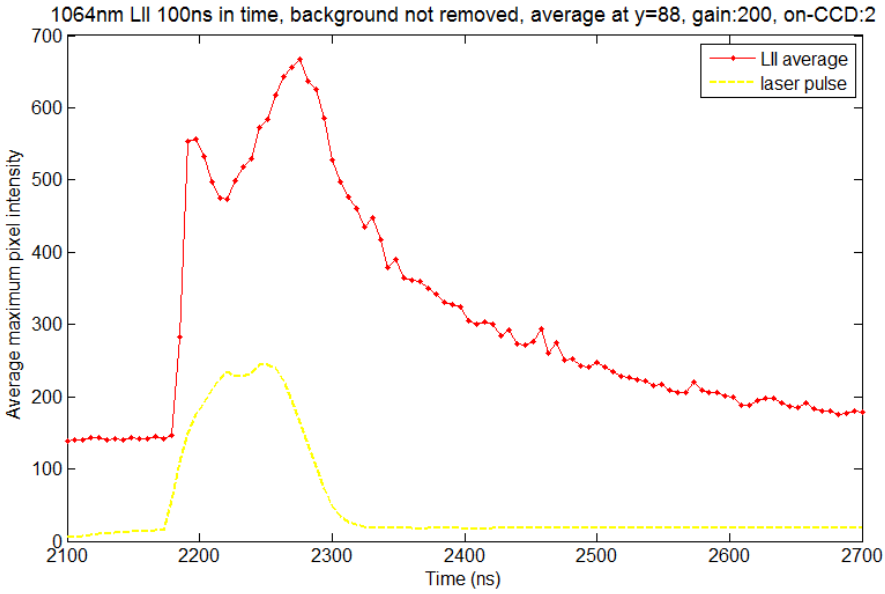

Figure 4.12: Temporal average LII signal using the 100 ns pulse duration. The laser pulse is shown by the dotted yellow line. Note that the background noise has not been removed. Average laser beam energy at 55.4 mJ with corresponding fluence of 1.76 J/cm^2.

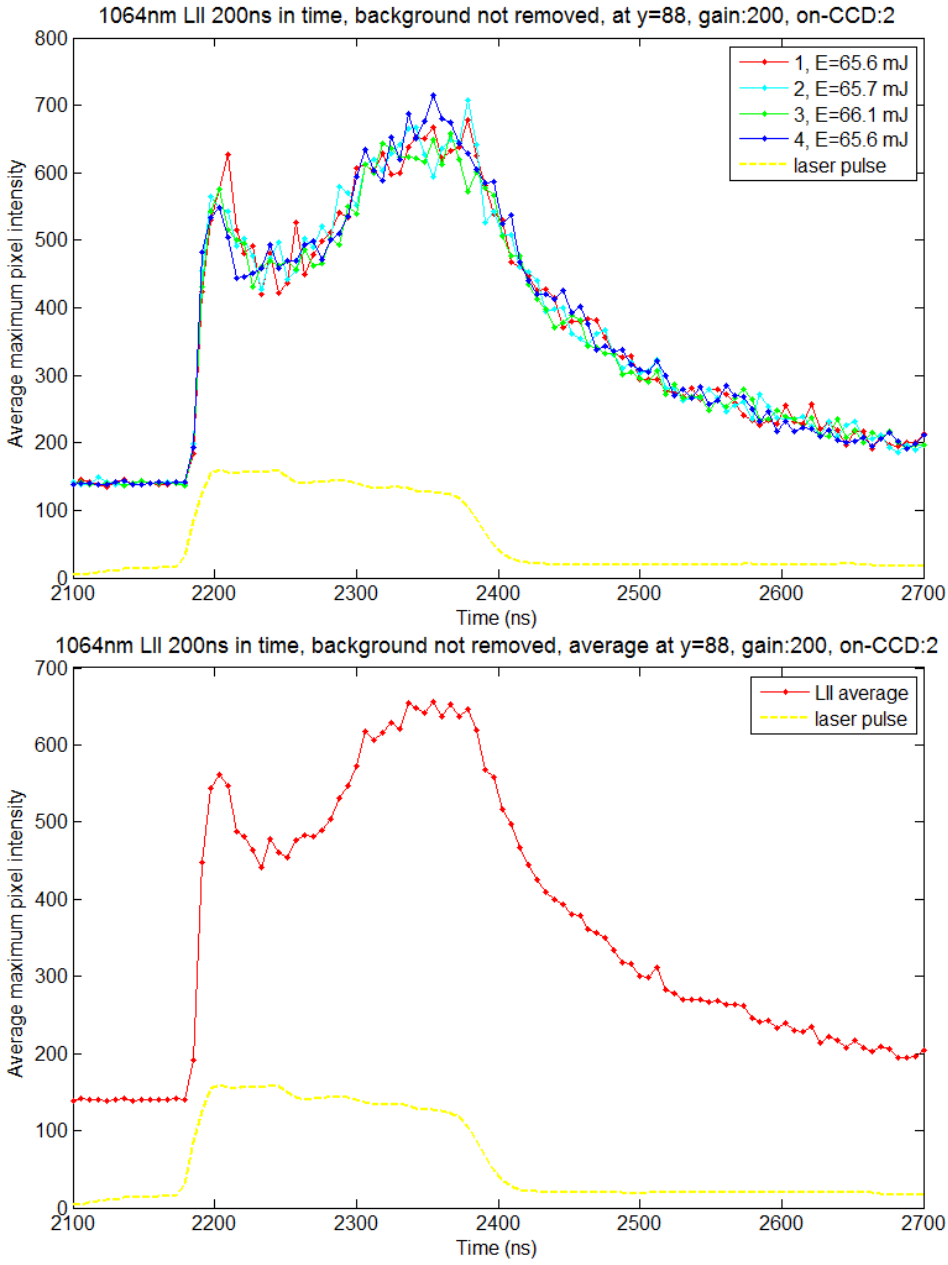

Figure 4.13: Temporal LII signal using the 200 ns pulse duration. The laser pulse is shown by the dotted yellow line. The bottom graph shows the average signal. Note that the background noise has not been removed. Average laser beam energy at 65.7 mJ with corresponding fluence of 2.09 J/cm^2.

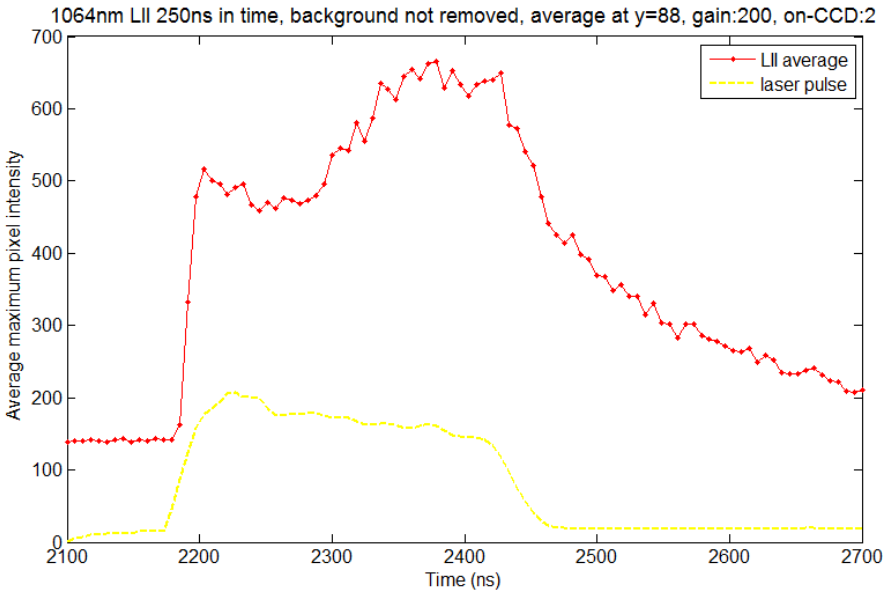

Figure 4.14: Temporal average LII signal using the 250 ns pulse duration. The laser pulse is shown by the dotted yellow line. Note that the background noise has not been removed. Average laser beam energy at 69.7 mJ with corresponding fluence of 2.22 J/cm^2.

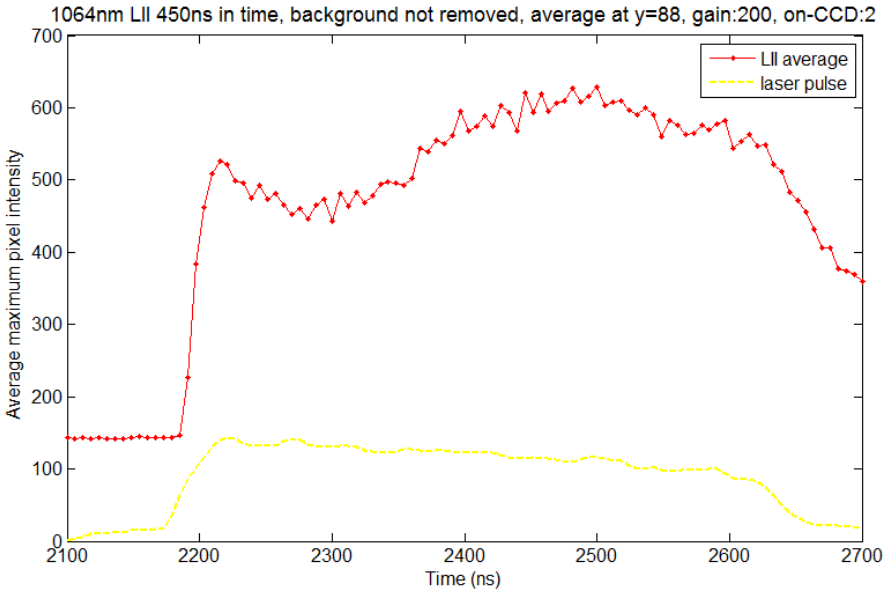

Figure 4.15: Temporal average LII signal using the 450 ns pulse duration. The laser pulse is shown by the dotted yellow line. Note that the background noise has not been removed. Average laser beam energy at 80.4 mJ with corresponding fluence of 2.56 J/cm^2.

Comparison of Pulse Durations

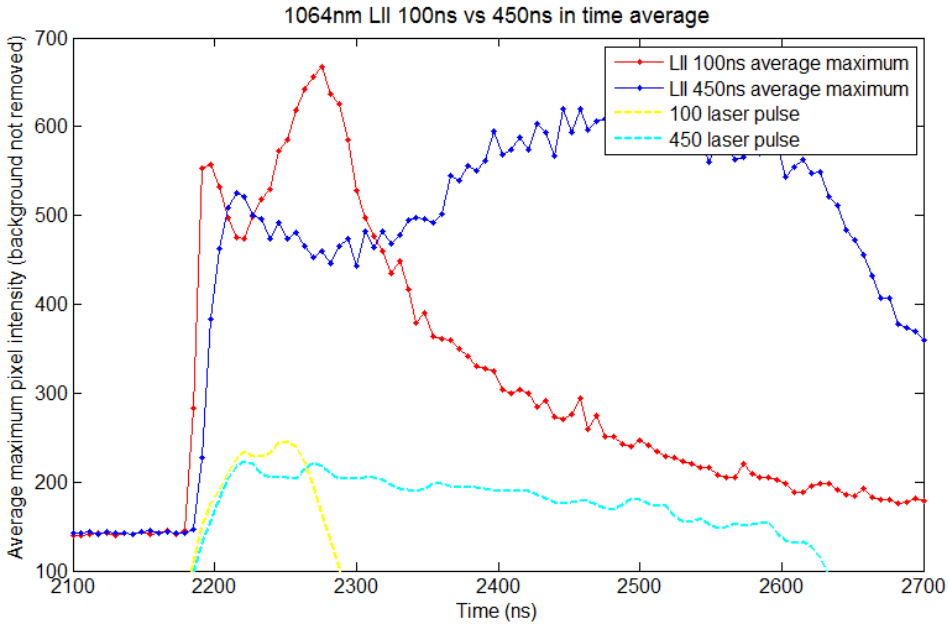

Figure 4.16: Comparison of the 100 ns and the 450 ns temporal LII profiles. The dotted lines show the laser pulse durations. Fluence of the 100 ns pulse was 1.76 J/cm^2, while the 400 ns pulse had a fluence of 2.56 J/cm^2.

Figure 4.16 shows how the peaks of the LII signals of shorter pulse duration rises more quickly. A second peak is clearly visible for both pulse durations. The laser pulses have here a much higher fluence than the 532 nm laser pulses. This is the consequence of using the first harmonic and also somewhat due to the improvements to the alignment inside the laser.

In the 532 nm laser beam experiments, there was not a great difference in energy between the different temporal laser pulses. However, in the results presented here, the different pulse durations have quite different energy values.

4.4 LII Measurements with Varying Fluence

As the Figure 4.17 depicts, the experimental setup made it possible to vary the fluence of the laser beam. The 200 ns laser pulse used to create the following graph has a fluence range of [0.024, 1.87] J/cm^2, see section 3.5.5. It is important to remember that this fluence value is found using equation (2.18), i.e. by using the average energy collected from the laser pulse. The fluence in the center of the laser beam will thus be of a higher value.

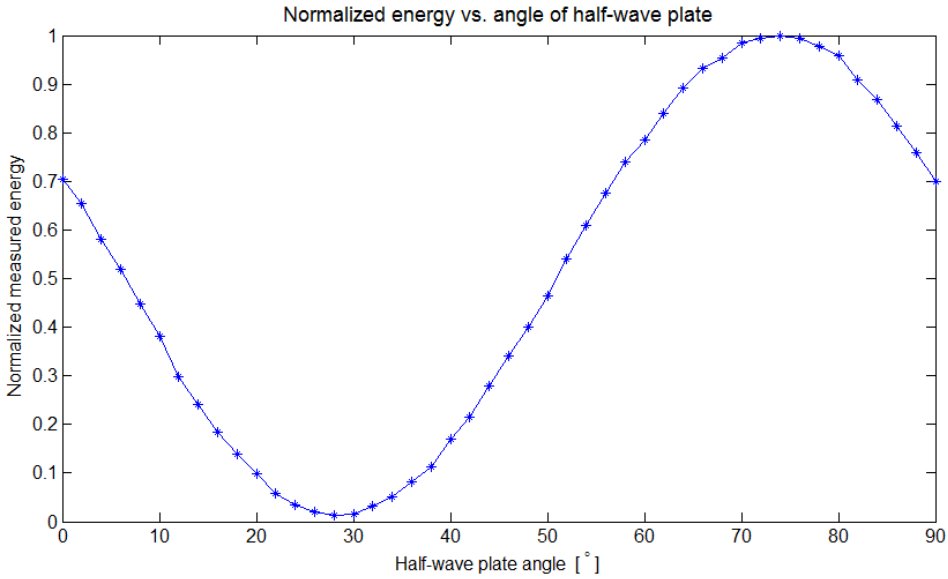

Figure 4.17: Normalized measured energy with respect to angle of the half-wave plate. Normalized version of Figure 3.20.

4.4.1 200 ns Laser Beam with Varying Fluence

Data Series nr. 1

In correspondence with Figure 4.17, the following angles were chosen for LII measurements with varying fluence: [0 °, 8 °, 14 °, 20 °, 28 °, 46 °, 74 °, 84 °]. The measured beam energies corresponding to these angles were [42.7 mJ, 27.0 mJ, 15.3 mJ, 6.8 mJ, 0.8 mJ, 18.5 mJ, 58.7 mJ, 51.3 mJ]. With respect to fluence in increasing order, this corresponds to: [0.027, 0.21, 0.49, 0.56, 0.86, 1.36, 1.63, 1.87] J/cm^2.

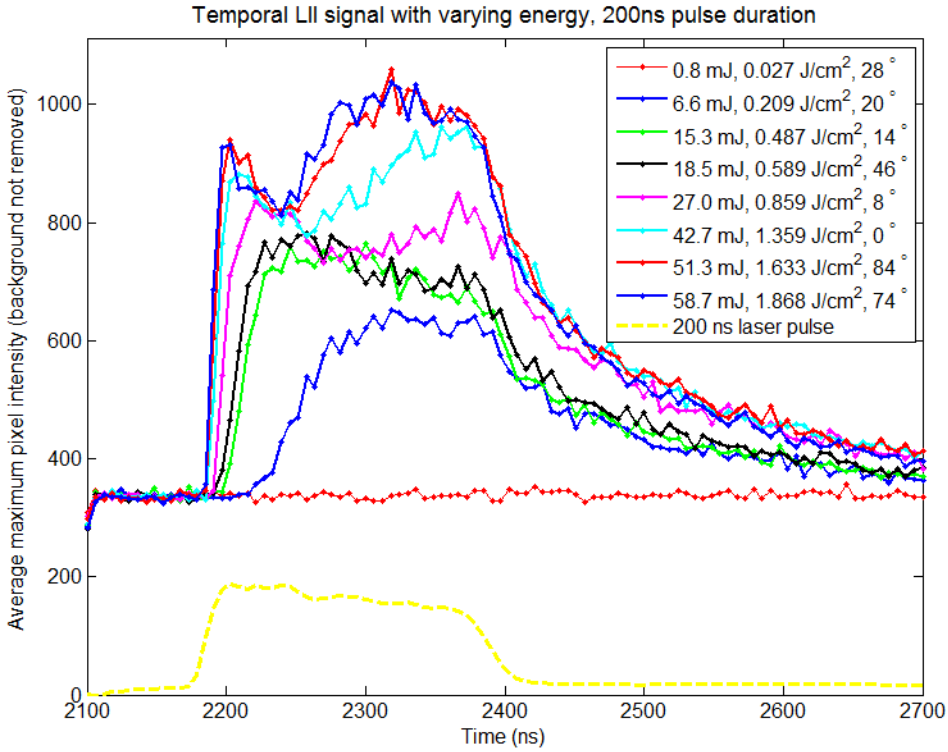

Figure 4.18: Temporal LII signal of the 200 ns pulse duration, with varying pulse fluence. Data series nr. 1. Background was not removed prior to measurements.

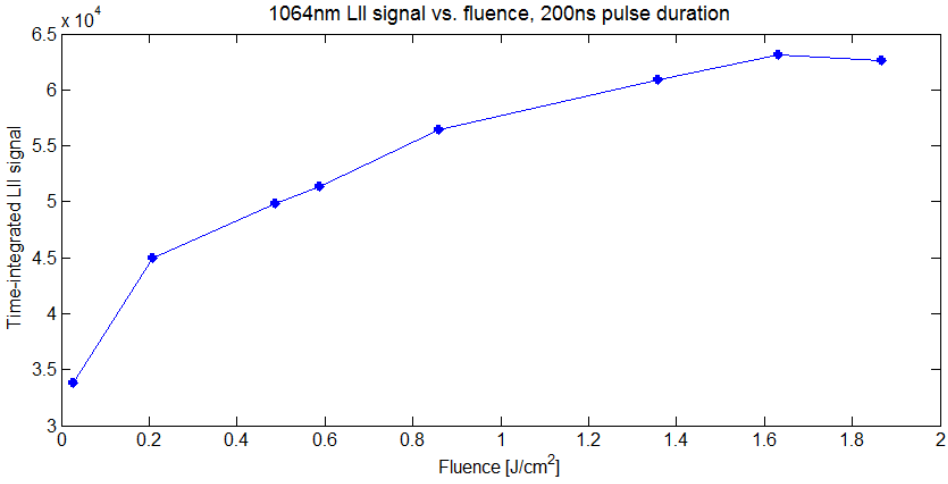

Figure 4.19: Time-integrated LII signal vs. fluence for data series nr. 1 depicted in Figure 4.18.

Data Series nr. 2

A second data series was collected in order to get a more detailed look at the temporal LII signals of the lower fluence values. Starting from 26° with no visible LII and until the second peak strongly appears, the angle on the plate polarizer was decreased by 2° with each LII measurement. From the results shown in Figures 4.20-**??**, the second peak is clearly visible in the temporal LII signals when the laser pulse has a fluence of 0.745 J/cm^2 or more.

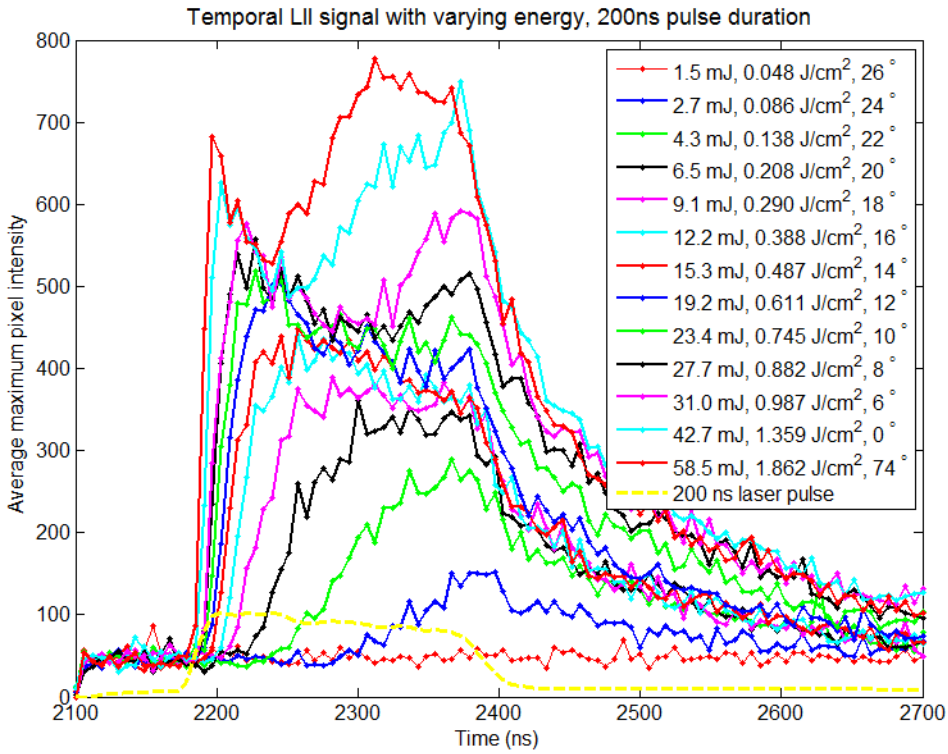

Figure 4.20: Temporal LII signal of the 200 ns pulse duration, with varying pulse fluence. Here all LII measurements from data series nr. 2 are shown. In comparison with Figure 4.18, background was removed prior to these measurements.

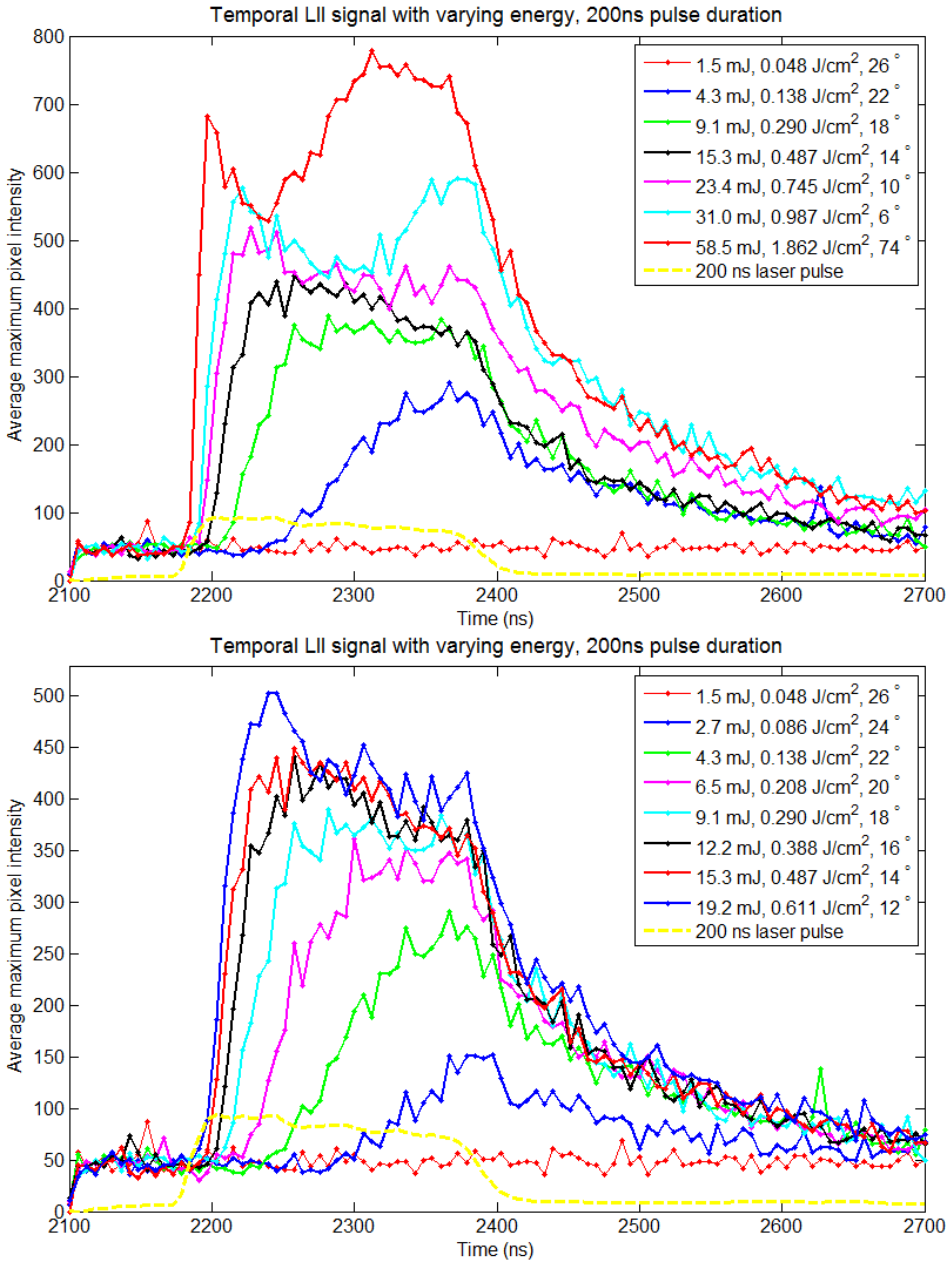

Figure 4.21: Temporal LII signal of 200 ns pulse duration with varying pulse fluence. In the top figure, every other LII measurement from data series nr. 2 is shown for better visibility. In the bottom figure, the LII measurements using low pulse fluence are shown.

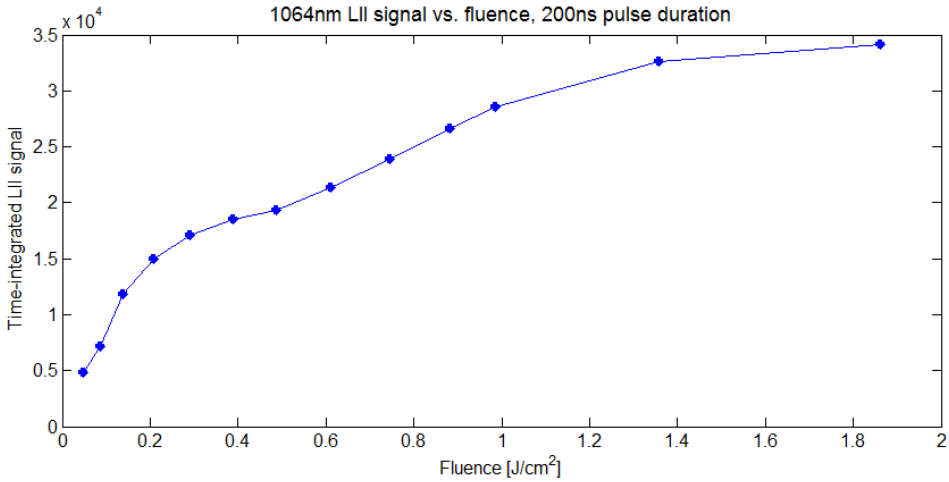

Figure 4.22: Time-integrated LII signal vs. fluence for data series nr. 2 depicted in Figure 4.20.

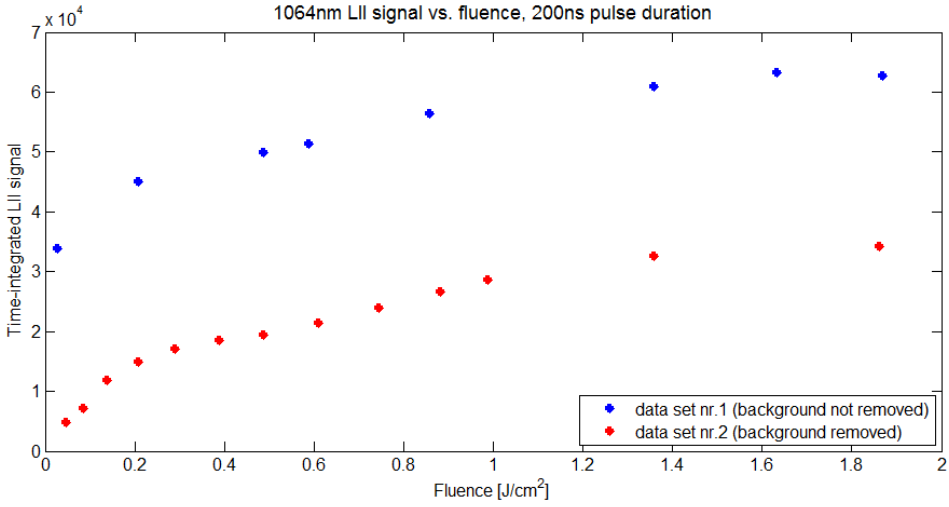

Figure 4.23: Time-integrated LII signal vs. fluence for both data series collected using the laser pulse of 200 ns duration. The background contribution was not removed prior to LII measurements in the first data series.

4.4.2 450 ns Laser Beam with Varying Fluence

For the 450 ns pulse duration tests, angles [28°, 76°] with 4° increase per LII measurement was chosen. The measured beam energies corresponding to these angles were [1.1, 1.8, 4.9, 10.5, 18.8, 27.5, 37.5, 47.0, 55.6, 63.1, 69.0, 71.5, 71.7] mJ. With respect to fluence, this corresponds to a range of [0.034, 2.282] J/cm^2.

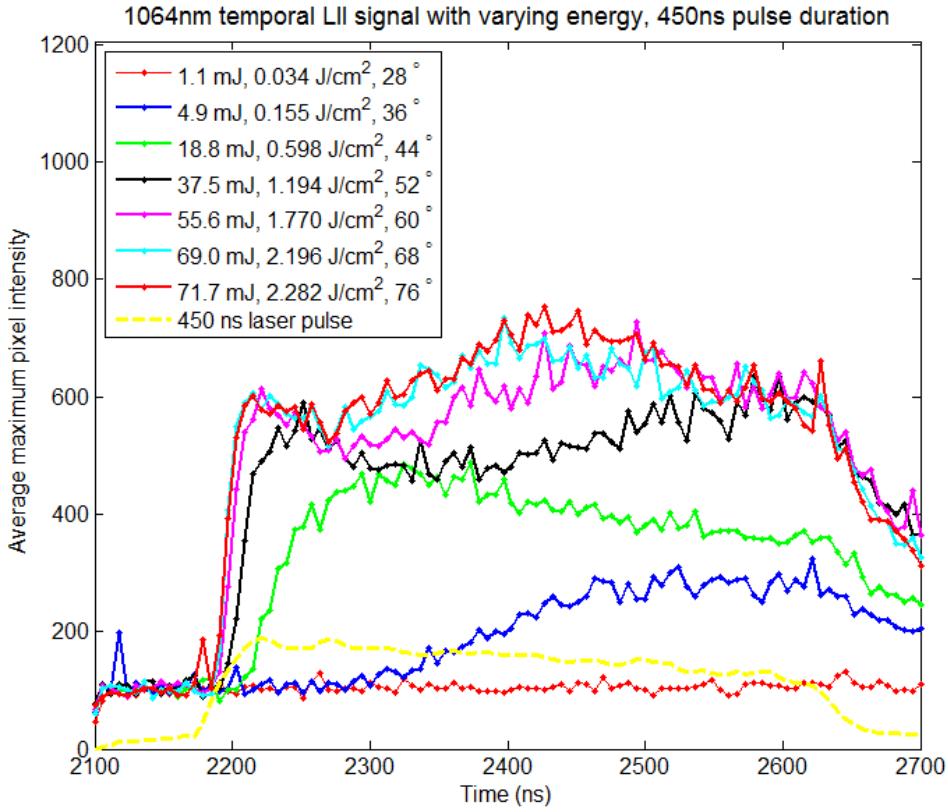

Figure 4.24: Temporal LII signal of the 450 ns pulse duration, with varying pulse fluence. Here every other LII measurement shown.

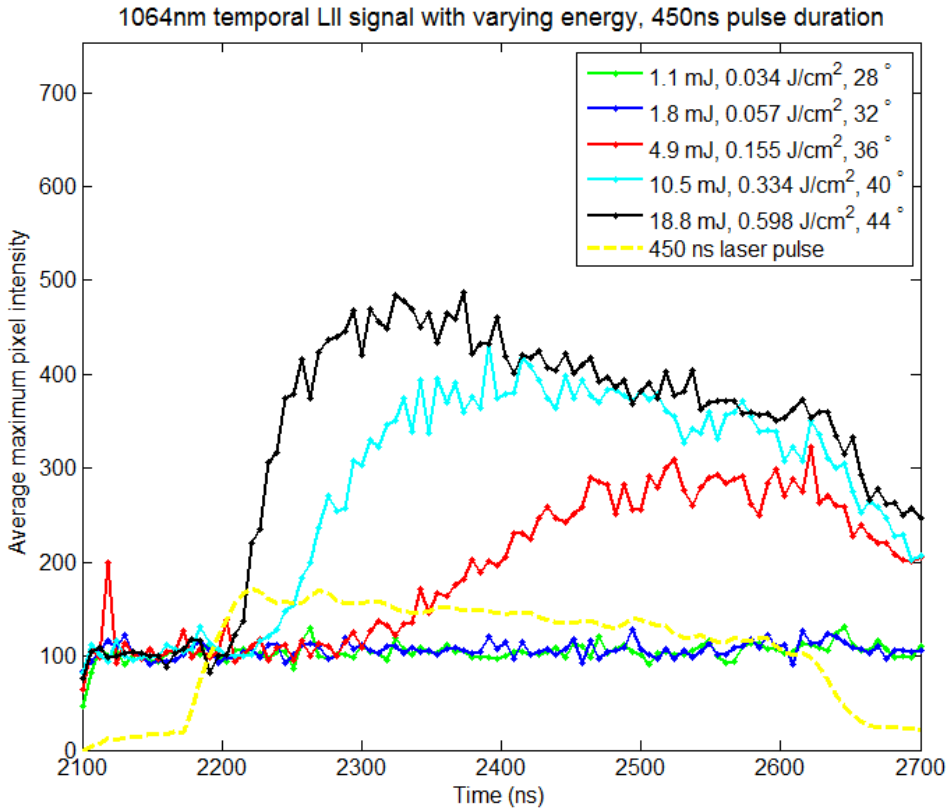

Figure 4.25: Temporal LII signal of the 450 ns pulse duration, with varying pulse fluence. Here LII measurements with low fluence values are shown.

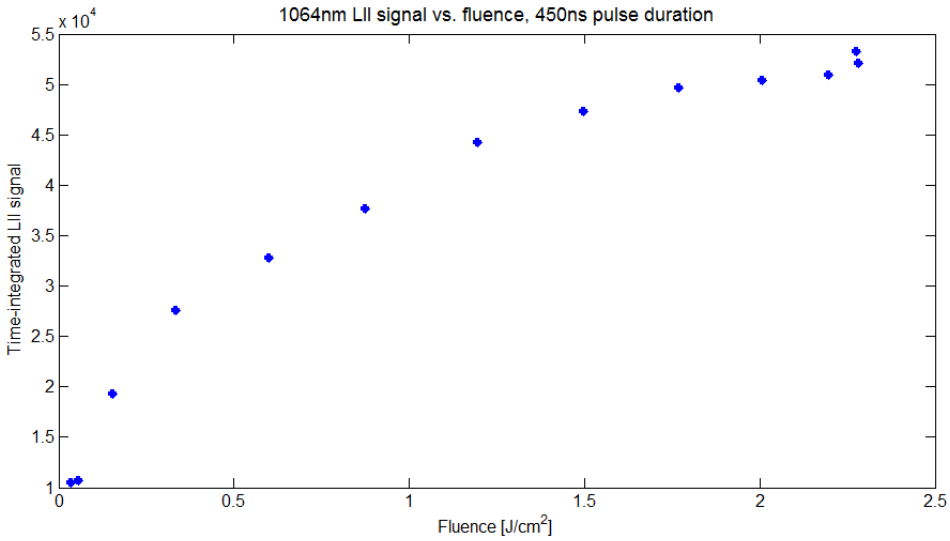

Figure 4.26: Time-integrated LII signal vs. fluence collected using the laser pulse of 450 ns duration. The background noise contribution was removed prior to LII measurements.

4.4.3 100 ns Laser Beam with Varying Fluence

For the 100 ns pulse duration tests, angles [28°, 78°] with 2° increase per LII measurement was chosen. The measured beam energies corresponding to these angles were in the range [0.734, 48.8] mJ. With respect to fluence, this corresponds to a range of [0.023, 1.55] J/cm^2.

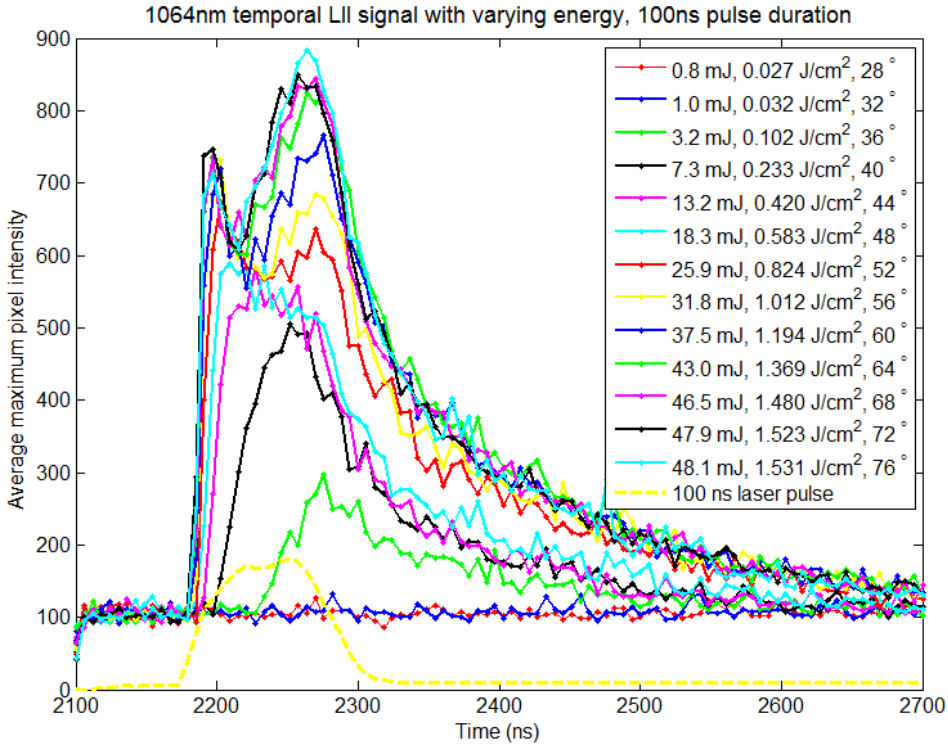

Figure 4.27: Temporal LII signal of the 100 ns pulse duration, with varying pulse fluence. Here every other LII measurement is shown.

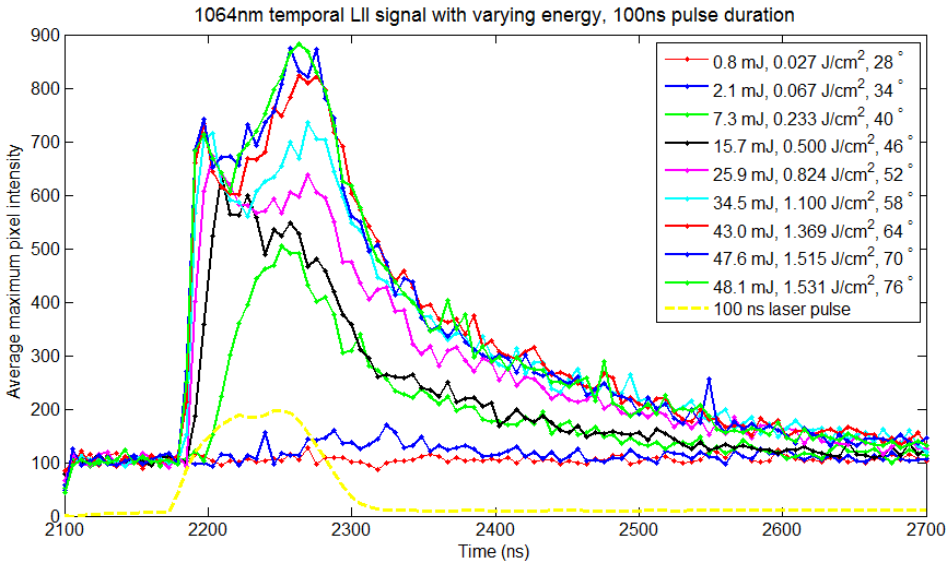

Figure 4.28: Temporal LII signal of the 100 ns pulse duration, with varying pulse fluence. Here every third LII measurement is shown for better visibility.

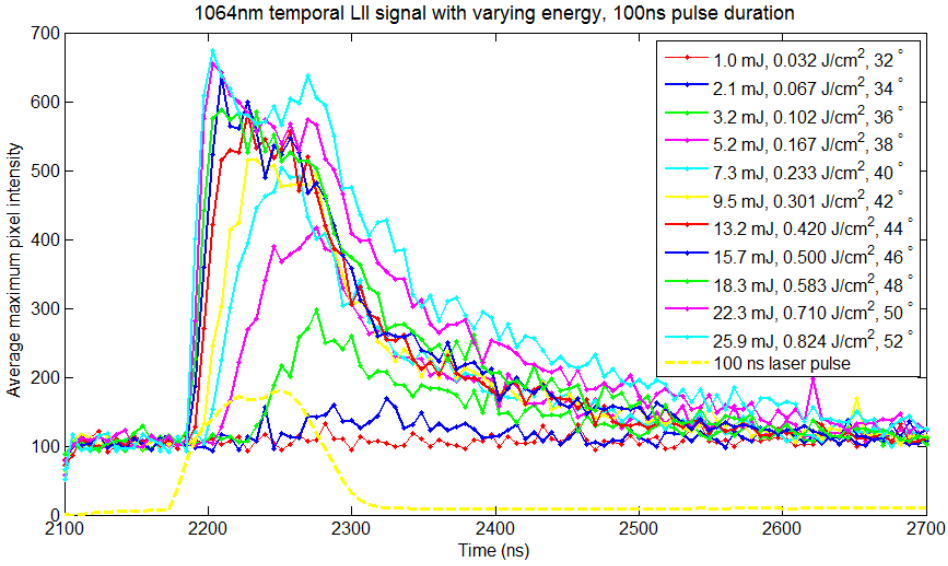

Figure 4.29: Temporal LII signal of the 100 ns pulse duration, with varying pulse fluence. Here LII measurements with low fluence values are shown.

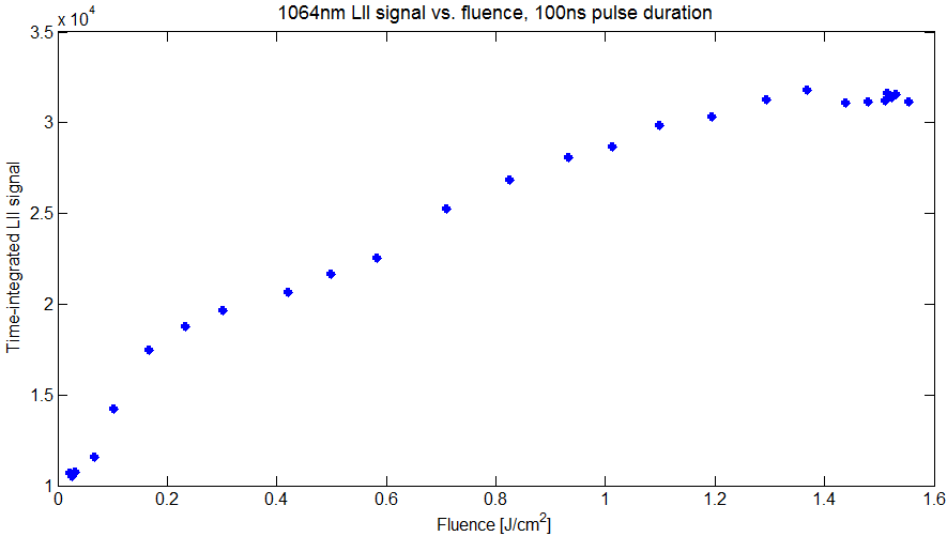

Figure 4.30: Time-integrated LII signal vs. fluence collected using the laser pulse of 100 ns duration. The background contribution was removed prior to LII measurements.

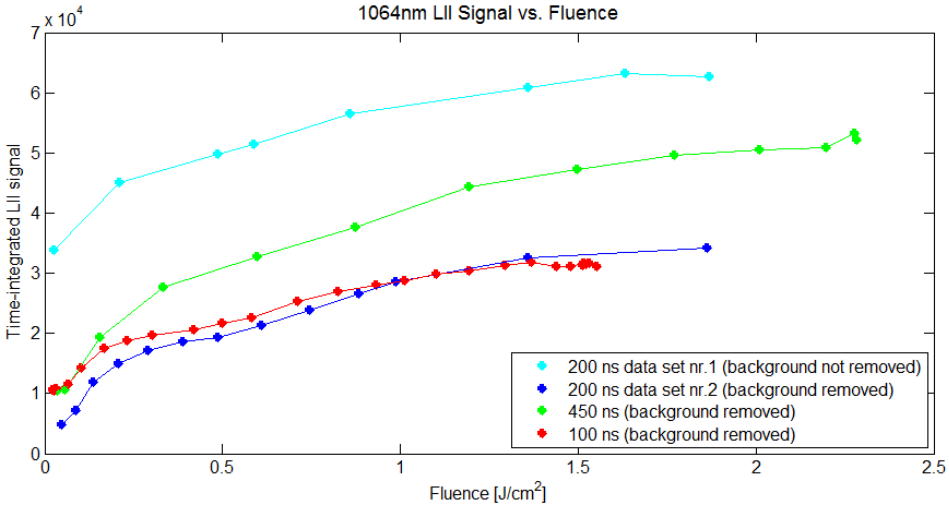

Figure 4.31: Time-integrated LII signal vs. fluence collected using laser pulses of 100, 200 and 450 ns duration. There are two data sets for the 200 ns pulse, one with and one without the background noise removed prior to measurements.

5 Discussion

5.1 Comparison of Results with Previous Experiment at SINTEF

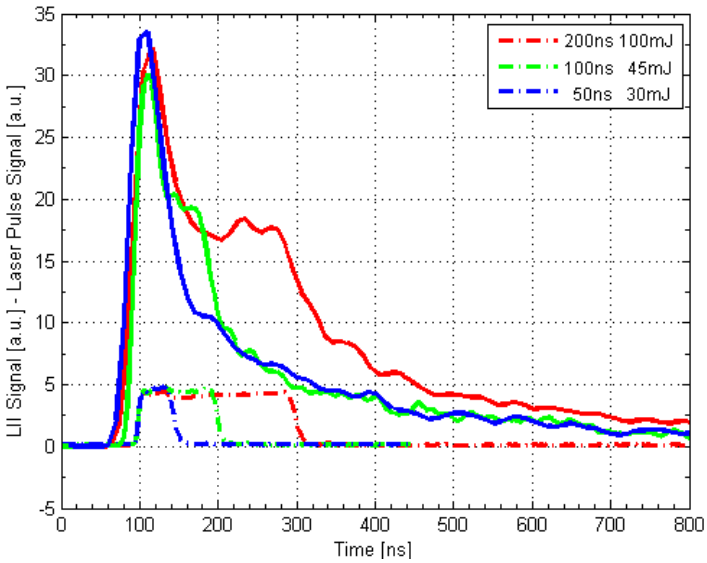

Figure 5.1: Figure 2.14 from previous experiments at SINTEF/NTNU with long pulse duration. The temporal LII signals show the appearance of a second peak for large pulse energies and long pulse durations.

The shape of the temporal LII signal is consistent with the previous results acquired at SINTEF, shown in section 2.5. There is first an initial prompt peak in the temporal LII signal, then a second peak appears after the prompt LII signal has begun to decay. It was also seen that the second peak became stronger when a laser pulse of high energy was used.

Figure 5.1 is also presented in section 2.5. The figure shows how the second peak appears when the laser pulse has a large pulse energy and a long pulse durations. The results found in this project is consistent with these findings.

As mentioned before, when comparing with the previous results at SINTEF, it is important to remember the different experimental setup and camera settings used. The gate width for these experiments is 5 ns instead of 10 ns. In the previous experiments ten images were accumulated on-chip, while only two images are accumulated on-CCD here. Most importantly, the laser beam's spatial profile is very different.

5.2 Y-profile of the Temporal LII Signal

Figure 5.2 is a sketch of what the camera sees, seen from another angle. The camera views the xy-plane as depicted by the shown coordinate system in the sketch. When it looks at the center of laser impact, it will see the intensity along the z-direction. A pixel at y=88 will be a result of the high intensity from the center of the laser and also the edges of the laser in the z-direction. This is shown by the orange circle in the same y-position as the square in the center of the laser beam.

In section 3.2.2 however, the ICCD camera's DOF was found to be 0.39 mm. The pixel's intensity at a certain y-position is a summation of the intensity along the DOF region in the z-direction. Though the DOF is found to be approximately 0.39 mm for the nine pixels, there is still the question of precisely how much the edges of the laser beam in the z-direction contribute to the shape of the temporal LII signal. A study of the y-profile of the temporal LII signal was therefore performed. Along with the temporal LII signal from the center, the signal was studied at y = 88 $\pm$ 39 and y = 88 $\pm$ 15. The fluence at these positions will be much less than the fluence at the center of the beam.

Analysis of the y-profile of the temporal LII signals was of interest for both the 532 nm and the 1064 nm LII measurements. Results are presented for both the 100 ns and 450 ns pulse durations. Together with the temporal LII signal, there is also shown a graph over the x-position found to give maximum intensity along the chosen y-position. As these figures show, the chosen x-value is quite random before the time of laser impact, but during impact and afterwards the x-position of found maximum remains much the same for all the y-positions.

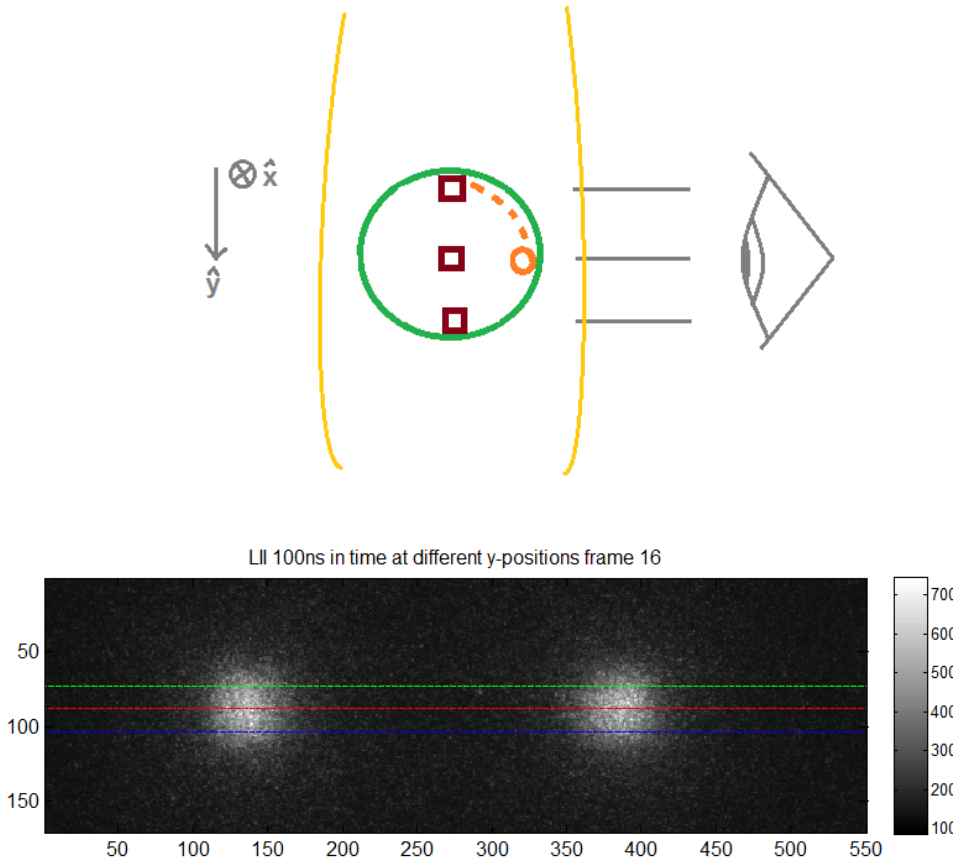

Figure 5.2: The sketch above shows different y-positions along which the ICCD camera finds average maximum intensity. The human eye signifies the position of the camera, seeing the xy-plane. The green circle is the cross-section of the laser passing through the flame (yellow). The image below is an example intensity image captured by the camera for the 1064 nm laser beam of 100 ns duration. The colored lines in the image highlight different y-positions, here $y = 88 \pm 15$ signifying a true width of 0.86 mm.

5.2.1 532 nm LII Experiments

LII signal along y = 88 $\pm$ 39

Figure 4.8 shows the average temporal LII signal for the 100 ns laser pulse along y=88, i.e. near the center of the laser's impact position in the flame. Figure 5.7 shows the average maximum signal at y=88, y=49 and y=127. y= 88 $\pm$ 39 corresponds to 78 pixels or 2.23 mm in real width according to the resolution measurement presented in section 3.2.2. The spatial beam profiles measured the laser beam's beamwidth to be 1.94 mm. A 2.23 mm width means that the temporal LII signal is captured a position slightly outside the $1/e^2$-

width, i.e. captured from the very edges of the laser beam depicted in the images of the beam's spatial profile. The spatial area along y = 88 $\pm$ 15 however, signifies a width of 0.86 mm and lies well within the beam's size.

As can be seen in Figure 5.7, there are striking differences in the shape of the temporal LII signal along the different y-positions. Near the top and bottom, the prominent first peak is not seen. Along the bottom edge, y=127, we see a weaker LII signal and a shape which suggests that vaporization might not have occurred. Along the edges, the peak signal is seen at a later time, about the same time as the second peak of the LII signal along the center y-position.

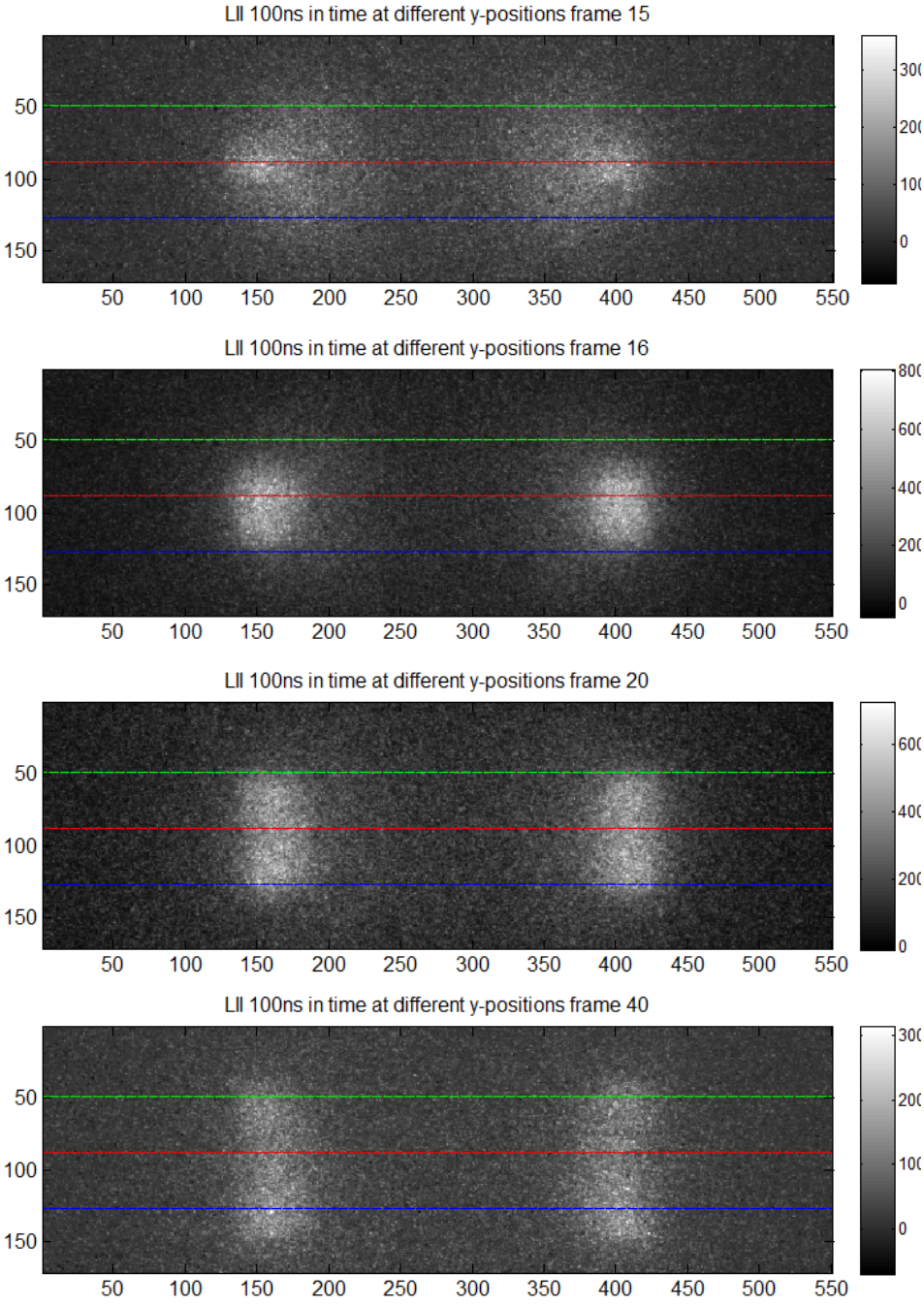

Figure 5.3: LII signal from 532 nm laser pulse of 100 ns duration. Starting with frame #15 of 100, directly after the pulse has reached the flame. The colored lines show three different y-positions; y = {49, 88, 127} = 88 $\pm$ 39.

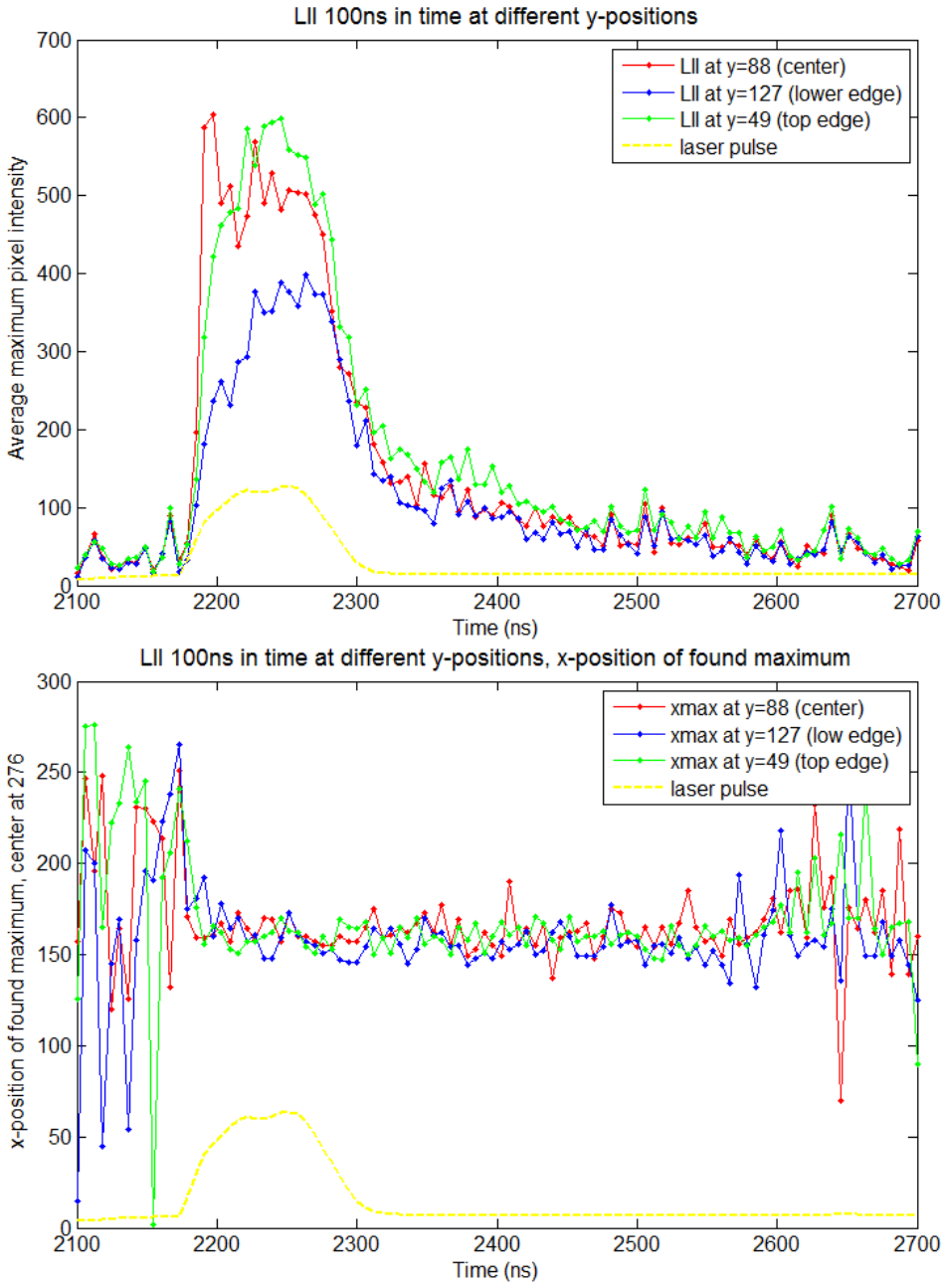

Figure 5.4: 100 ns temporal LII signal along different y-positions in the top graph, using 532 nm laser beam. The bottom graph shows the x-position of found maximum along y=88, y=49 and y=127.

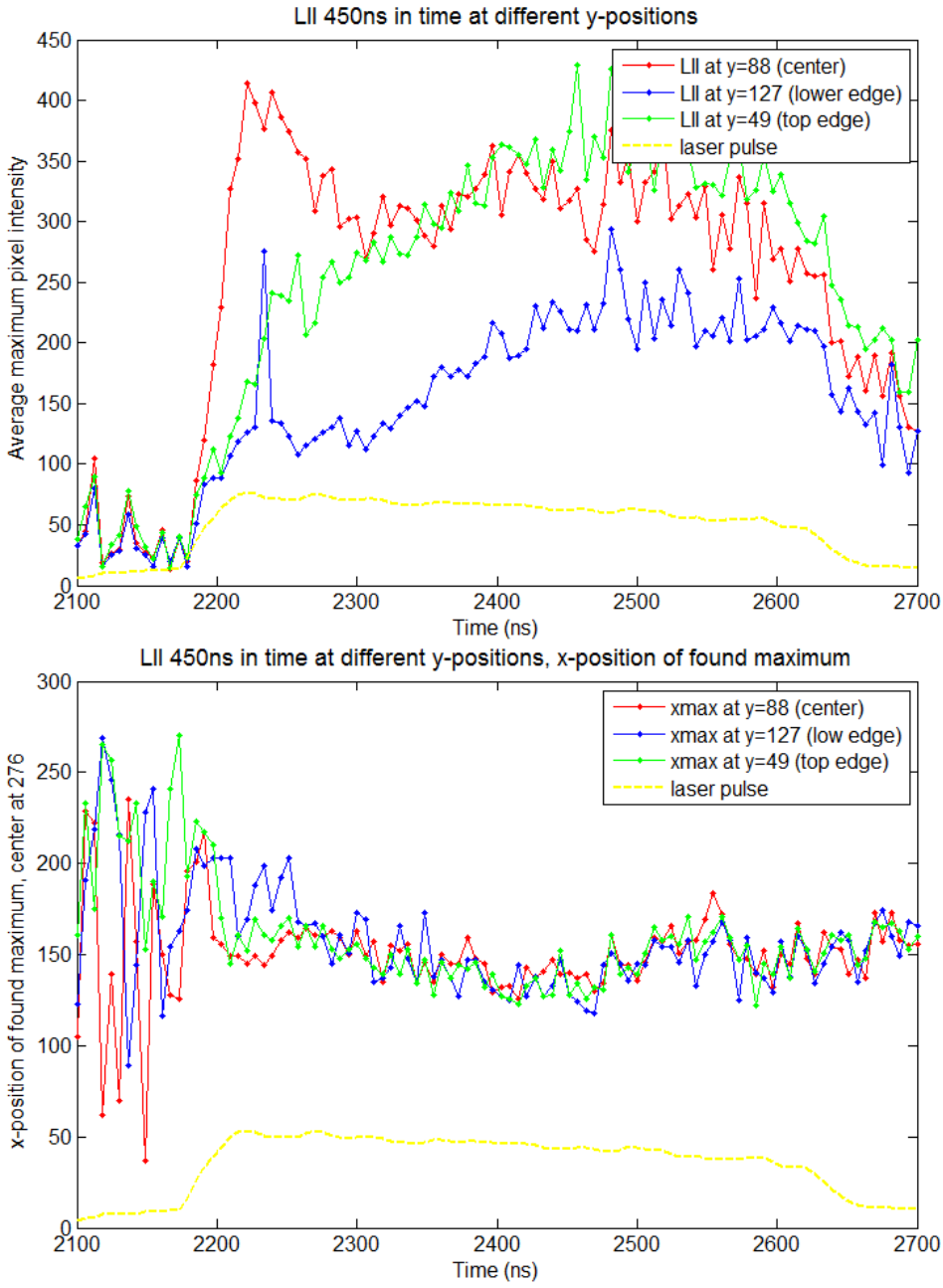

Figure 5.5: 450 ns temporal LII signal along different y-positions in the top graph, using 532 nm laser beam. The bottom graph shows the x-position of found maximum along y=88, y=49 and y=127.

LII signal along y = 88 $\pm$ 15

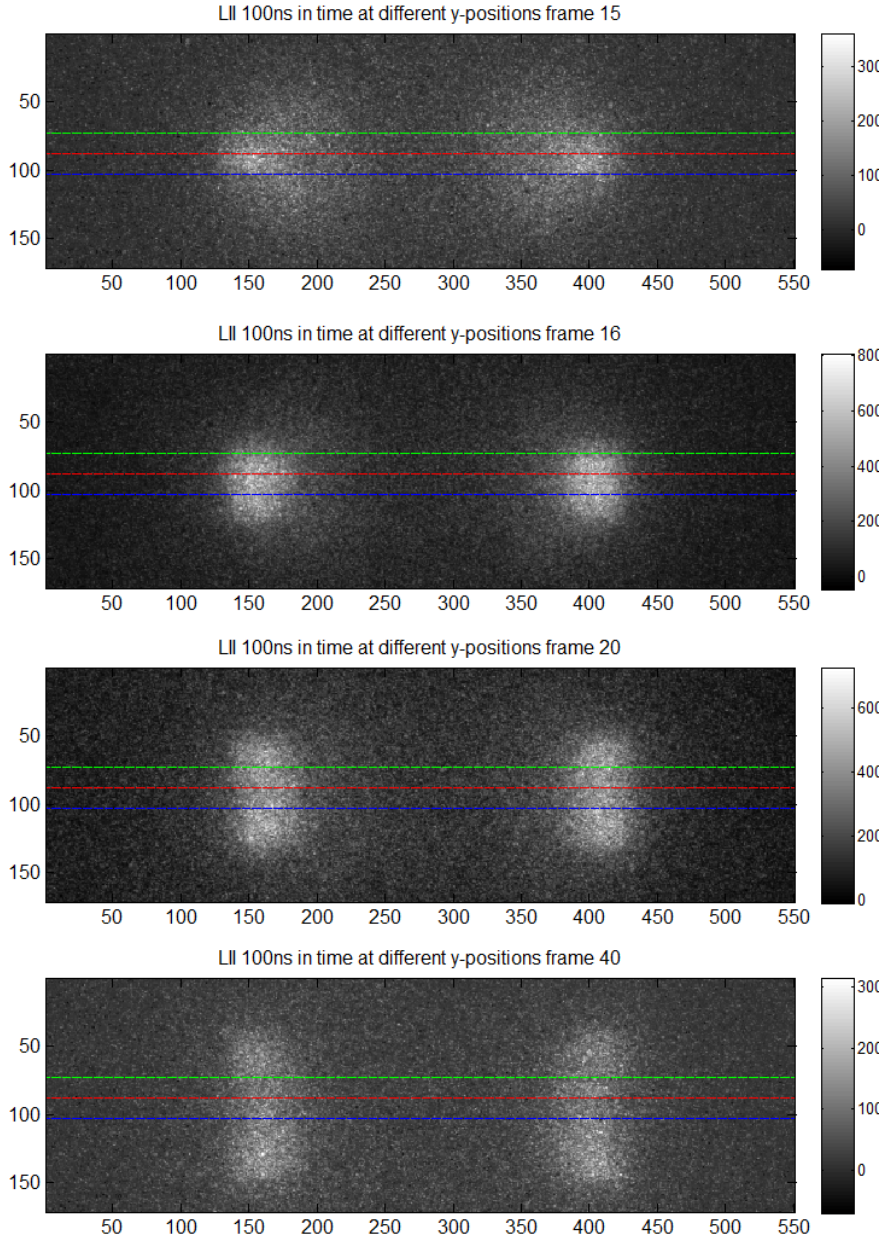

Figure 5.6: LII signal from 532 nm laser pulse of 100 ns duration. Starting with frame #15 of 100, directly after the pulse has reached the flame. The colored lines show three different y-positions; y = 88 $\pm$ 15.

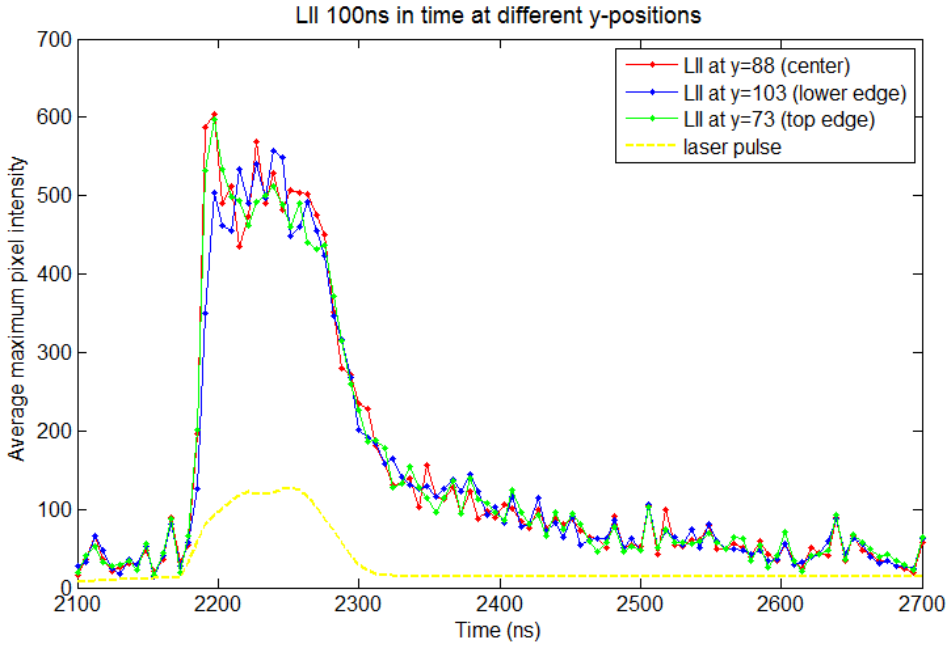

Figure 5.7: 100 ns temporal 532 nm LII signal along different y-positions: y = 88 $\pm$ 15.

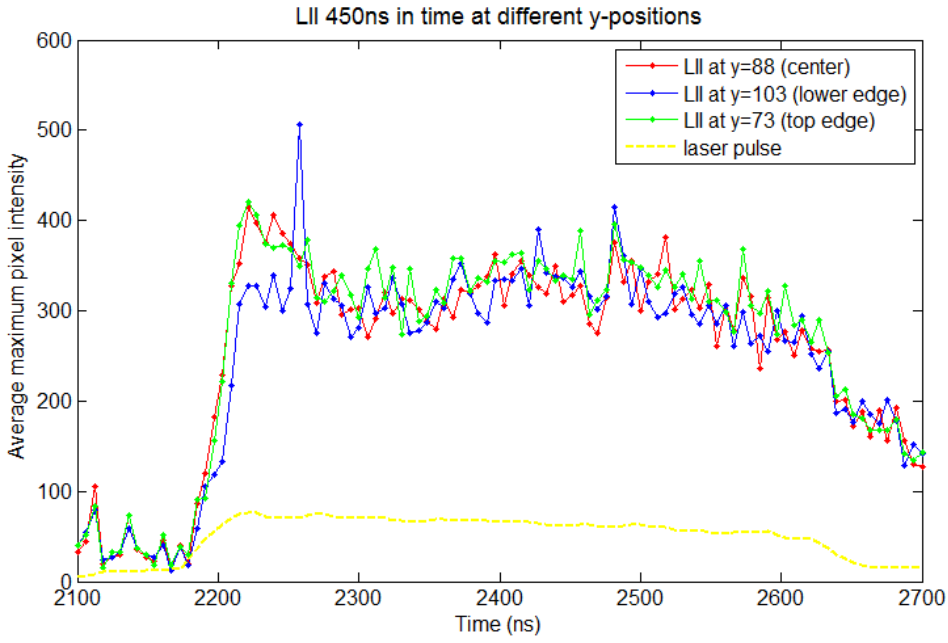

Figure 5.8: 450 ns temporal 532 nm LII signal along different y-positions: y = 88 $\pm$ 15.

5.2.2 1064 nm LII Experiments

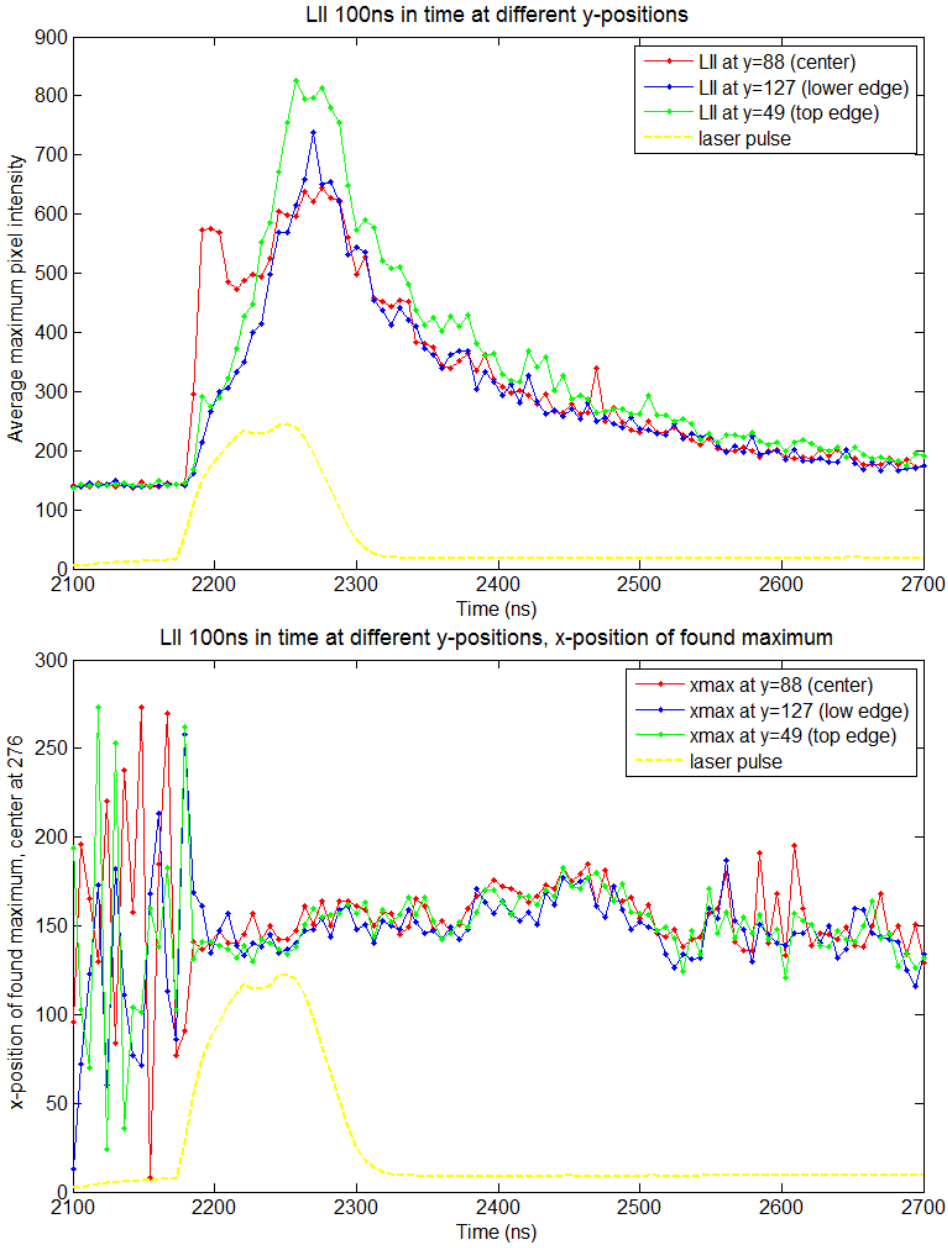

Figure 5.9: 100 ns temporal LII signal along different y-positions in the top graph, using 1064 nm laser beam. The bottom graph shows the x-position of found maximum along y=88, y=49 and y=127 (y = 88 $\pm$ 39).

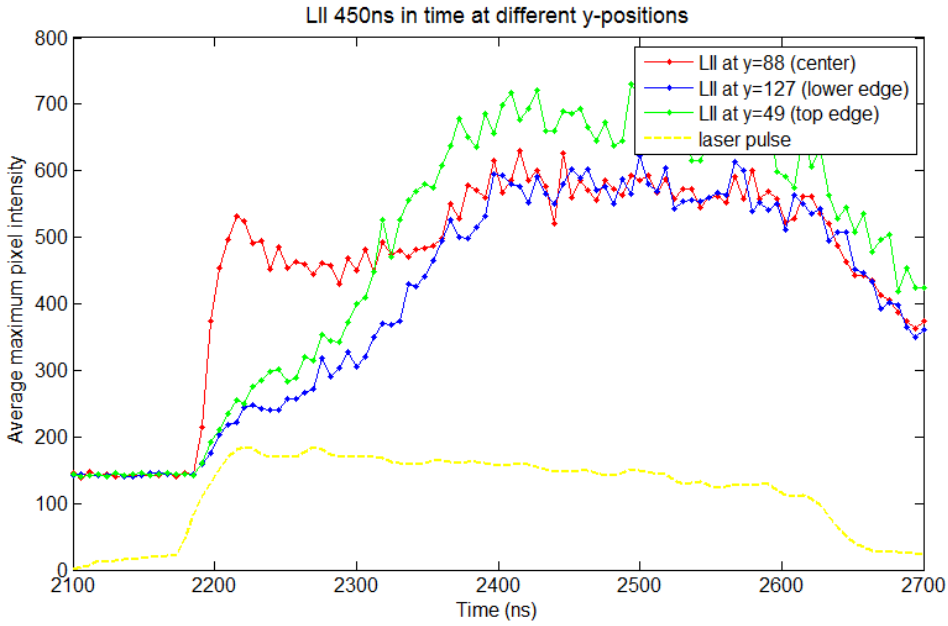

Figure 5.10: 450 ns temporal 1064 nm LII signal along different y-positions: y = 88 $\pm$ 39.

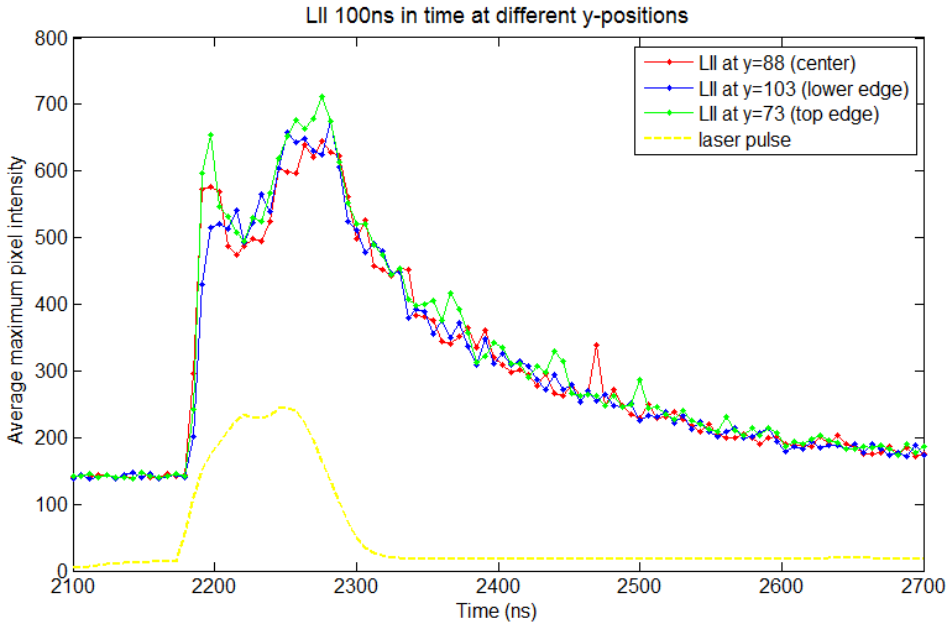

Figure 5.11: 100 ns temporal 1064 nm LII signal along different y-positions: y = 88 $\pm$ 15.

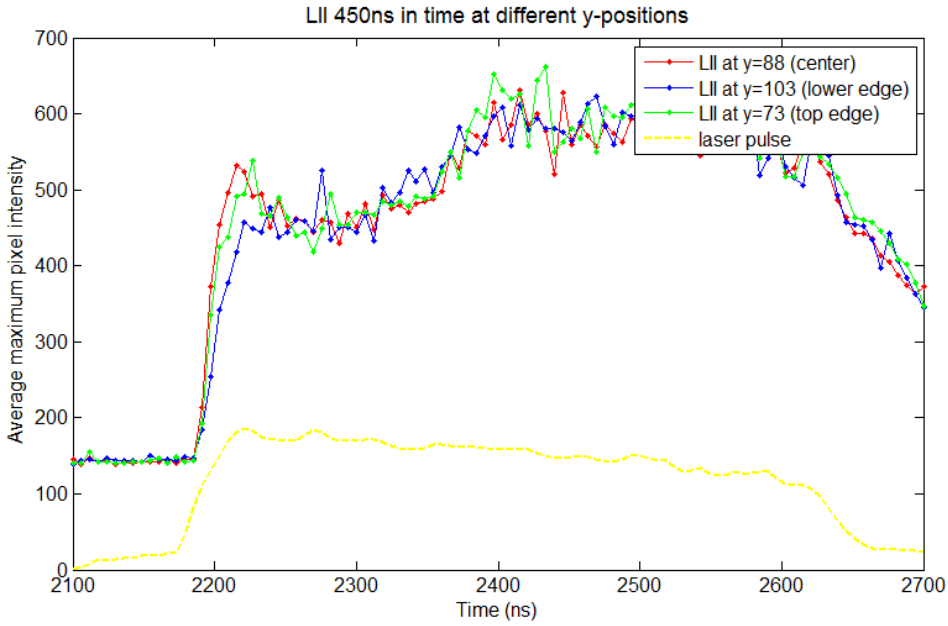

Figure 5.12: 450 ns temporal 1064 nm LII signal along different y-positions: y = 88 $\pm$ 15.

5.3 X-profile of the Temporal LII Signal

Despite the relatively high airflow around the fuel flame, the flame flickers. As mentioned earlier, as long as a certain y-position is chosen and maximum intensity is found along this height, the flickering of the flame isn't of much consequence. Figure 5.7 shows the chosen x-position where maximum intensity was found for each of the 100 images. To be consistent, only the left side of the flame was chosen for analysis, see Figure 3.31. The graph shows how the position of maximum is quite random before the impact of the laser pulse. However, when the laser pulse is present and also quite a long time after, the position of maximum intensity stays around the same x-value, about x $\approx$ 150.

The purpose of analyzing the temporal LII profiles in the x-direction is to study a possible difference in the LII signal between the fuel-rich and the oxygen-rich area of the flame. The temporal LII signal was analyzed as previously shown for the found x-position of maximum intensity signal, defined as x = xmax. At the same time, the intensity for x= xmax $\pm 20, \pm 30$, etc. were recorded. The result is shown in Figure 5.14 for the 100 ns pulse and in Figure 5.15 for the 450 ns pulse. The figures show how the temporal LII signal for the fuel side has higher intensity than the oxygen rich side in the beginning. Some frames later, this difference has evened more out.

In the 532 nm and 1064 nm measurements, the x-profiles of both the 100 ns and 450 ns pulse durations were analyzed. The following results show how the soot builds up slightly differently on the fuel vs. the oxygen-rich side. However, this does not seem to have an effect on the second peak phenomenon. Indeed, the temporal LII signals of the 1064 nm laser beam clearly show the second peak at both the fuel- and oxygen-rich side.

5.3.1 532 nm LII Experiments

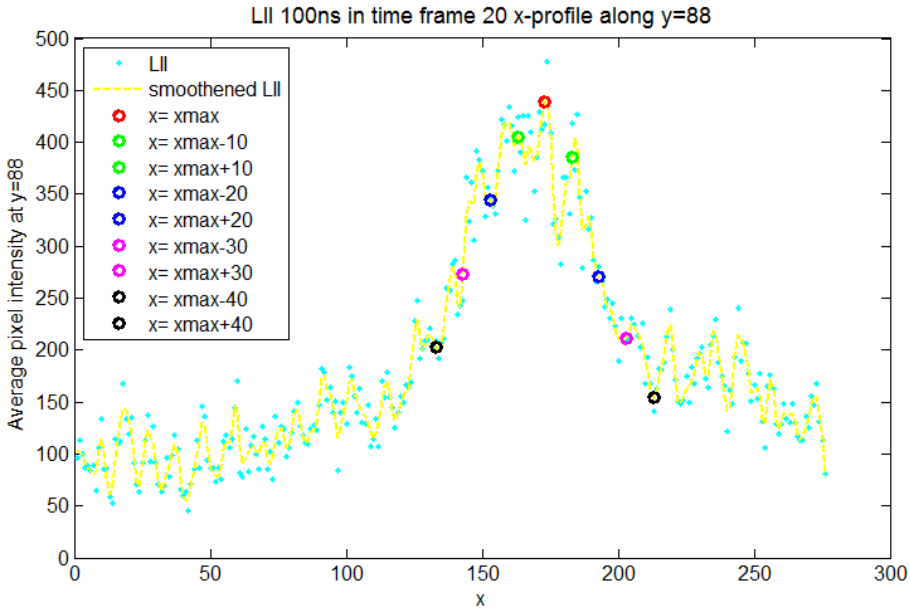

Figure 5.13: X-profile of frame #20 of 100 for the 100 ns pulse duration, using 532 nm laser beam. The x-profile was analyzed for the left side of the flame. In the figure, the fuel-side is thus to the right, i.e. the x-values greater than xmax.

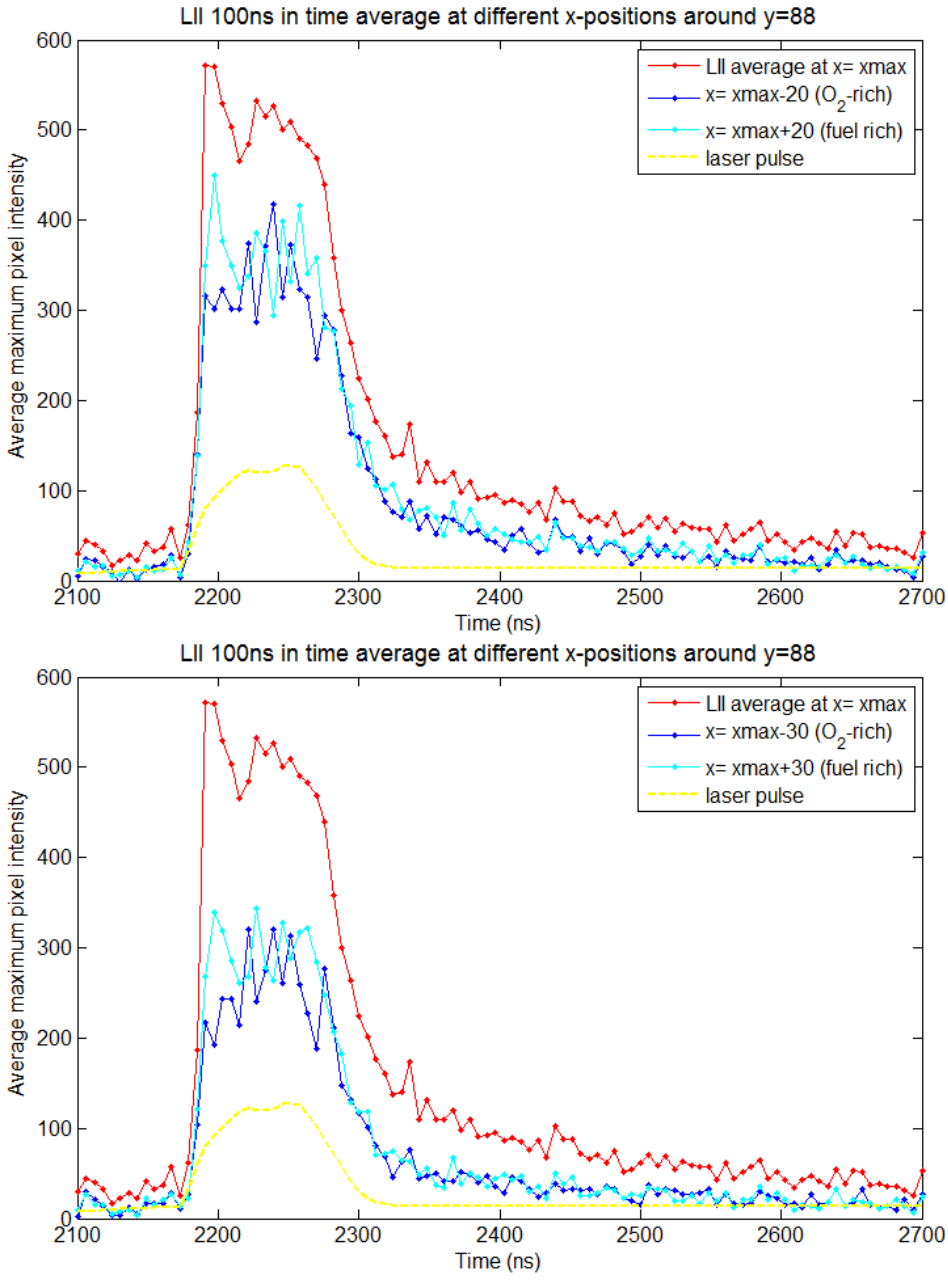

Figure 5.14: Temporal LII signal for the 100 ns pulse duration, using 532 nm laser beam. The temporal profiles of both the O_2-rich and the fuel rich side are shown.

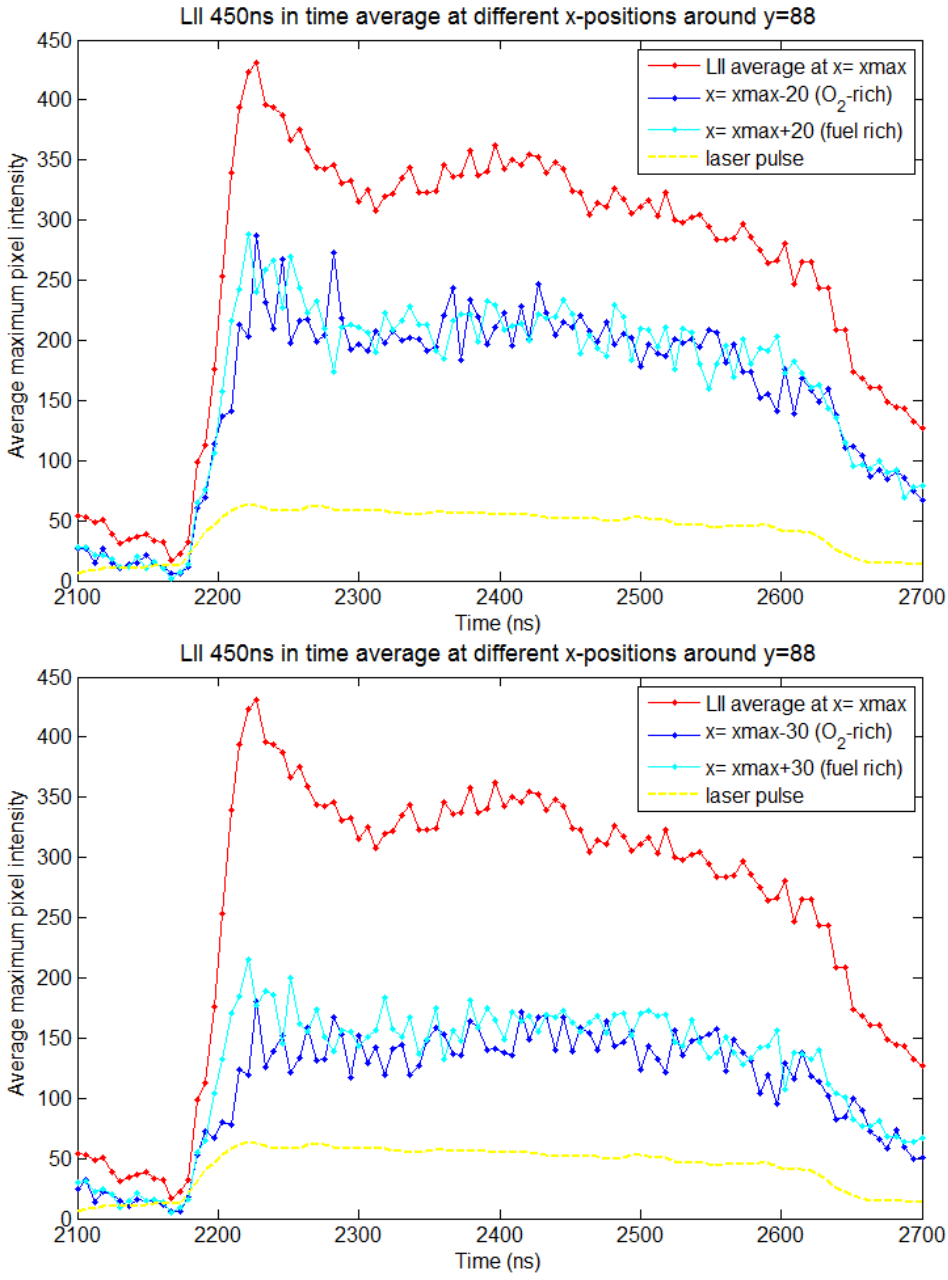

Figure 5.15: Temporal LII signal for the 450 ns pulse duration, using 532 nm laser beam. The temporal profiles of both the O_2-rich and the fuel rich side are shown.

5.3.2 1064 nm LII Experiments

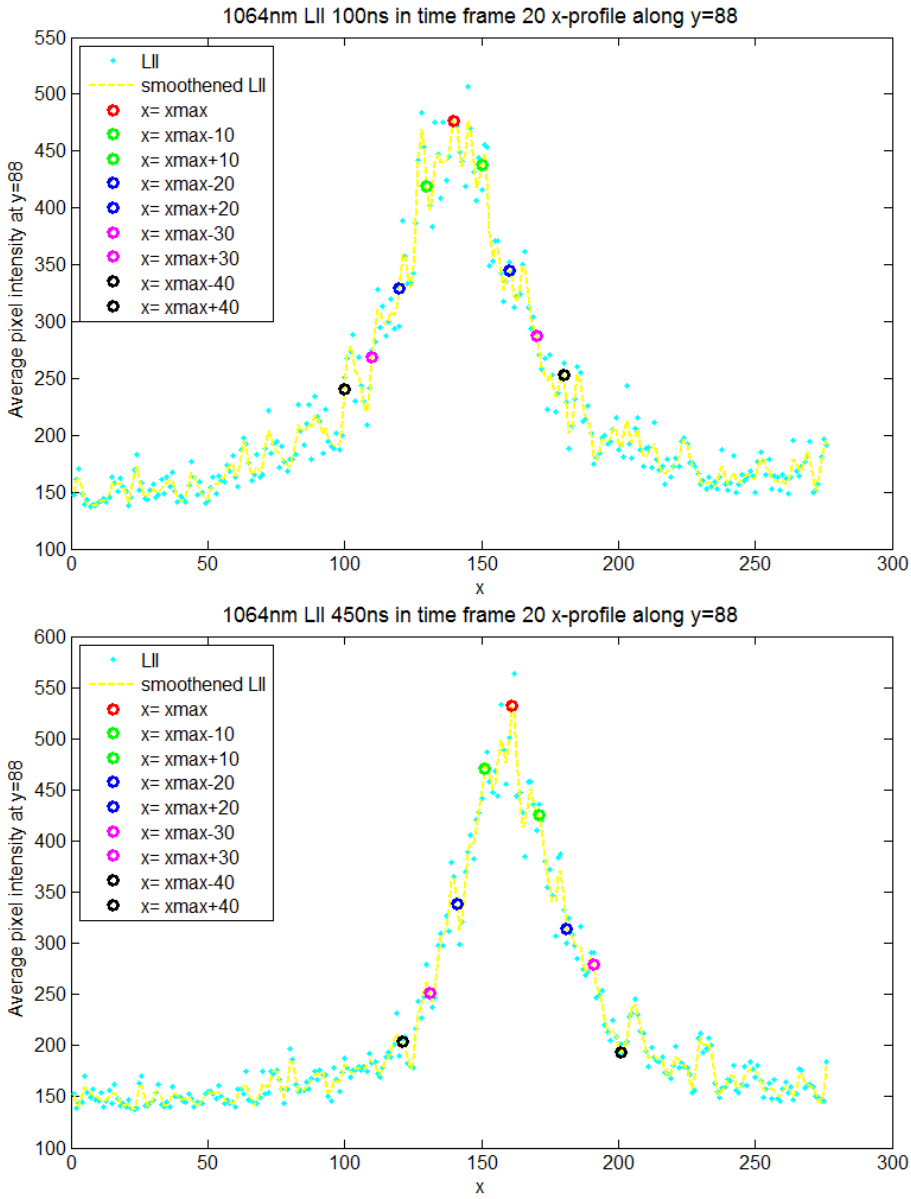

Figure 5.16: X-profile of frame #20 of 100 for the 100 ns pulse(top) and the 450 ns pulse(below). The x-profile was analyzed for the left side of the flame. In the figure, the fuel-side is to the right.

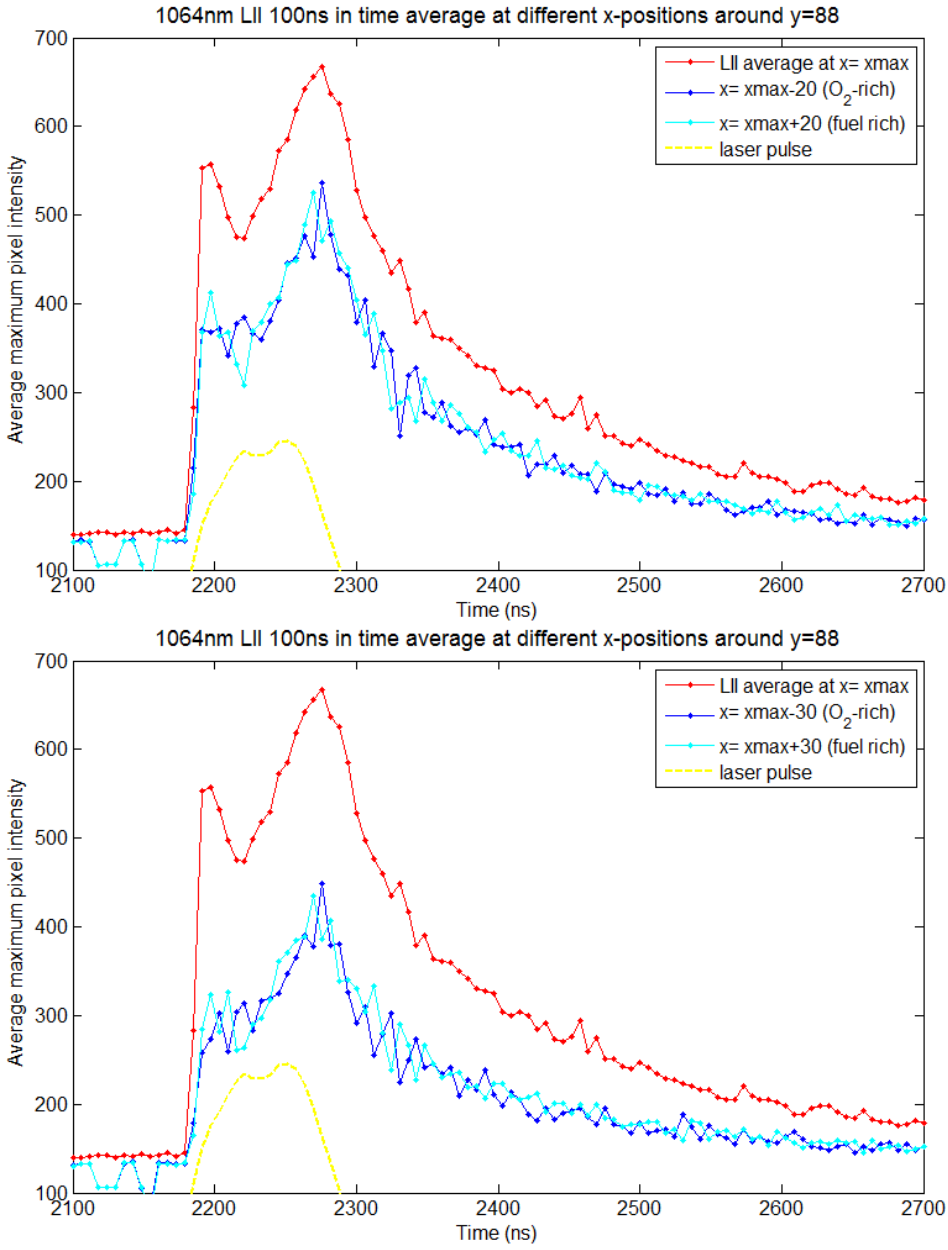

Figure 5.17: Temporal LII signal for the 100 ns pulse duration, using 1064 nm laser beam. The temporal profiles of both the O_2-rich and the fuel rich side are shown.

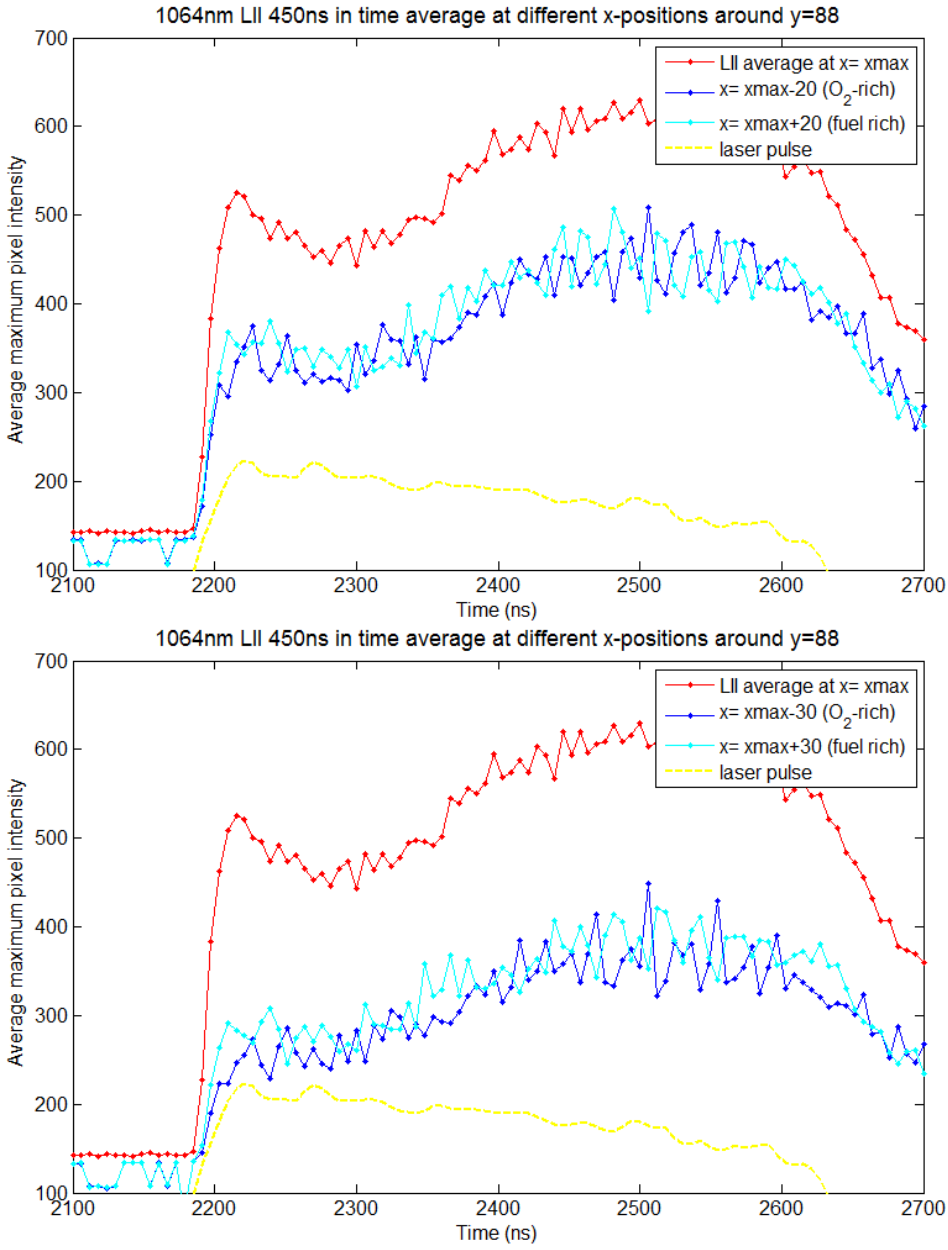

Figure 5.18: Temporal LII signal for the 450 ns pulse duration, using 1064 nm laser beam. The temporal profiles of both the O_2-rich and the fuel rich side are shown.

5.4 The Second Peak Phenomenon

5.4.1 Fluence Dependence

The results in section 4.4 show how the appearance of the second peak in the LII signal is dependent on the fluence of the laser pulse used. The results also showed that the laser pulses with low fluence have an LII signal which starts much later in time than that for the high fluence pulses. When the pulse energy is low, the energy distributed to the soot particles uses more time to build-up the amount of energy needed to create induced incandescence.

Interestingly, as long as the laser pulse fluence is above a certain threshold, the second peak is seen at the same position in time. This suggests that the phenomenon is not dependent on the amount of energy absorbed. Its position is however dependent on the laser pulse duration.

Further study of the results presented in section 4.4 revealed another interesting aspect. Defining a starting position in time of the second peak, the accumulated fluence from the laser beam up to that time was calculated. By finding an approximate starting time for several average fluence energies for each of the three pulse durations, several accumulated fluence values were calculated. Interestingly, these calculations show a threshold value for accumulated fluence around 0.4-0.5 J/cm^2 for the temporal LII signal to have two peaks. As an example, the 100 ns pulse of average pulse fluence of 0.824 J/cm^2 (52°) has an approximate start time of the second peak 55 ns after laser impact. The accumulated fluence in this time interval is thus 0.824 J/cm^2 x (55 ns/100 ns) = 0.45 J/cm^2 . The 0.4-0.5 J/cm^2 fluence area is the threshold value area for vaporization to occur when using a 1064 nm laser beam.

From the graphs over time-integrated LII signal vs. fluence, another question arises. This method should according to previous studies, reveal a signal that increases rapidly until it begins to saturate around 0.4-0.5 J/cm^2. However, the LII measurements show a different result when using a long pulse duration. The time-integrated signal does indeed increase rapidly up to about 0.4 J/cm^2, when it appears to begin to saturate. However, in direct contrast to previous studies, the signal begins to increase again.

Because of these findings, the time-integrated LII signal vs. fluence was analyzed for different time intervals. The LII signal was first time-integrated within the time of the first peak, and then time-integrated within the time of the second peak. From the results shown in Figures 5.19-5.21, we see that the non-lasting saturation happening around 0.4-0.5 J/cm^2 is even more prominent when only the the second peak's time frame is analyzed.

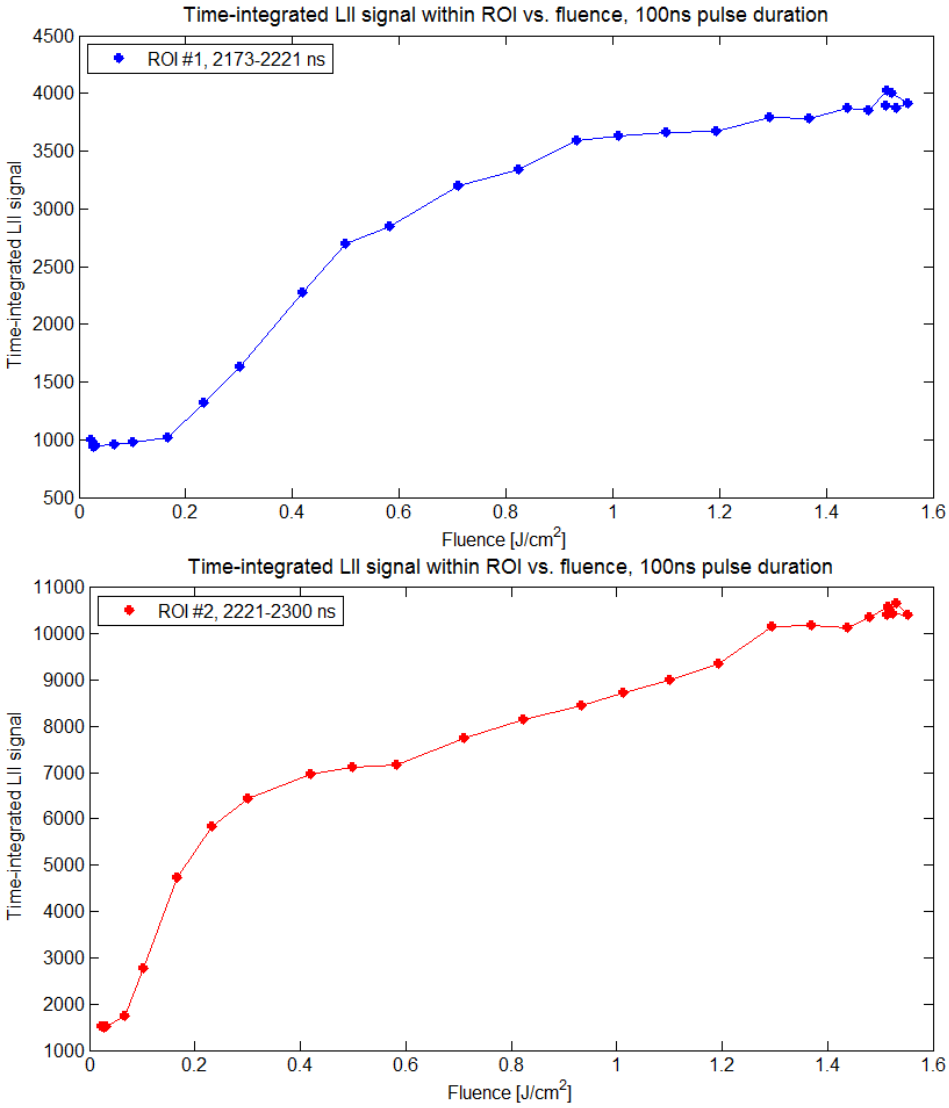

Figure 5.19: Time-integrated LII signal vs. fluence for the 100 ns pulse duration, using the 1064 nm laser beam. The top graph is the time-integrated LII signal during the time frame of the first peak, and the bottom graph shows the results when time-integrated over the time frame of the second peak. The time-integrated LII signal vs. fluence during the full time frame 2100-2700 ns is presented in Figure 4.30.

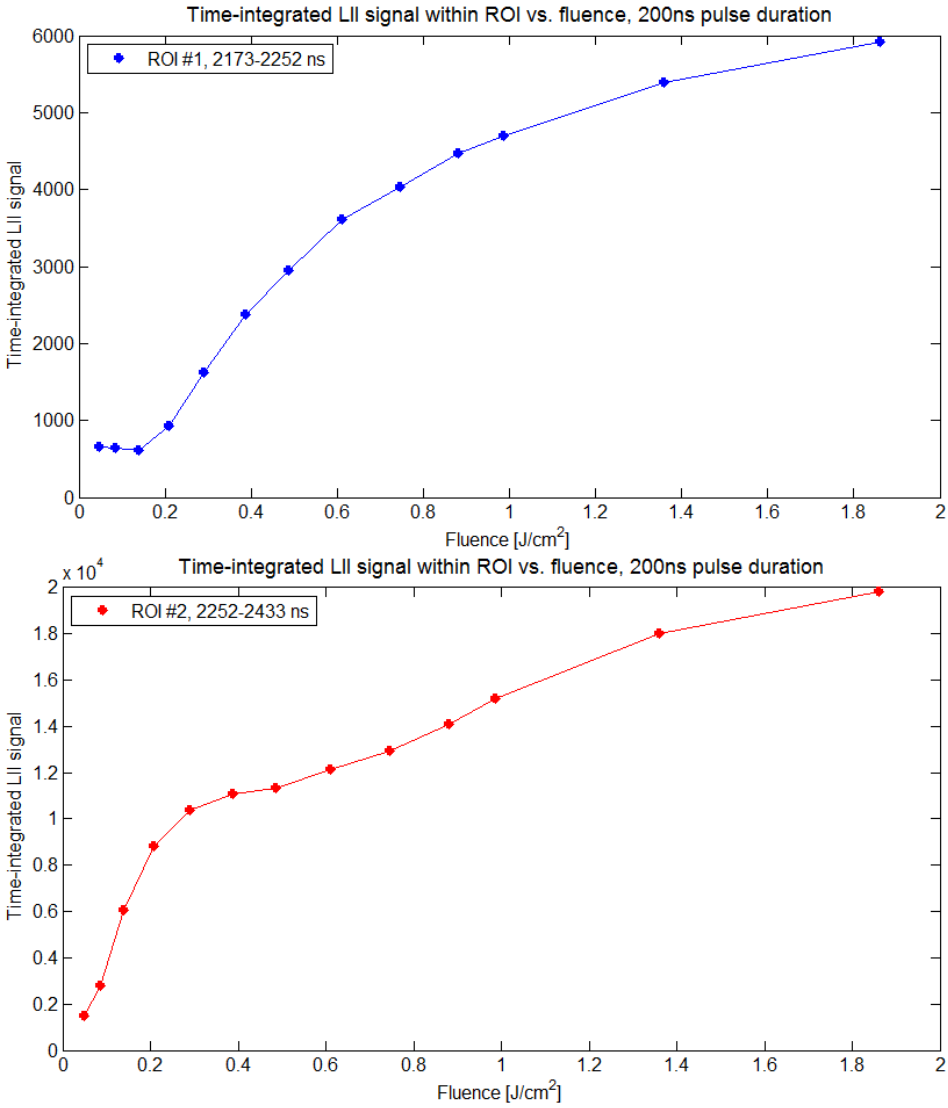

Figure 5.20: Time-integrated LII signal vs. fluence for the 200 ns pulse duration, using the 1064 nm laser beam. The top graph is the time-integrated LII signal during the time frame of the first peak, and the bottom graph shows the results when time-integrated over the time frame of the second peak. The time-integrated LII signal vs. fluence during the full time frame 2100-2700 ns is presented in Figure 4.23.

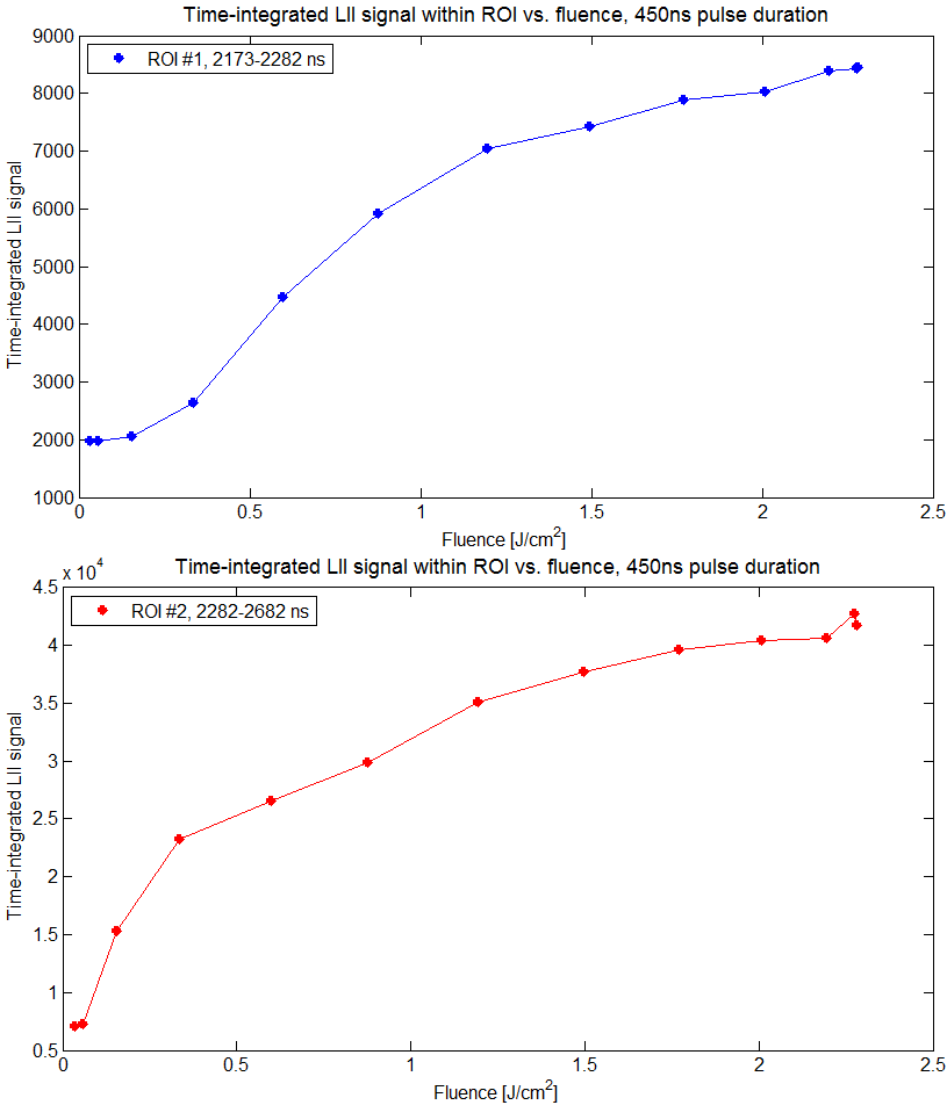

Figure 5.21: Time-integrated LII signal vs. fluence for the 450 ns pulse duration, using the 1064 nm laser beam. The top graph is the time-integrated LII signal during the time frame of the first peak, and the bottom graph shows the results when time-integrated over the time frame of the second peak. The time-integrated LII signal vs. fluence during the full time frame 2100-2700 ns is presented in Figure 4.26.

From the figures presented in section 4.4, the first temporal curve to have a clearly visible double peak can be approximately decided upon for each pulse duration. The corresponding fluence values of these signals are highlighted in Figure 5.22. For the 100 ns pulse, the first peak begins to take shape in the signal corresponding to average pulse fluence of 0.500 J/cm^2 (46°) and irradiance 5.00 MW/cm^2. The two peaks are both present in the LII signal corresponding to average pulse fluence of 0.824 J/cm^2 (52°) and irradiance 8.24 MW/cm^2.

Likewise for the 200 ns pulse, the first peak begins to take shape in the signal corresponding to average pulse fluence of 0.388 J/cm^2 (16°) and irradiance 1.94 MW/cm^2. The two peaks are both present in the LII signal corresponding to average pulse fluence of 0.745 J/cm^2 (10°) and irradiance 3.725 MW/cm^2. For the 450 ns pulse, the first peak begins to take shape in the signal corresponding to average pulse fluence of 0.598 J/cm^2 (44°) and irradiance 1.329 MW/cm^2. The two peaks are both present in the LII signal corresponding to average pulse fluence of 1.194 J/cm^2 (52°) and irradiance 2.653 MW/cm^2.

Figure 5.22 shows that the first peak begins to become visible after the area of slight saturation in the LII signal vs. fluence. This indicates a threshold value for the double peak phenomenon to occur. Figure 5.23 is the corresponding figure showing LII signal vs. irradiance instead of fluence.

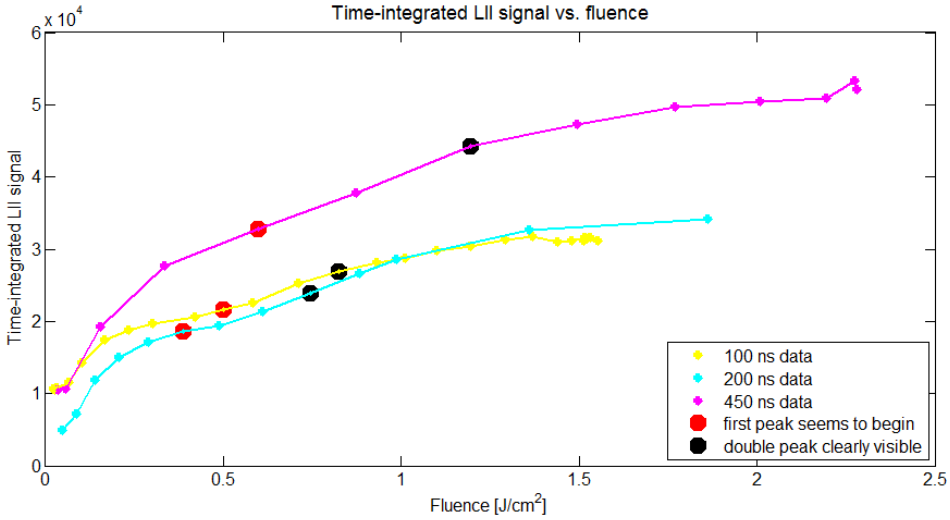

Figure 5.22: Time-integrated LII signal vs. fluence for the three pulse durations. The fluence values of when the first peak begins to become visible and the fluence values when the two peaks are clearly visible are distinguished by red and black dots. The position of the red dots is interestingly right after the slight saturation seen in the signal, in other words just at the beginning of the new increase.

From the figures presented in this thesis, a question arises as to which peak is actually the usual prompt LII peak when doing LII measurements with laser pulses of 7 - 10 ns duration. With such short pulses, it would not be possible to distinguish whether two peaks are in fact present in the temporal LII signal. The results in section 4.4 using low fluence values show how it is the second peak which seems to grow with increasing fluence. It might therefore be possible that it is the appearance of a first peak that is the unknown phenomenon, while the second peak is the original temporal LII signal.

The slight saturation in the 0.4-0.5 J/cm^2 fluence range in the graph from the second peak's time frame shows that the second peak is connected with the initial vaporization of the soot particles. The reason for the sudden appearance of an initial first peak in the temporal LII signal is still unknown, as is the reason behind the further increase in the graphs over the time-integrated LII signal vs. fluence after the 0.4-0.5 J/cm^2 fluence range.

5.4.2 Irradiance Dependence

Figure 5.23 shows the time-integrated LII signal vs. irradiance for the three pulse durations. In the figure, the red and black dots represent the irradiance values of when the first peak begins to become visible and when the double peak is clearly visible in the temporal LII signals.

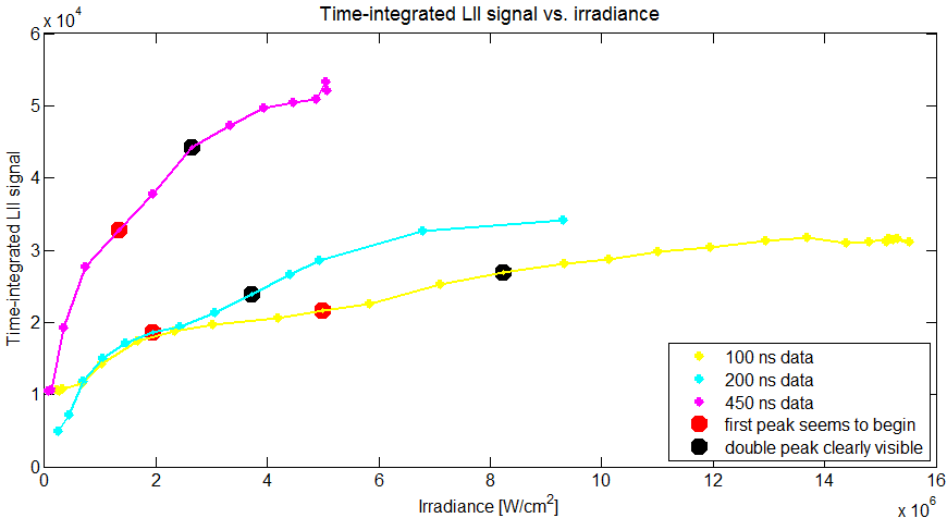

Figure 5.23: Time-integrated LII signal vs. irradiance for the three pulse durations. The irradiance values of when the first peak begins to become visible and the irradiance values when the two peaks are clearly visible are distinguished by red and black dots. As seen in Figure 5.22, the position of the red dots is right after the slight saturation seen in the signal, just at the beginning of the new increase.

Time-integrated LII signal vs. irradiance was studied in the hope of distinguishing whether the double peak phenomenon is dependent on pulse duration. Figure 5.24 shows the time-integrated LII signal vs. fluence for the three pulse durations; 100 ns, 200 ns and 450 ns.

Figure 5.25 shows the time-integrated LII signal vs. irradiance with data points of approximately the same fluence values are highlighted for the three pulse durations. If the dashed lines between these data points had been horizontal, the double peak phenomenon would be independent of pulse duration. The data points of the 100 ns and 200 ns pulses seem to be horizontal, but the 450 ns data points are definitely not horizontal with the other two points. However, since the fluence values of the data points are not exactly the same value and only three different pulse durations were analyzed, further study is needed to determine if the double peak phenomenon is dependent on pulse duration or not. Unfortunately, time was a limiting factor in this project.

LII measurements with even more detailed fluence values is thus advised for all the pulse durations in the range 50 - 450 ns. If the corresponding lines between these data points turns out to be horizontal in the figure over time-integrated LII signal vs. irradiance, the double peak phenomenon can be said to be independent of pulse duration. Such a result would indicate that the LII signals when using a 7 - 10 ns pulse actually has two peaks, though it might not be distinguishable in the temporal signal due to the short time frame.

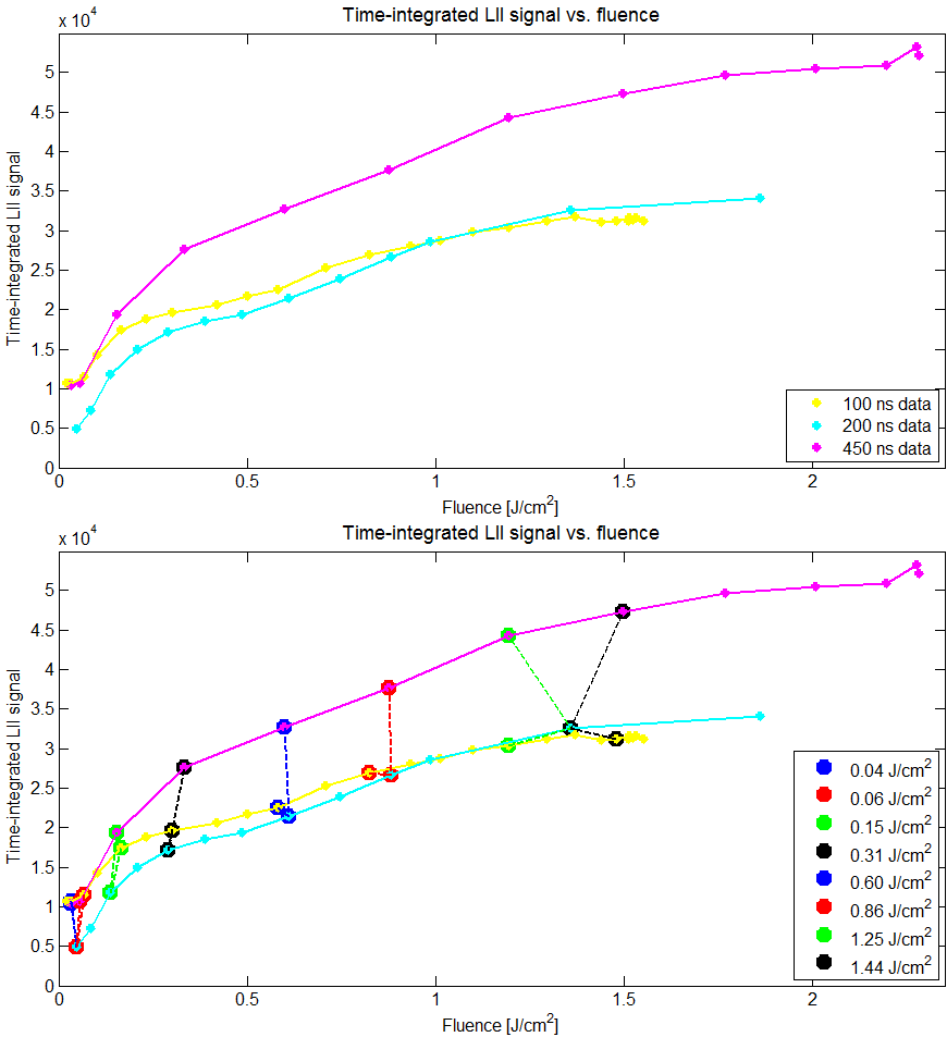

Figure 5.24: Time-integrated LII signal vs. fluence for the three pulse durations; 100 ns, 200 ns and 450 ns. In the bottom graph, data points with approximately the same fluence values are shown. The average fluence for the three data points is shown in the legend. The data points are the ones that are highlighted in Figure 5.25 over the time-integrated LII signal vs. irradiance.

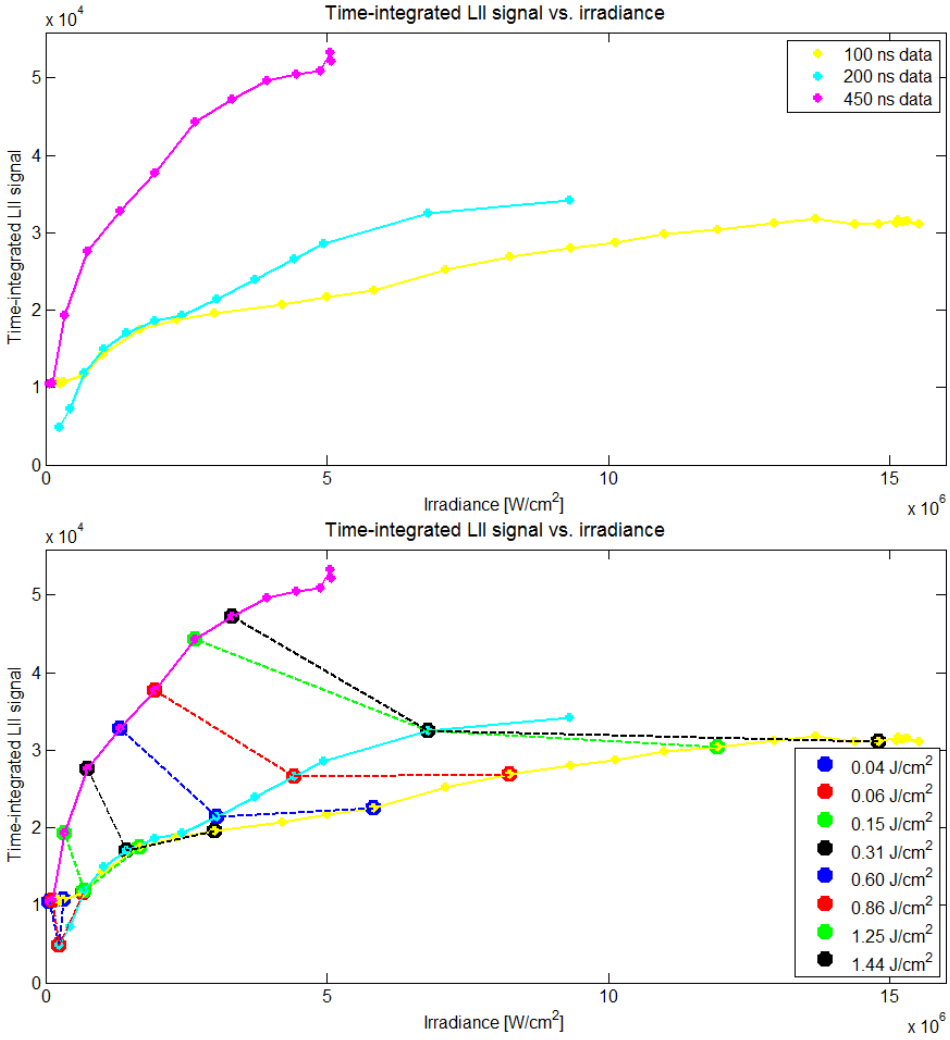

Figure 5.25: Time-integrated LII signal vs. irradiance. In the bottom graph, data points with approximately the same fluence values are shown, with dashed lines between the three data points. The average fluence for the three data points is shown in the legend. The data points are the ones that are highlighted in Figure 5.24 over the time-integrated LII signal vs.fluence. If the dashed lines had been horizontal, the double peak phenomenon would be independent of pulse duration.

5.4.3 Possible Causes

Contribution from Low-energy Parts of the Beam

Figures 5.7 and 5.8 show that the temporal LII signal from the beam wings increases more slowly than the signal from the center. As seen in the figures, the peak of the signal from the wings coincides with the position of the second peak in the signal from the center of laser impact. With respect to the temporal LII signals with varying fluence, this is similar with the signals obtained when using low laser pulse energy.

Nine pixels corresponds to a DOF length of 0.39 mm, as found in section 3.2.2. Compared to a 2 mm wide laser beam, such a width is small. The maximum intensity signal collected by the nine pixels should therefore mostly get its contribution from the center of the beam.

It might seem the low-energy beam wings can be a possible cause of the second peak phenomenon, especially with the figures presented in section 5.2. If the calculated DOF is in fact not entirely correct and the low-energy beam wings do have a significant contribution in the LII signal collected by the ICCD camera's nine pixels, the rest of the spatial beam profile's Gaussian intensity distribution must also have a contribution and be taken into account.

The resulting temporal LII signal would then be a signal with contribution from the whole energy range of the laser beam's spatial distribution. As the temporal LII signals with varying fluence show, increasing the laser pulse's fluence results in a decreasing amount of time between laser pulse impact and the start of LII signal. If the whole beam has a contribution in the LII signal collected by the ICCD camera, the resulting LII signal should not have the second peak phenomenon present. The second peak must therefore be due to something else than a possible wider DOF.

Despite the above, further study is advised with respect to the camera's DOF. Two scenarios to study the spatial contribution in the LII signal collected by the ICCD camera will now be briefly presented. In between the flame and the camera, there is today only one collection lens, see Figure 3.1. The introduction of another lens will make it possible to shift the focus position inside the flame without changing the position of the camera. The two lenses can be set up so that in between them, the light will be collimated. The distance between the lenses can thus be changed without affecting the signal collected by the camera. One of the lenses will focus the collected light towards the ICCD camera. The focus point of the other lens will be inside the flame, but this focus point can be moved by moving the lens. It will then be possible to obtain a series of LII measurements throughout the flame.

Another scenario is to use an incandescent lamp at the position of the nozzle exit. With the setup kept the same, the emitted light from the lamp will be imaged by the camera. The lamp can then be moved slightly towards or away from the camera. It will then be possible

to study how much intensity the camera is able to collect when the lamp is for example 1.5 mm away from the center of the nozzle exit. A graph over the intensity registered by the camera vs. the position of the lamp can thus be acquired. The collected signal can then be used as an experimental method to determine the DOF of the ICCD camera's nine pixels. If the signal detected by the camera falls drastically when the lamp is moved away from the center of the nozzle exit, the effect of the low-energy wings can be neglected in the temporal LII signal collected from the center at y=88.

PAH-fluorescence or C_2-radicals/Carbonaceous Particles

Contribution from PAH-fluorescence can be ruled out as a probable cause as the first and second peak appeared so strongly in the 1064 nm temporal LII signals. Contribution from C_2-radicals or carbonaceous particles can also be assumed to be negligible as their effect should have been less when using the 1064 nm laser beam, and this was not seen.

Morphological Changes and Creation of New Particles

The second peak phenomenon can be caused by creation of new particles. A first thought was that as the laser impacts the soot aggregates within the flame, more primary particles become "freed". It would then be possible that the second peak is due to the fact that these newly freed particles in turn emit LII a short time later. However, as discussed in section 2.4.3, the soot aggregates don't break up as one might initially think will happen. Instead, the soot goes through morphological changes due to laser impact.

As mentioned in section 2.4.3, Michelsen et al. studied particle formation from pulsed laser irradiation from soot aggregates in 2007 (Michelsen et al., 2007). Studies found that as the soot particles vaporized, new particles were formed. Vaporization of the particle generates gasphase carbon species which further nucleate to form new particles.

Such changes in particle morphology and fine structure could have substantial effects on the temporal LII signal. It might therefore be possible that these new particles are the cause of the double peak phenomenon. If particles are created as a result of vaporization, the increased mass would create a stronger LII signal and thus result in a new peak in the temporal LII signal.

The data presented by Michelsen et al. also show that there is a fluence dependence on the size and number density of the new particles. With increasing fluence, the small particles increased in size and number concentration until a plateau was reached at the higher fluence values. The strong fluence dependence found for the double peak phenomenon could thus be closely linked to this observed dependence.

5.5 Advised Further Research

As the results presented in this thesis show, the double peak phenomenon is highly dependent on fluence. There seems to be a certain accumulated fluence threshold for two peaks to appear in the temporal LII signals. The figures of the time-integrated LII signal vs. fluence show a tendency not seen before. It is advised that this is studied more detailed, both for all the pulse durations in the 50 - 450 ns range and also for many more fluence values.

The advised detailed experimental measurements would also give more data to determine the double peak phenomenon's possible dependence on irradiance. LII measurements with irradiance in mind should be done by deciding the angle of the half-wave plate solely for giving average pulse energies of the same predetermined values. This would then have to be repeated for all the different pulse durations.

Furthermore, the ICCD camera used in this experimental setup takes an intensity image collected using a 5 ns opening time and quite a large field of view. To get time-resolved LII signals, using a photocathode is advised as this will return instantaneous signals in time. Time-resolved LII measurements collected using such a setup will result in more detailed graphs over the LII signal with varying fluence and varying pulse durations. One drawback is that finding the perfect focus position of such a camera is more difficult than with an ICCD camera that returns viewable 2D images.

Further research should be dedicated to the possibility of the double peak phenomenon being caused by morphological changes in the soot particles. A computational study with the introduction of the new particles created due to vaporization could yield interesting results. Such a study might result in the appearance of a first and second peak also in the numerically generated time-resolved LII signals. This can in turn be compared with experimental results and perhaps shed some more light as to the cause of the double peak.

6 Conclusion

Two peaks appear in the temporal LII signals when using a laser of long pulse duration and relatively high fluence. The pulse durations used in this project were in the range 50 ns - 450 ns. The laser pulse's energy was varied using a combination of a half-wave plate and a beamsplitter.

The cause of the two peaks appearing in the temporal LII signal is still unknown, but the results show some interesting aspects of the phenomenon. Evidently, there is a strong fluence dependence. For the two peaks to appear, a certain fluence threshold must be reached.

Studies of the time-integrated LII signal vs. laser pulse fluence revealed a signal which increased sharply until around 0.4-0.5 J/cm^2 where it appeared to saturate. However, past this threshold, the signal began to increase again. Previously, such fluence profiles have been known to saturate completely around 0.4-0.5 J/cm^2 for 1064 nm laser light. It is past this threshold that the two peaks become visible in the temporal LII signals.

The phenomenon's irradiance dependence was also analyzed, but more data is required to give a decisive conclusion. It might be that the two peaks are present in all temporal LII signals, only that when short pulses are used, the two peaks are not discernible and are instead seen as one.

PAH-fluorescence and contribution from C_2-radicals have been ruled out as possible causes of the phenomenon. The two peaks might be caused by morphological changes in the soot, or by creation of new particles due to vaporization. They might also be caused by unknown processes the soot undergoes when impacted by the laser beam. A more extensive experimental investigation is advised, preferably in combination with computational modeling.

Bibliography

Bengtsson, P.-E., Aldn, M., 1995. Soot-visualization strategies using laser techniques. Applied Physics B 60, 51–59.

ContinuumCorporation, 2005-2008. DLR Custom Laser System Graphical User Interface User Manual.

ContinuumCorporation, 2008. Agilite 569-10 QA-Report.

Dalzell, W. H., Sarofim, A. F., 1969. Optical constants of soot and their application to heat flux calculations. Journal of Heat Transfer 91, 100–104.

Dasch, C. J., 1984a. Continuous-wave probe laser investigation of laser vaporization of small soot particles in a flame. Applied Optics 23, 22092215.

Dasch, C. J., 1984b. Spatially resolved soot-absorption measurements in flames using laser vaporization of particles. Opt. Lett. 9, 214–216.

Ditaranto, M., Meraner, C., Haugen, N. E. L., Saanum, I., 2013. Influence of long pulse duration on time-resolved laser-induced incandescence. Applied Physics B (in press).

Dobbins, R. A., Subramaniasivam, H., 1994. Soot Precursor Particles in Flames. Springer Series in Chemical Physics 59, 291299.

Eckbreth, A. C., 1977. Effects of laser-modulated particulate incandescence on Raman scattering diagnostics. Journal of Applied Physics 48 (11), 4473–4479.

Eckbreth, A. C., 1996. Laser Diagnostics for Combustion Temperature and Species, 2nd Edition. Gordon and Breach Science Publishers, Combustion Science and Technology Book Series Volume 3.

Einstein, A., 1916. Strahlungs-Emission und absorption nach der Quantentheorie. Verhandlungen der Deutschen Physikalischen Gesellschaft 18, 318–323.

Geusic, J. E., Marcos, H. M., van Uitert, L. G., 1964. Laser Oscillations in Nd-doped Yttrium Aluminum, Yttrium Gallium and Gadolinium Garnets. Applied Physics Letters 4 (10), 182–184.

Hofmann, M., Kock, B., Schulz, C., 2007. A web-based interface for modeling laser-induced incandescence (LIISim). Proceedings of the Third European Combustion Meeting, website: http://www.liisim.com.

Melton, L. A., 1984. Soot diagnostics based on laser heating. Applied Optics 23 (13), 2201–2208.

Michelsen, H. A., 2003. Understanding and predicting the temporal response of laser-induced incandescence from carbonaceous particles. Journal of Chemical Physics 118 (15), 7012–7045.

Michelsen, H. A., Tivanski, A. V., Gilles, M. K., van Poppel, L. H., Dansson, M. A., Buseck, P. R., 2007. Particle formation from pulsed laser irradiation of soot aggregates studied with a scanning mobility particle sizer, a transmission electron microscope, and a scanning transmission x-ray microscope. Applied Optics 46 (6), 959–977.

Michelsen, H. A., Witze, P. O., Kayes, D., Hochgreb, S., 2003. Time-resolved laser-induced incandescence of soot: the influence of experimental factors and microphysical mechanisms. Applied Optics 42, 5577–5590.

Papen, G., 2013. Lecture notes in course ECE185 - Lasers and Modulators, UCSD Spring 2013. Http://papenlab1.ucsd.edu/ itunes101/ECE185/index.php?id=slides.

Qamar, N. H., Nathan, G. J., Alwahabi, Z. T., King, K. D., 2005. Effect of Turbulent Mixing on Soot Sheet Dimensions. 5th Asia-Pacific Conference on Combustion.

Schulz, C., Kock, B. F., Hofmann, M., Michelsen, H., Will, S., Bougie, B., Suntz, R., Smallwood, G., 2006. Laser-induced incandescence: recent trends and current questions. Applied Physics B 83, 333–354.

Sevault, A., 2012. Investigation of the Structure of Oxy-Fuel Flames Using Raman Laser Diagnostics. Ph.D. thesis, NTNU, Norwegian University of Science and Technology.

Verdeyen, J. T., 1995. Laser Electronics, 3rd Edition. Prentice Hall.

Wal, R. L. V., Jensen, K. A., 1998. Laser-induced incandescence: excitation intensity. Applied Optics 37, 1607–1616.

Wal, R. L. V., Jensen, K. A., Choi, M. Y., 1997. Simultaneous laser-induced emission of soot and polycyclic aromatic hydrocarbons within a gas-jet diffusion flame. Comb. Flame 109, 399–414.

Will, S., Schraml, S., Bader, K., Leipertz, A., 1998. Performance characteristics of soot primary particle size measurements by time-resolved laser-induced incandescence. Applied Optics 37, 5647–5658.

Witze, P. O., Hochgreb, S., Kayes, D., Michelsen, H. A., Shaddix, C. R., 2001. Time-resolved laser-induced incandescence and laser elastic scattering measurements in a propane diffusion flame. Applied Optics 40, 24432452.

Yoder, G. D., Diwakar, P. K., Hahn, D. W., 2005. Assessment of soot particle vaporization effects during laser-induced incandescence with time-resolved light scattering. Applied Optics 44 (20), 4211–4219.

Zizak, G., 2000. Laser Induced Incandescence (LII) of soot. ICS Training Course on Laser Diagnostics of Combustion Processes, NILES, University of Cairo, Egypt.

Appendix

6.1 Laser Beam Profiles

6.1.1 Previously Obtained 532 nm Laser Beam Profile

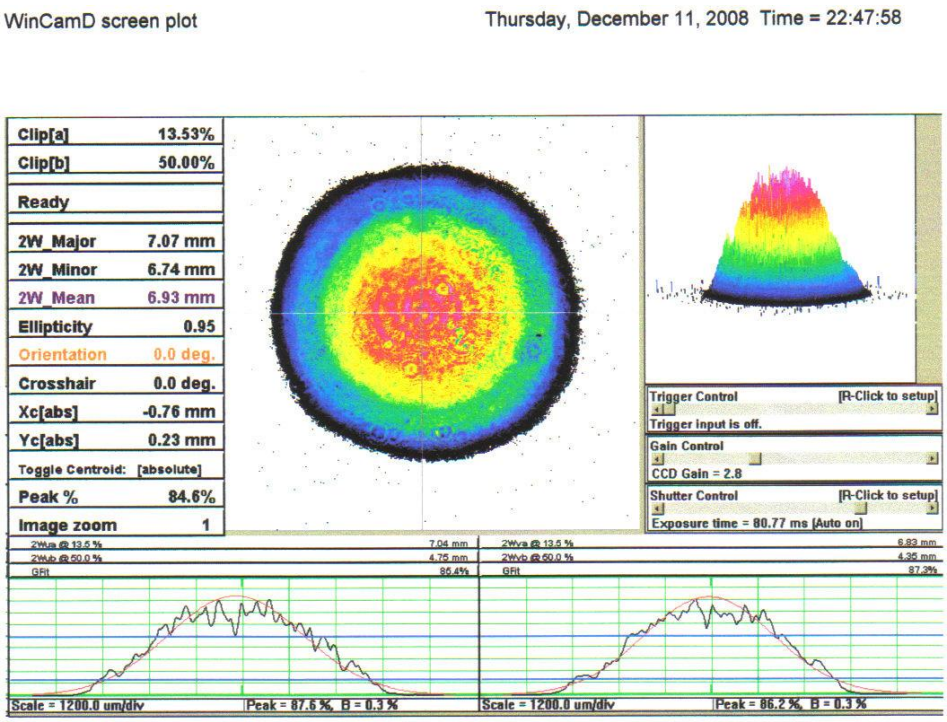

Figure 6.1: The radial profile of the output beam from the Nd:YAG laser taken several years earlier. The picture is taken after two wedges at 0.75 m from the laser output port. The original laser beam has diameter of about 7 mm and a Gaussian radial beam profile. Figure from the manufacturers of the laser (ContinuumCorporation, 2008) at time of installation.

6.1.2 1064 nm Laser Beam Profile - With 4 mm Aperture at Flame Distance

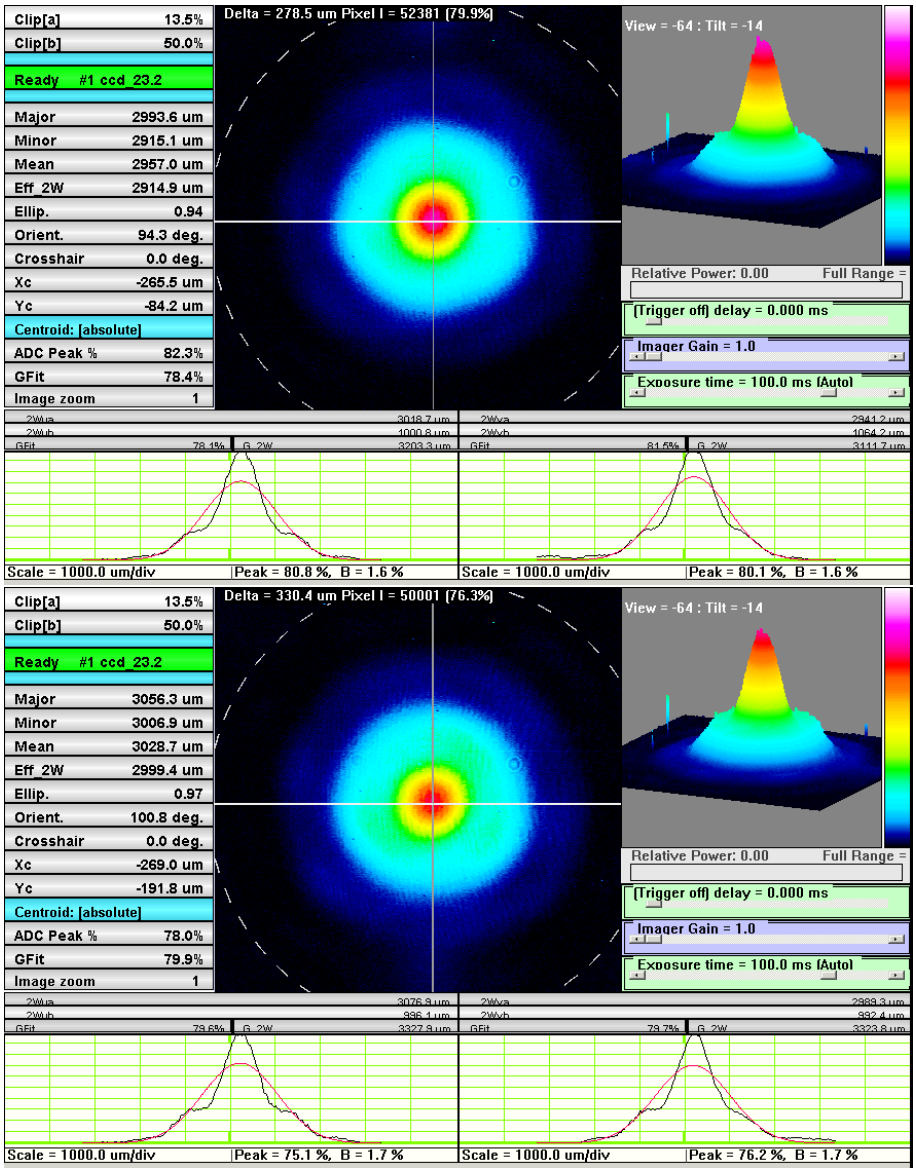

Figure 6.2: Spatial beam profile of the 1064 nm laser beam with 4 mm aperture in place. The pulse duration was 100 ns and the energy about 160 mJ and 260 mJ. Because of the intensity wings, the fitted Gaussian curves in red have a much lower peak value. The resulting average measured $1/e^2$-widths were 2.98 and 3.03 mm at the flame distance.

6.2 Energy Loss of 532 nm Energy Detector Container

The 100 ns laser pulse was used for the experiments. Four measurements, each an average of 500 pulses, were collected before the nozzle and after. Throughout the measurements, the internal temperatures of the laser remained the same, ensuring consistent results. As Figure 6.3 shows, there is some loss due to encapsulating the energy detector after the nozzle. This loss is about 10 %. In the experiments using the 532 nm laser beam, the estimated energy reaching the flame can be assumed to be $1.1 \cdot E_{after}$.

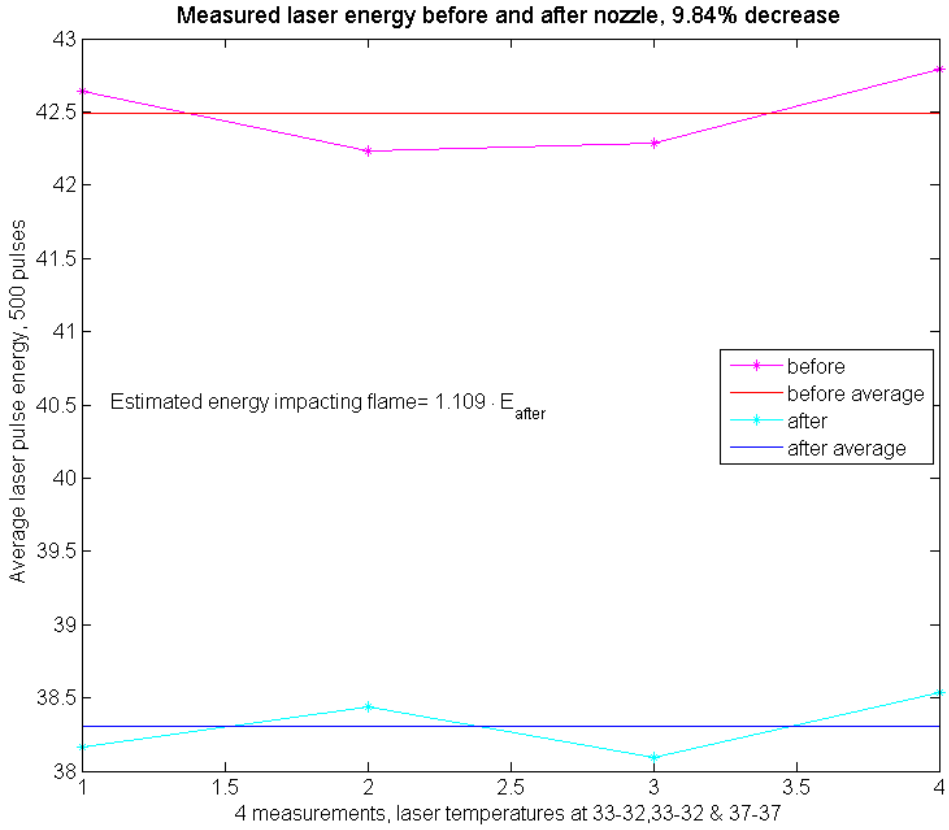

Figure 6.3: Laser pulse energy before and after nozzle. An approximate 10 % reduction in energy was found due to the container the energy detector is placed in when positioned after the nozzle exit.

6.3 Checking if Notch Filter is Dependent on Angle of Incidence

There had previously been registered some dependence on the angle of incidence of the notch filter. Measurements were therefore done with the notch at slightly different angles. Five temporal LII measurements per angle were collected for 0° to 7°. Figure 6.4 shows the resulting average temporal LII signals for the different angles.

It is the prompt LII signal that is of importance, and here very little difference was seen. A slightly higher peak signal was found for the 7° notch angle, but overall the notch filter can be assumed to be independent of angle. Normal incidence was thus chosen for all further LII measurements as measurements prior to the notch tests had had this setup.

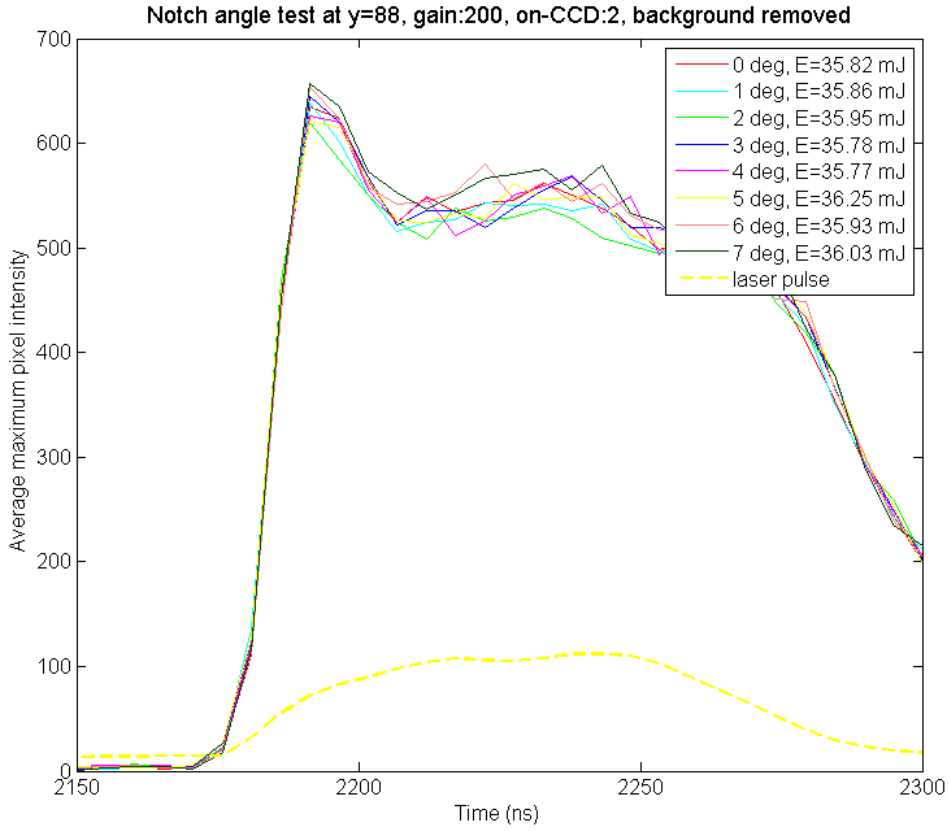

Figure 6.4: Notch angles, average of five measurements per angle

6.4 Temporal Laser Pulse Shapes

Figures 6.5 - 6.12 show the temporal shape of the different pulse durations. The average pixel intensity was found for each frame of the 100 frames taken per measurement, within a chosen ROI.

50 ns Pulse Duration

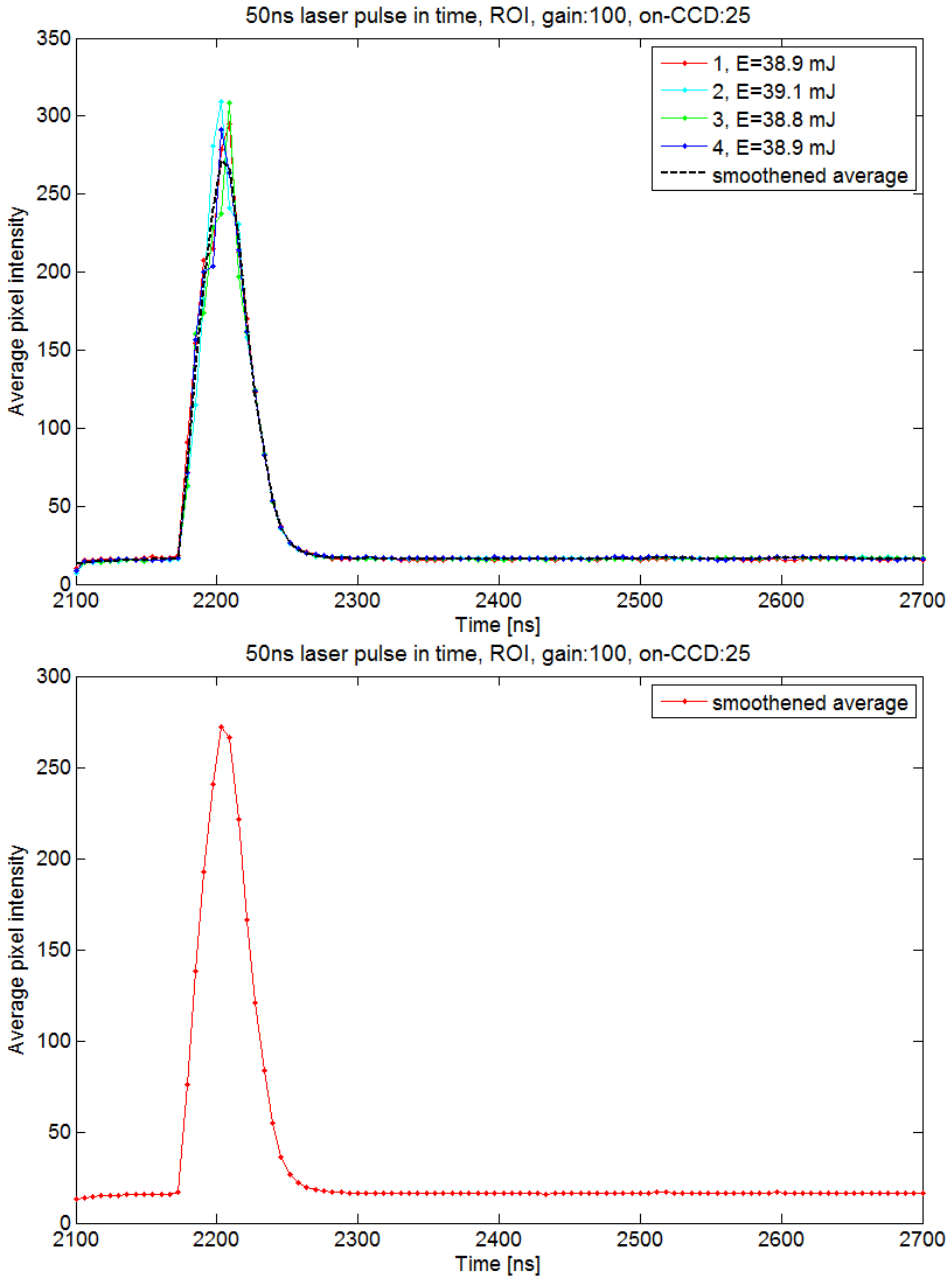

Figure 6.5: Rayleigh scattering signal from the 50 ns laser beam. The dotted black curve in the top graph shows the smoothened average signal, depicted by itself in the bottom graph.

100 ns Pulse Duration

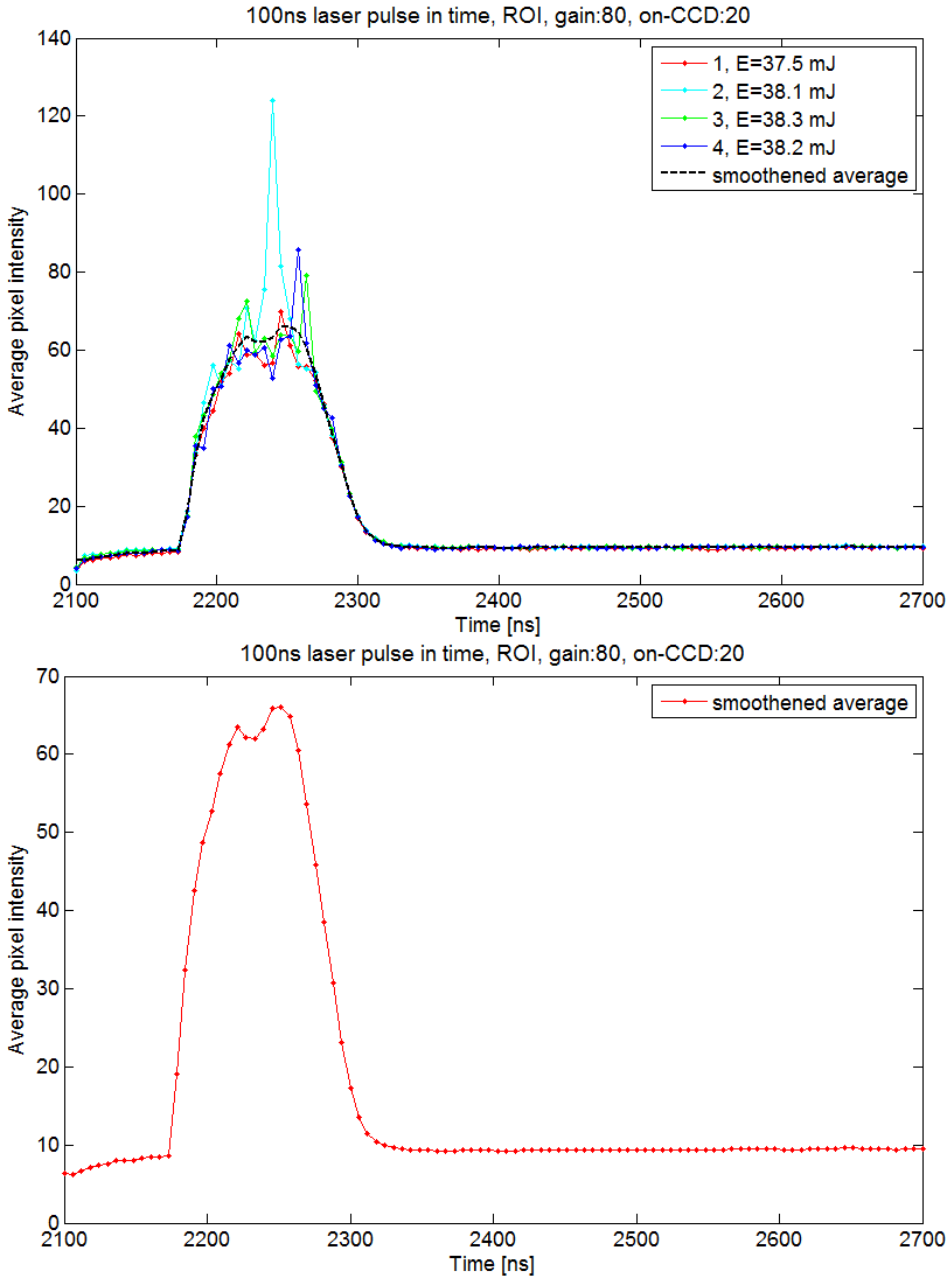

Figure 6.6: Rayleigh scattering signal from the 100 ns laser beam. The dotted black curve in the top graph shows the smoothened average signal, depicted by itself in the bottom graph.

150 ns Pulse Duration

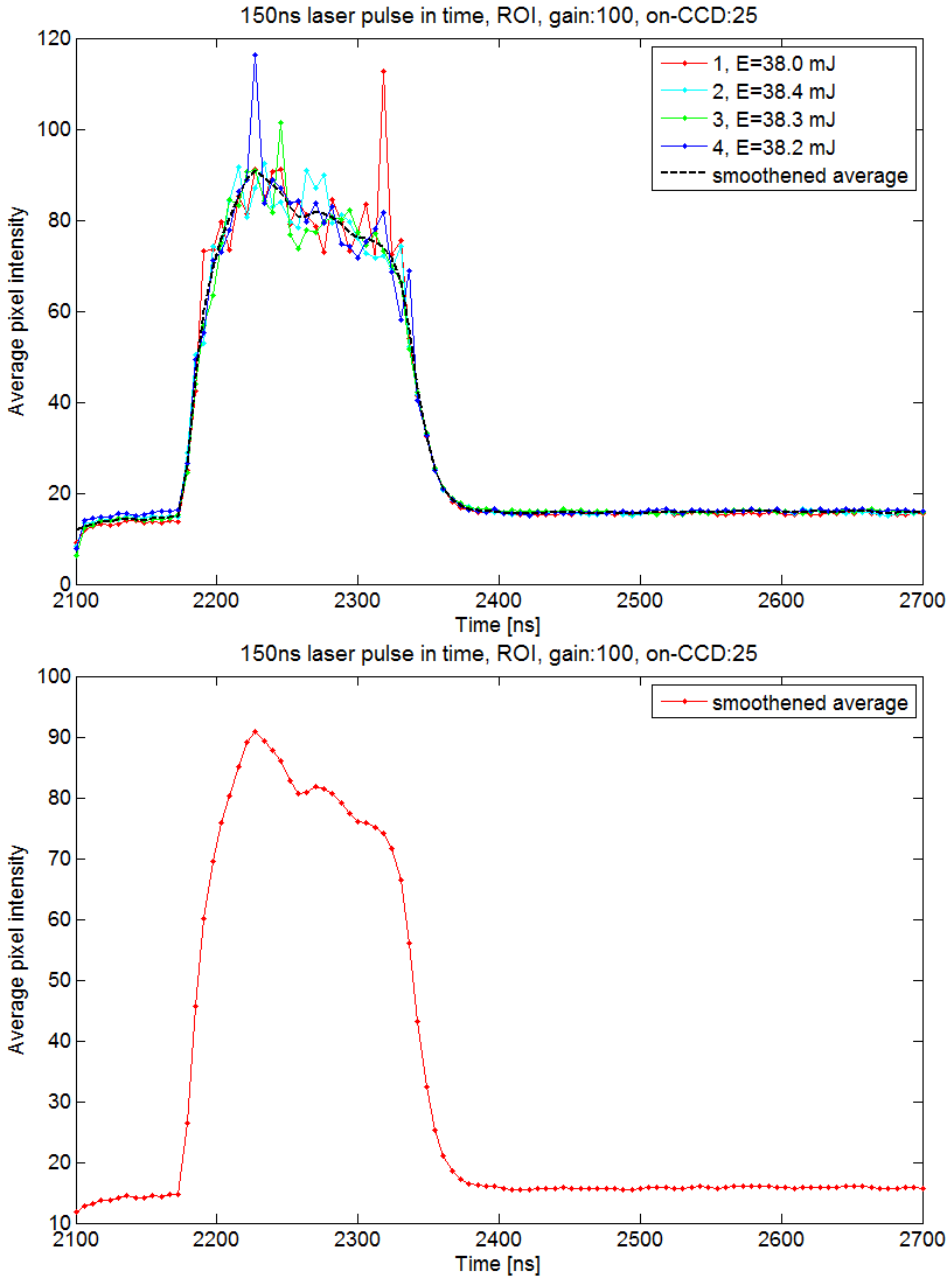

Figure 6.7: Rayleigh scattering signal from the 150 ns laser beam. The dotted black curve in the top graph shows the smoothened average signal, depicted by itself in the bottom graph.

200 ns Pulse Duration

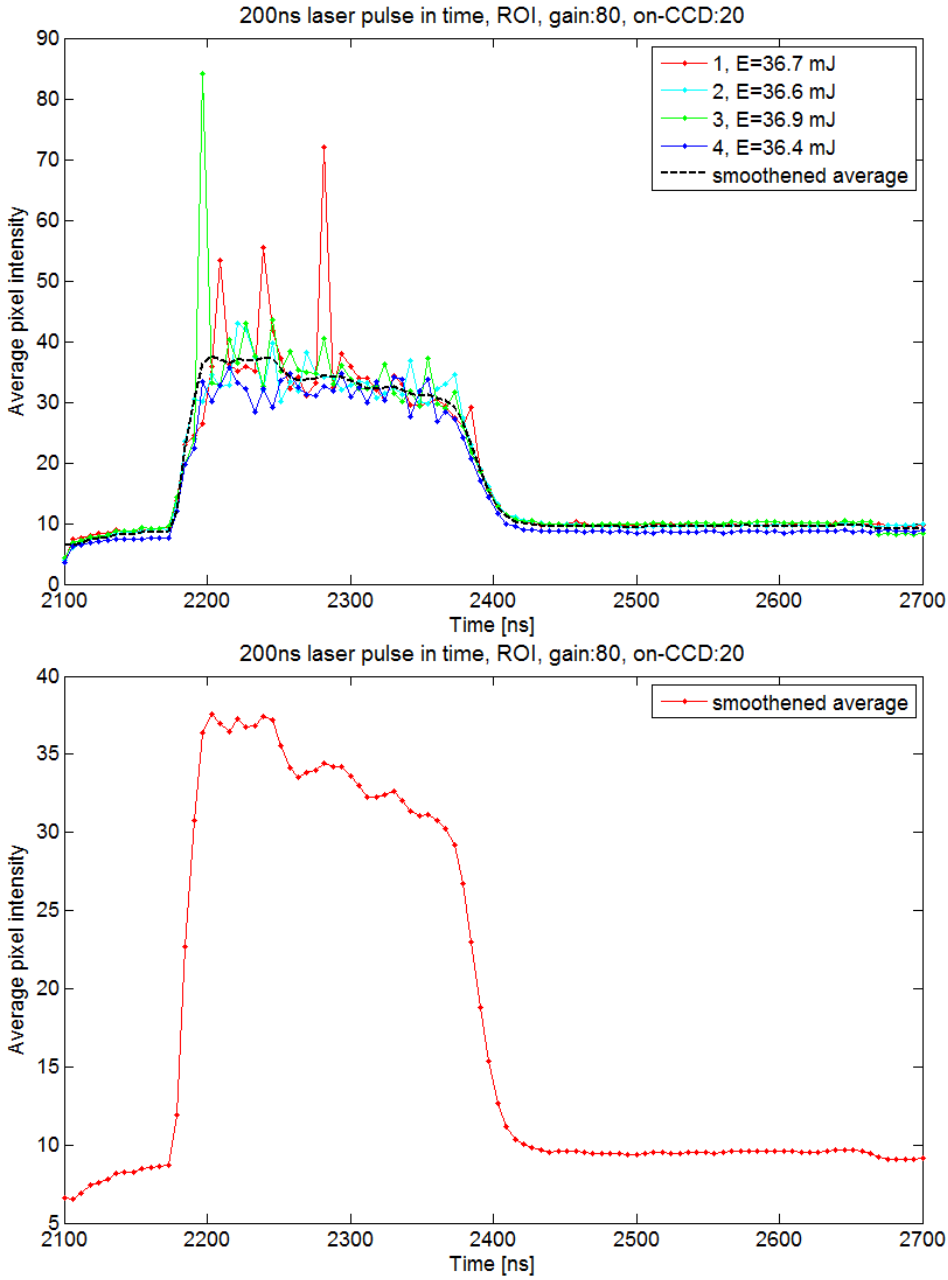

Figure 6.8: Rayleigh scattering signal from the 200 ns laser beam. The dotted black curve in the top graph shows the smoothened average signal, depicted by itself in the bottom graph.

250 ns Pulse Duration

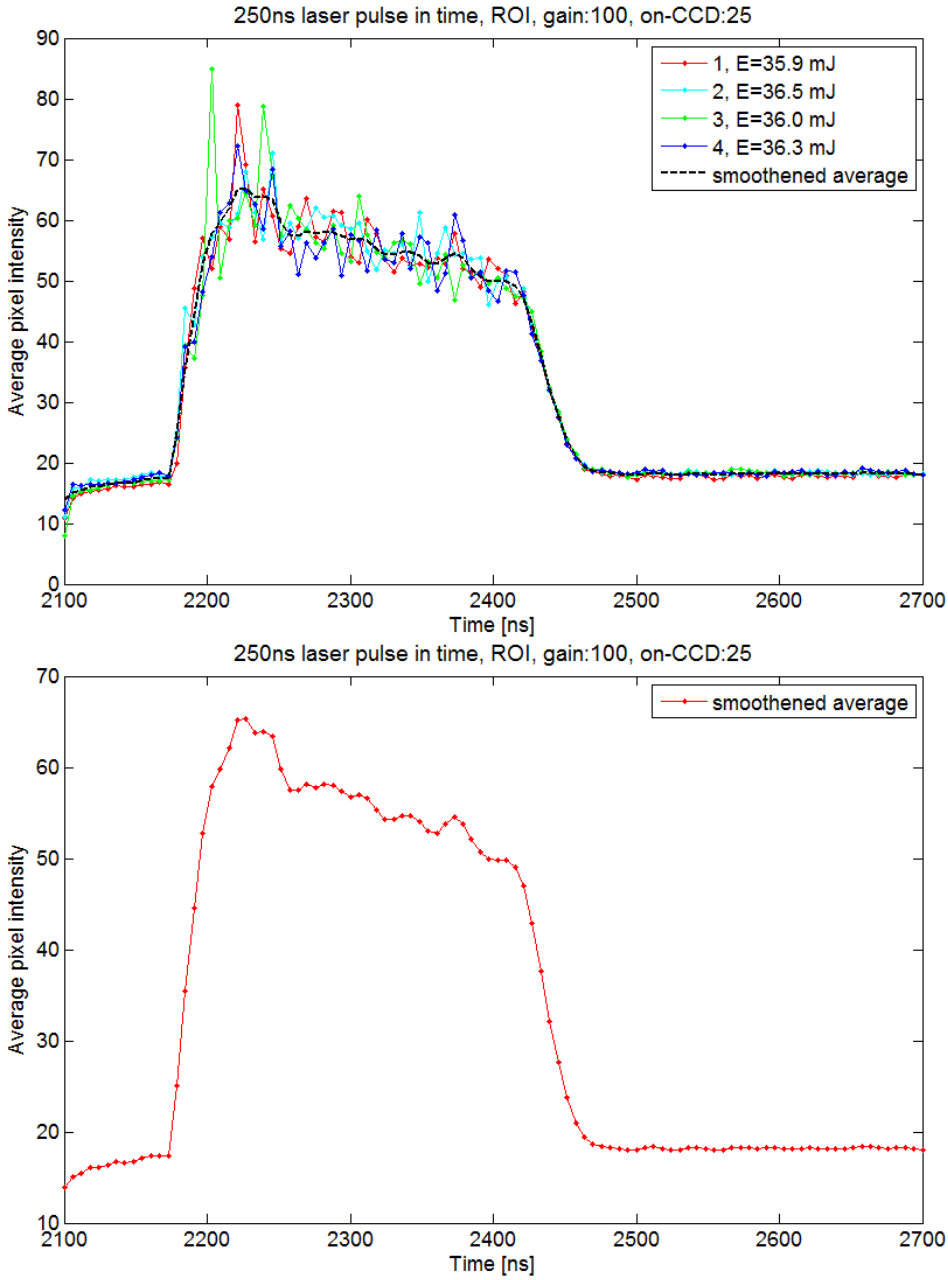

Figure 6.9: Rayleigh scattering signal from the 250 ns laser beam. The dotted black curve in the top graph shows the smoothened average signal, depicted by itself in the bottom graph.

300 ns Pulse Duration

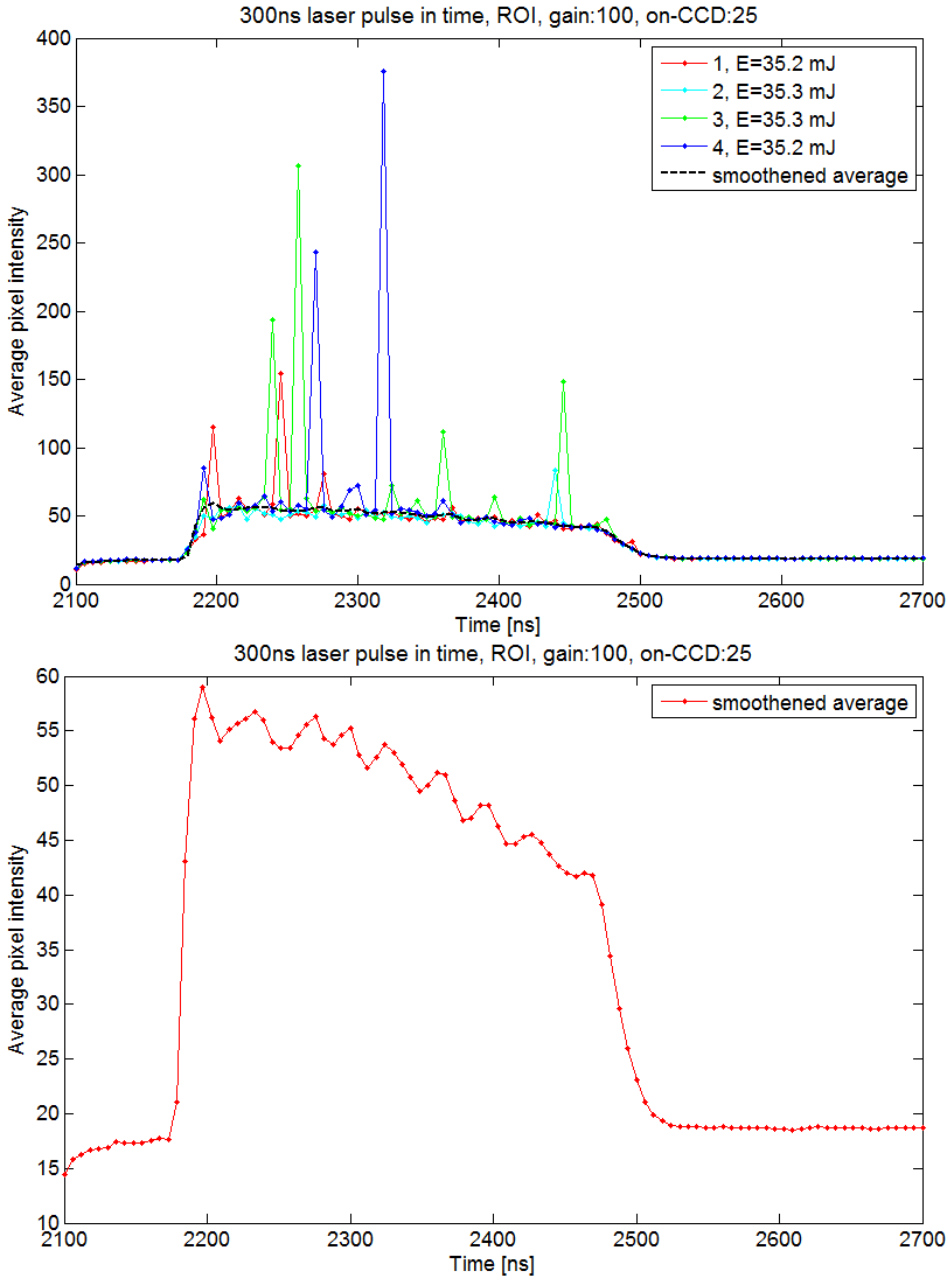

Figure 6.10: Rayleigh scattering signal from the 300 ns laser beam. The dotted black curve in the top graph shows the smoothened average signal, depicted by itself in the bottom graph.

400 ns Pulse Duration

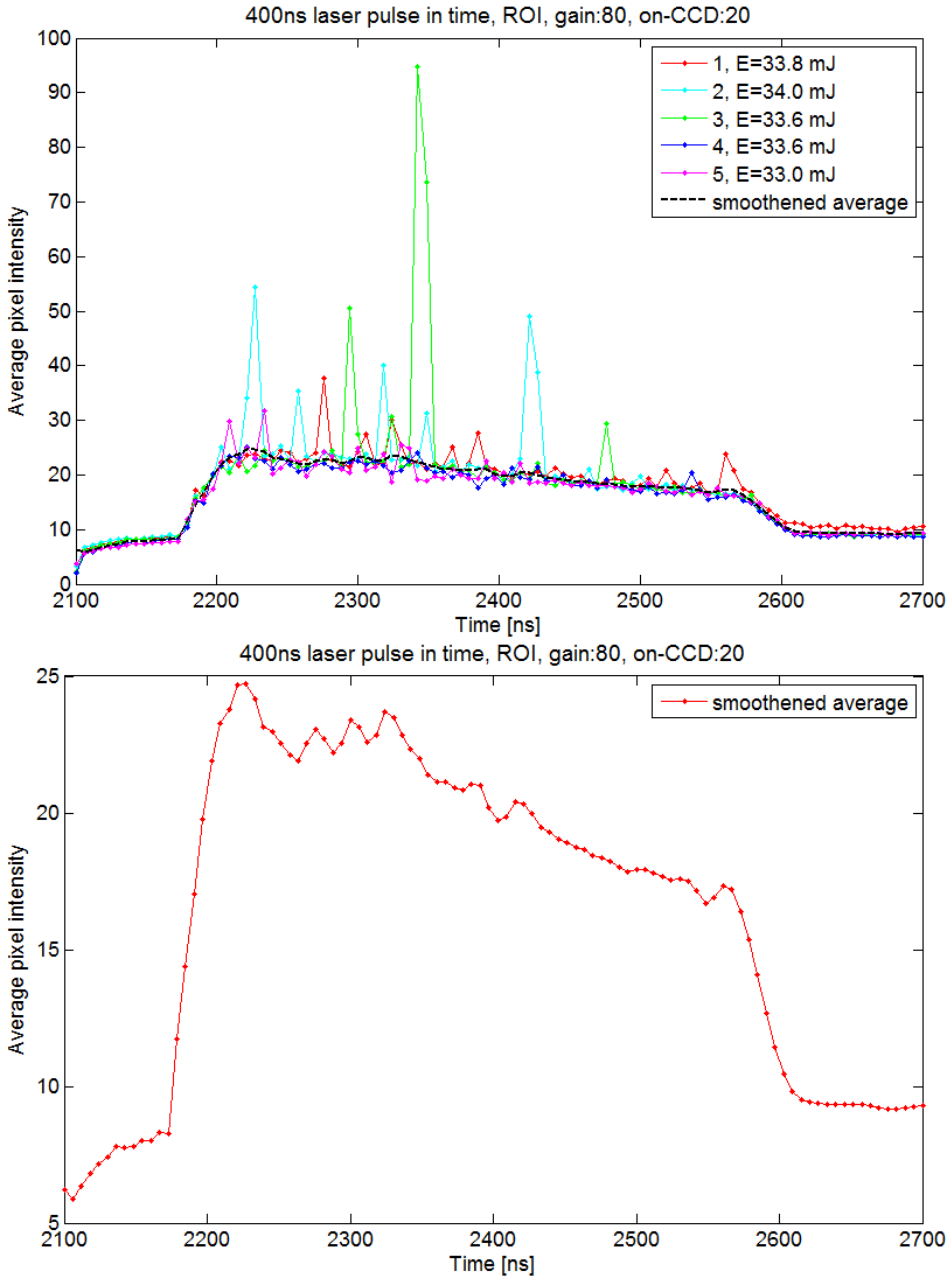

Figure 6.11: Rayleigh scattering signal from the 400 ns laser beam. The dotted black curve in the top graph shows the smoothened average signal, depicted by itself in the bottom graph.

450 ns Pulse Duration

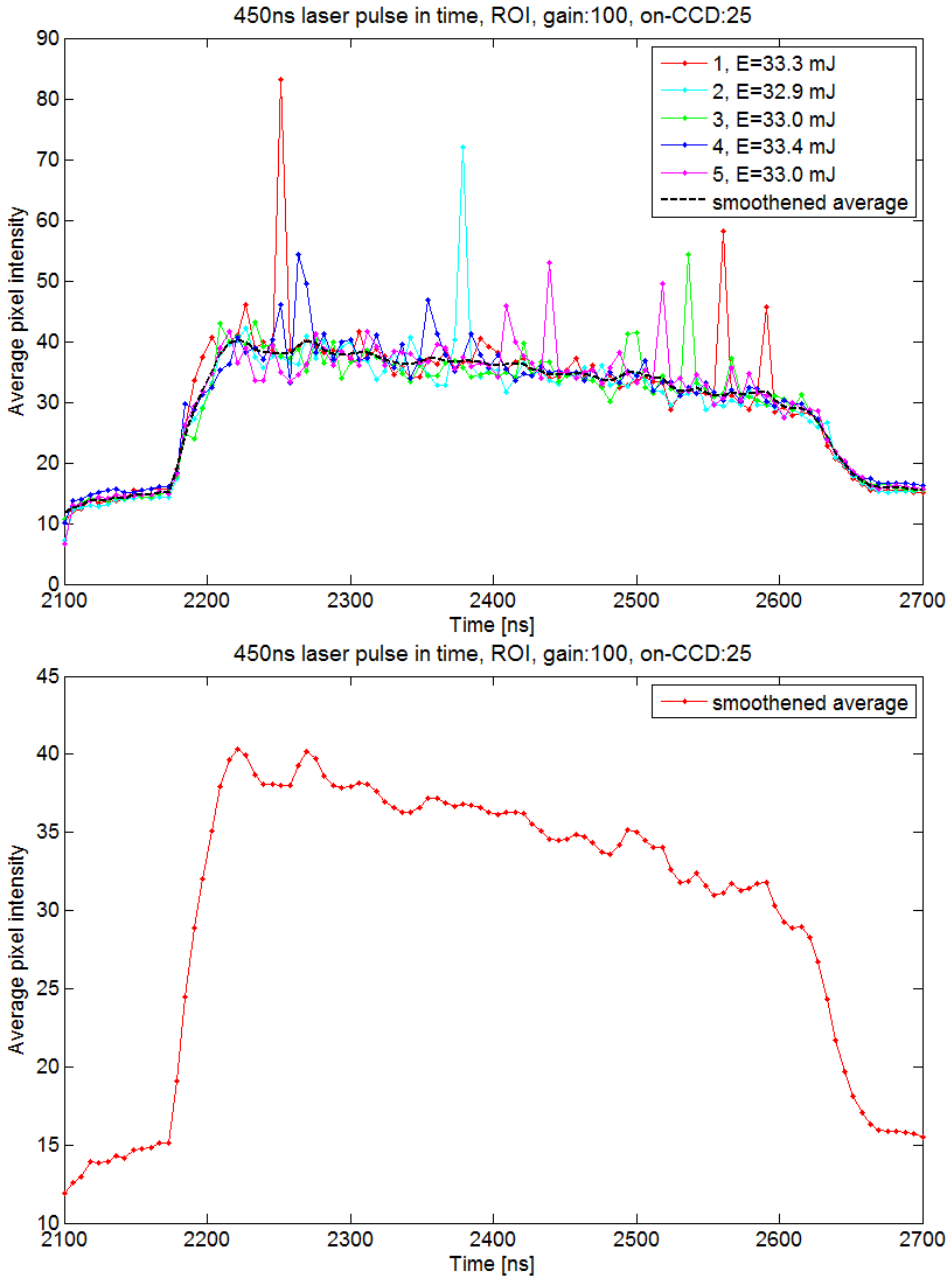

Figure 6.12: Rayleigh scattering signal from the 450 ns laser beam. The dotted black curve in the top graph shows the smoothened average signal, depicted by itself in the bottom graph.